Master's thesis

NTNU
Norwegian University of Science and Technology
Faculty of Engineering
Department of Structural Engineering

Sigurd Aune & Jostein Lima

Modelling and Simulation of Yielding, Work-Hardening and Fracture of Advanced High-Strength Steels

Master's thesis in Civil and Environmental Engineering
Supervisor: Odd Sture Hopperstad
June 2020

NTNU
Norwegian University of
Science and Technology

Sigurd Aune & Jostein Lima

Modelling and Simulation of Yielding, Work-Hardening and Fracture of Advanced High-Strength Steels

Master's thesis in Civil and Environmental Engineering
Supervisor: Odd Sture Hopperstad
June 2020

Norwegian University of Science and Technology
Faculty of Engineering
Department of Structural Engineering

NTNU
Norwegian University of
Science and Technology

Department of Structural Engineering
FACULTY OF ENGINEERING SCIENCE
NTNU – Norwegian University of Science and Technology

MASTER'S THESIS 2020

for

Sigurd Aune and Jostein Lima

Modelling and simulation of yielding, work-hardening and fracture of advanced high-strength steels

Advanced high-strength steels (AHSS) are complex materials with selected chemical compositions and multiphase microstructures that result from precisely controlled heating and cooling processes. Various physical mechanisms are used to achieve a variety of strength, ductility, toughness and fatigue properties. In the automotive industry, AHSS is used in load-bearing components, bumper systems, battery protection, door joists, etc.

Dual-phase (DP) steels are advanced high-strength steels widely used in automotive applications. The microstructure of dual-phase steels consists of martensitic islands embedded in a ferrite matrix. The ferrite is soft giving a high degree of ductility, while the martensite is hard providing high strength. The interaction between the soft ferrite and the hard martensite leads to strong work hardening, which is an important factor in distributing plastic deformation in a deformed structure and thus improving the deformability. By use micromechanical finite element (FE) simulations it is today possible to study the deformation within the two phases and thus to improve our understanding of how the strain is distributed and the energy is absorbed under large deformations in this type of microstructure. It is also possible to study how the plastic behaviour (i.e., yielding and work-hardening) is affected by the microstructure, and to investigate possible mechanisms of ductile fracture.

In this project, material models for plasticity and fracture are established for DP steels with different martensite content based on existing laboratory tests and micromechanical FE simulations. Laboratory tests will be performed to investigate the Bauschinger effect as a function of martensite content using a specially-designed anti-buckling device. The main objective of the master's project is to use micromechanical FE simulations to study the influence of martensite volume fraction and distribution on yielding, work-hardening and ductility.

The key tasks of the master's project are as follows:

1. To conduct a literature study on the microstructure, mechanical behaviour, and microstructure-based modelling and simulation of DP steels.
2. To carry out an experimental study on the influence of martensite volume fraction on the Bauschinger effect in dual-phase steel.
3. To establish a micromechanical FE modelling framework for plasticity and fracture of DP steels.
4. To perform a numerical study on yielding, work-hardening and ductile fracture of DP steels and compare the results to existing and new experimental data.
5. To propose and calibrate a material model for DP steels applicable to large-scale FE simulations of structural components based on the experimental data and the micromechanical analyses.

Supervisors: Odd Sture Hopperstad, Maria Jesus Perez Martin, Borja Erice

The thesis must be written according to current requirements and submitted to the Department of Structural Engineering, NTNU, no later than June 10th, 2020.

NTNU, January 15th, 2020.

Odd Sture Hopperstad
Professor

Department of Structural Engineering
Faculty of Engineering
NTNU – Norwegian University of Science and Technology

ACCESSIBILITY
OPEN

MASTER THESIS 2020

SUBJECT AREA: Computational Mechanics	DATE: June 10, 2020	NO. OF PAGES: 6+98+27

TITLE:

Modelling and simulation of yielding, work-hardening and fracture of advanced high-strength steels

Modellering og simulering av flyt, fastning og brudd i avansert høyfast stål

BY: Sigurd Aune og Jostein Lima

SUMMARY:
In this thesis, cyclic load experiments are conducted by use of an anti-buckling device to investigate the influence of martensite volume fraction on the Bauschinger effect in dual-phase (DP) steels. Four different DP steels are tested: Docol 500DP, 600DP, 800DP and 1000DP. Then, microstructure-based modelling and simulations are conducted to study the influence of martensite volume fraction and distribution on yielding, work-hardening and ductility of the DP steels. Finally, material models for the DP steels applicable to large-scale FE simulations based on the experimental data and the micromechanical analyses are proposed.

The cyclic load experiments were successfully conducted by use of an anti-buckling device. The Bauschinger effect was found to increase with the DP steel quality and the martensite volume fraction in the experiments.

The microstructure-based modelling was done by establishing a micromechanical FE modelling framework for plasticity and fracture. Four different representative volume elements (RVEs) with idealized geometry were considered. An RVE with a single cubical martensite island in the centre was established as the micromechanical FE modelling framework since it in general was superior to the other three when compared to stress-strain curves from experimental data.

The RVEs were used to perform a numerical study on yielding, work-hardening and ductile fracture. It was found that the yielding resembled the Hershey yield locus with an exponent of $m=6$. Further, it was reported that the ferrite-martensite strength difference did not capture all of the Bauschinger effect experienced in experiments. The numerical study of ductile fracture was based on the implementation of the Gurson model in the ferrite material model. The influence of the Gurson parameters and the obtained fracture mechanisms were discussed. It was concluded that the Gurson model with only the initial void volume fraction feature and the porous failure criterion was not sufficient when the martensite volume fraction increased.

Lastly, material models were proposed for DP steels applicable to large-scale FE simulations based on experiments and idealized RVEs. This was done by conducting a micro-macro transition approach. The final material models were Gurson models, where the work-hardening was described by Voce hardening laws and damage was included through nucleation and growth of voids.

RESPONSIBLE TEACHER: Odd Sture Hopperstad
SUPERVISOR(S): Maria Jesus Perez Martin, Borja Erice og Lars Edvard Blystad Dæhli
CARRIED OUT AT: SIMLab, the Department of Structural Engineering, NTNU

Institutt for konstruksjonsteknikk
Fakultet for ingeniørvitenskap
NTNU – Norges teknisk-naturvitenskapelige universitet

TILGJENGELIGHET
ÅPEN

MASTEROPPGAVE 2020

FAGOMRÅDE: Beregningsmekanikk	DATO: 10.06.2020	ANTALL SIDER: 6+98+27

TITTEL:

Modellering og simulering av flyt, fastning og brudd i avansert høyfast stål

Modelling and simulation of yielding, work-hardening and fracture of advanced high-strength steels

UTFØRT AV: Sigurd Aune og Jostein Lima

SAMMENDRAG:
I denne avhandlingen ble eksperiment med syklisk last utført ved bruk av et anti-knekkingsutstyr for å undersøke hvilken påvirkning volumfraksjonen av martensitt har på Bauschingereffekten i tofasestål. Fire forskjellige tofasestål ble undersøkt: Docol 500DP, 600DP, 800DP og 1000DP. Deretter ble modellering og simulering basert på mikrostruktur utført for å undersøke hvilken påvirkning volumfraksjonen og fordelingen av martensitt har på flyt, fastning og duktilitet i tofasestålene. Til slutt ble det foreslått materialmodeller som kan brukes i storskalasimuleringer basert på eksperimentelle data og mikromekaniske analyser.

Syklisk last eksperimentene hvor anti-knekkingsutstyret ble brukt var vellykket, og det ble funnet at Bauschingereffekten økte med stålkvaliteten og volumfraksjonen av martensitt.

Modelleringen basert på mikrostruktur ble gjennomført ved å danne et rammeverk for modellering av plastisitet og brudd. Fire forskjellige representative volumelementer (RVEer) med idealisert geometri ble vurdert. RVEen med én kubisk øy av martensitt la grunnlaget for rammeverket, ettersom dette var RVEen som etterlignet spennig-tøyningskurvene fra eksperiment best.

RVEene ble brukt for å undersøke flyt, fastning og duktilt brudd. Det ble funnet at flytningen liknet en Hershey flyteflate med eksponenten $m=6$. Videre ble det funnet at styrkeforskjellen mellom ferritt og martensitt ikke var nok til å gjenskape hele Bauschingereffekten observert i eksperimentene. Bruddstudiet ble utført ved å implementere Gursonmodellen inn i materialmodellen til ferritten. Effektene av Gurson-parameterne og bruddmekanismene ble deretter undersøkt. Det ble konkludert at Gursonmodellen med kun initiale porer og et porøst bruddkriterium ikke var godt nok når volumfraksjonen av martensitt økte.

Til slutt ble det, basert på eksperimenter og idealiserte RVEer, foreslått materialmodeller som kan brukes i storskalasimuleringer. Dette ble gjort med en mikro-til-makrometode. De resulterende materialmodellene var Gursonmodeller hvor Voce fastningslov og skade gjennom nukleering og vekst av porer ble inkludert.

FAGLÆRER: Odd Sture Hopperstad
VEILEDER(E): Maria Jesus Perez Martin, Borja Erice og Lars Edvard Blystad Dæhli
UTFØRT VED: SIMLab, Institutt for konstruksjonsteknikk, NTNU

Preface

This masters thesis was conducted at the Structural Impact Laboratory (SIMLab) at the Norwegian University of Science and Technology (NTNU) in the spring of 2020. The final requirement for the degree of Master of Science in Civil Engineering at NTNU is the master thesis and it has a weight of 30 credits. The duration was 20 weeks from January to June 2020. The main supervisor of this thesis was Odd Sture Hopperstad at the Department of Structural Engineering at NTNU. Maria Jesus Perez Martin, Borja Erice, and Lars Edvard Blystad Dæhli from the same department contributed as co-supervisors.

Acknowledgements

First, we want to thank Senior Engineer Trond Auestad at the Department of Structural Engineering for helping us with conducting the laboratory tests. We wish to thank Postdoctoral Researcher Maria Jesus Perez Martin and Researcher Borja Erice at the Department of Structural Engineering for all help received during this study. Your attendance when conducting the laboratory tests, which ensured smooth execution of the tests, was much appreciated. You quickly answered our questions by e-mail, shared post-processing scripts, and provided us with data from the former conducted experiments. We are grateful for your attendance at our weekly guiding meetings, where you asked questions and shared your experiences.

Further, a special thanks is addressed to Postdoctoral Researcher Lars Edvard Blystad Dæhli at the Department of Structural Engineering. Without hesitating, you always helped us when we came knocking on your office door. You were encouraging and motivated us to reflect on our findings, which increased the quality of the final work.

Last, but not least, a special thanks goes to our main supervisor Professor Odd Sture Hopperstad at the Department of Structural Engineering. First of all, your knowledge in the field of micromechanics is marvellous. More important to us were the curiosity and eagerness you showed during our guiding sessions. It motivated us to do the work thoroughly and to be well prepared for our meetings. Your guidance and support throughout this thesis are deeply appreciated.

Abstract

In this thesis, cyclic load experiments are conducted by use of an anti-buckling device to investigate the influence of martensite volume fraction on the Bauschinger effect in dual-phase (DP) steels. Four different DP steels are tested: Docol 500DP, 600DP, 800DP and 1000DP. Then, microstructure-based modelling and simulations are conducted to study the influence of martensite volume fraction and distribution on yielding, work-hardening and ductility of the DP steels. Finally, material models for the DP steels applicable to large-scale FE simulations based on the experimental data and the micromechanical analyses are proposed.

The cyclic load experiments were successfully conducted by use of an anti-buckling device. The Bauschinger effect was found to increase with the DP steel quality and the martensite volume fraction in the experiments.

The microstructure-based modelling was done by establishing a micromechanical FE modelling framework for plasticity and fracture. Four different representative volume elements (RVEs) with idealized geometry were considered. An RVE with a single cubical martensite island in the centre was established as the micromechanical FE modelling framework since it in general was superior to the other three when compared to stress-strain curves from experimental data.

The RVEs were used to perform a numerical study on yielding, work-hardening and ductile fracture. It was found that the yielding resembled the Hershey yield locus with an exponent of $m = 6$. Further, it was reported that the ferrite-martensite strength difference did not capture all of the Bauschinger effect experienced in experiments. The numerical study of ductile fracture was based on the implementation of the Gurson model in the ferrite material model. The influence of the Gurson parameters and the obtained fracture mechanisms were discussed. It was concluded that the Gurson model with only the initial void volume fraction feature and the porous failure criterion was not sufficient when the martensite volume fraction increased.

Lastly, material models were proposed for DP steels applicable to large-scale FE simulations based on experiments and idealized RVEs. This was done by conducting a micro-macro transition approach. The final material models were Gur-

son models, where the work-hardening was described by Voce hardening laws and damage was included through nucleation and growth of voids.

Contents

1 Introduction

In the automotive industry it is crucial to improve performance of the cars and reducing production costs in order to be competitive. This could be done by improving the engine, enhancing the crash safety, reducing the fuel consumption, increasing the efficiency of the production etc. For instance, by decreasing the vehicle weight the fuel consumption could be reduced. This could be done by using thinner sheets. However, the requirements regarding the crash safety are becoming more stringent, and high-strength materials with good formability are a prerequisite for success. It is challenging to develop such materials, since the strength of the material often is inversely proportional to its ductility (Davies 1978). Thus, many researchers have the last decades given their effort to develop such materials.

The advanced high-strength steels (AHSS) are steels with superior mechanical properties. They are complex materials with selected chemical compositions and multiphase microstructures obtained by using controlled thermomechanical treatment. Various physical mechanisms are used to achieve a variety of strength, ductility, toughness and fatigue properties. In the automotive industry, AHSS are used in load-bearing components, bumper systems, battery protection, door joists, etc. Several types of AHSS have been given attention to since the 1970s. Dual-phase (DP) steels were the first AHSS presented. In addition to the desired properties regarding strength and ductility, only a simple thermomechanical treatment is necessary to create DP steels. Other advanced high-strength steels exist today, such as transformation-induced plasticity (TRIP) and twinning-induced plasticity (TWIP) steels, which have superior ductility without the expense of reduction of strength compared to DP steels. However, disadvantages such as more complex thermomechanical treatment, welding and casting issues limit the use of such AHSS, and DP steels are often preferable (Fonstein 2015).

DP steels have a microstructure that mainly consists of two phases, where martensite islands are randomly distributed in a ferrite matrix. The ferrite phase is soft, ensuring early yield and great ductility, while the martensite phase is brittle and contributes with high strength. Several grades of DP steel exists today and the

most familiar types are DP500, DP600, DP800 and DP1000. The number indicates ultimate tensile strength of the DP steel, and the ductility decreases with the increase of the ultimate tensile strength. Furthermore, the DP steels are known for their continuous yield, low yield to ultimate tensile strength ratio, and high initial work-hardening rate (Tasan et al. 2015). These characteristics ensure distribution of the plastic deformation, which is important when considering the energy absorption during crash situations.

Important parameters that affect the properties of DP steels are the martensite volume fraction, distribution of martensite islands, carbon content, ferrite and martensite grain size and shape. The investigation of how these parameters affect the properties of DP steels is extensive (e.g. Abid et al. (2017), Bag et al. (1999), Jiang et al. (1995), Pierman et al. (2014)). Significant progress has been accomplished the last decades due to systematic investigation of the parameters, but also the development of the experimental and the numerical methods are important factors for these achievements. For instance, micromechanical finite element (FE) simulations and representative volume elements (RVE) are frequently used to model the microstructure. An RVE is a material volume that has the general characteristics of the whole microstructure, but is small enough to be computationally efficient. This progress has made it possible to study how the phases interact with each other. Moreover, it is possible to obtain new information about the stress fields and how the energy distributes in the microstructure, which increase the understanding of yielding, work-hardening, and fracture in DP steels.

It is a desire that numerical simulations could eventually be used instead of experimental studies, since laboratory tests are costly to carry out. For instance, the number of tests a new car goes through before it is approved can be greatly reduced if the corresponding numerical simulations are sufficiently accurate. However, it is a challenge to capture the complex material behaviour in the material model used in the simulations. An appealing approach may be to use the micromechanical FE simulations as a basis. The micromechanical FE simulations are too computationally expensive to directly be used in large scale simulations. However, the plasticity and fracture behaviour from the micromechanical FE simulations may be used in the large scale material models (Kouznetsova 2002).

The objective of this thesis is to use micromechancical FE simulations to study

how yielding, work-hardening, and ductile fracture are influenced by the martensite volume fraction and distribution in DP steels. Laboratory tests are conducted to investigate the Bauschinger effect as a function of martensite volume fraction in DP steels by using a specially designed anti-buckling device. Material models are established for DP steels with different martensite volume fraction based on the plasticity and fracture experienced in experimental work and micromechanical FE simulations. An overview is presented in the following.

In Chapter 2, a brief overview of the state of the art of the topic is given. The microstructure, the mechanical behaviour, and the microstructure-based modelling and simulation of DP steels are covered. The objective is to give an introduction to DP steels and present some of the latest, most relevant research done in this field relevant to this study.

All of the methods that are used are presented in Chapter 3. The three different experiments used in this study are introduced. The cyclic load tests conducted in this study are presented in detail, while only a brief overview of the uniaxial tension and central hole experiments conducted in advance of this study is given. The post-processing of the experimental data and the different numerical models used then follow. The construction of the RVEs is described in detail such that it should be possible to repeat the study.

The results and discussion from the cyclic load laboratory tests are presented in Chapter 4. An evaluation of the anti-buckling device is first presented before the findings regarding how the martensite volume fraction influences the Bauschinger effect in DP steels are addressed. Similar chapters for the uniaxial tension and central hole experiments are omitted since they were conducted in advance of this study.

The contents in the following chapters cover the establishment of the micromechanical FE framework for plasticity and fracture of DP steels and are presented in Figure 1.1, where the numbers signify the chapters where the corresponding step is covered. Chapter 5 contains preliminary sensitivity studies and addresses the issue of volumetric locking. The numerical study of yielding, work-hardening and ductile fracture of DP steels is presented in Chapter 6. Yielding and work-hardening of DP steels in uniaxial tension are considered in Section 6.1, where the behaviour of

different RVEs are examined with focus on the role of martensite volume fraction and its distribution. Section 6.2 and 6.3 consider yielding in different stress states (iso-curves) and the kinematic hardening obtained by using the different RVEs, respectively. In Section 6.4, fracture in the DP steel is considered. Here, the objective is to investigate the fracture mechanics in the RVEs. Lastly, in Chapter 7 a micro-macro homogenization procedure is presented, where the behaviour of the highly heterogeneous microstructure of DP steels is homogenized. The Gurson model is utilized to represent the void evolution where both initial voids and void nucleation are studied. A homogenization process is established in order to use the micromechanical results in large scale simulations.

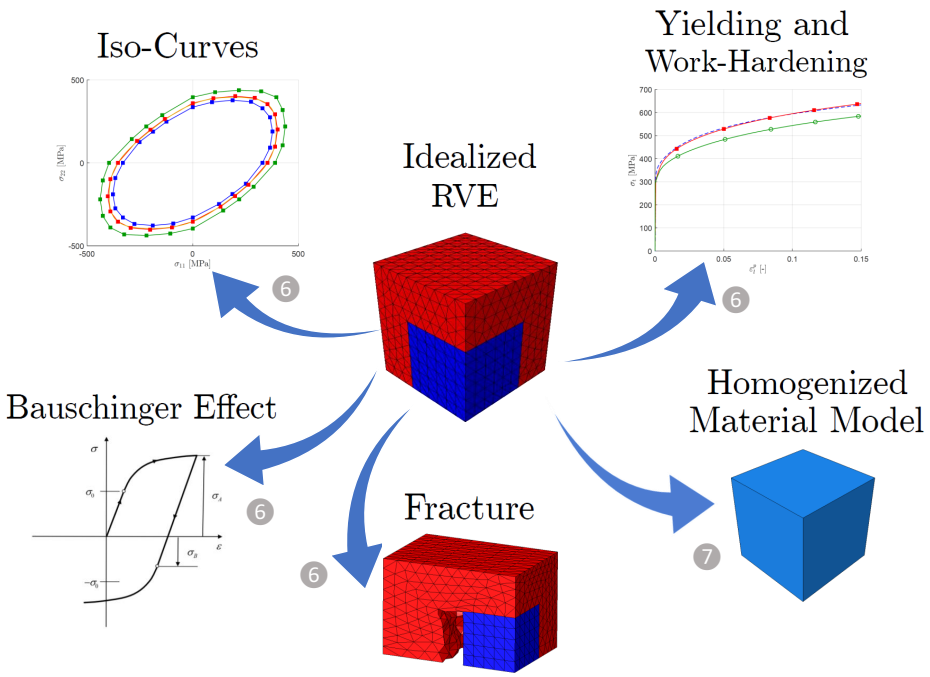

Figure 1.1: An overview of the micromechanical FE modelling conducted in this thesis. The idealized RVEs are the basis. Yielding and work-hardening of the RVEs are presented in Section 6.1. The RVEs are used to obtain iso-curves for yielding, to investigate kinematic hardening, and to consider ductile fracture in Section 6.2, 6.3 and 6.4, respectively. Then, material models for the DP steels are calibrated by conducting a homogenization procedure in Chapter 7.

2 State of the Art

A literature review covering the microstructure, the mechanical behaviour and microstructure-based modelling and simulation of DP steels is presented in this chapter. It includes basic theory on DP steels in addition to an overview of the state of the art research. Since the research of DP steels is extensive and the objective of this literature review is to provide an overview, only a limited number of references are included.

2.1 Microstructure of DP Steels

DP steels have a two-phase microstructure, where the strength comes from the hard martensite phase, which is dispersed in a soft ferrite matrix. Figure 2.1 shows typical microstructures of DP steel of different quality and martensite volume fraction, where the ferrite and the martensite are the dark and the light parts, respectively. Typically, the martensite volume fraction, V_m, varies between 10 and 50% in DP steels. A DP steel microstructure could be obtained by a simple thermomechanical treatment, as shown in Figure 2.2. In this case, a ferrite-pearlite ($\alpha + Fe_3C$) microstructure is heated to an intercritical annealing temperature (a temperature between A_1 and A_3 in Figure 2.2), where a ferrite-austenite ($\alpha + \gamma$) microstructure appears. The temperature is held constant for a few minutes before the microstructure is quenched below the martensite start temperature (M_s). Then, the austenite transformes to martensite, α', and the ferrite-martensite microstructure is obtained.

In addition, small amounts of pearlite, bainite and austenite may be present in the microstructure depending on the heating process. The obtained ferrite-martensite microstructure can be controlled by changing the intercritical annealing temperature, heating rate to this temperature and the cooling rate. According to Mazinani & Poole (2007), the martensite volume fraction and the size of the martensite islands increase with the intercritical annealing temperature. Further, it was stated that the morphology changed when the heating rate to this intercritical annealing temperature was increased. Equiaxed and elongated martensite islands were ob-

tained when low and high heating rates to this temperature were used, respectively. Additionally, a high cooling rate is necessary in order to transform all the austenite into martensite.

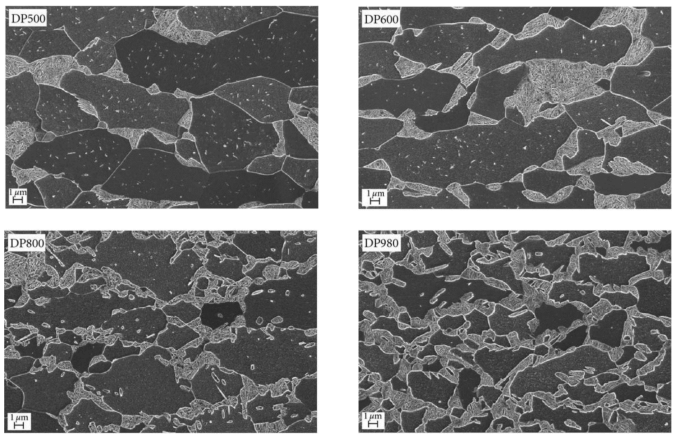

Figure 2.1: Microstructure of Docol 500DP, 600DP, 800DP and 1000DP. The ferrite phase is dark, while martensite phase is light.

Alloying elements are introduced to improve the properties of DP steels. The most important is carbon, which increases both the yield stress and ultimate tension stress. The amount of carbon in DP steels is often in the range of 0.06-0.15-wt%. About 1.3-3% manganese is included in DP steel to obtain solid-solution strengthening in the ferrite. Other elements that can occur in DP steels are chromium and molybdenum to hold back the formation of pearlite; silicon to facilitate the ferrite transformation; and vanadium and niobium for microstructure refinement and precipitation strengthening (Tasan et al. 2015).

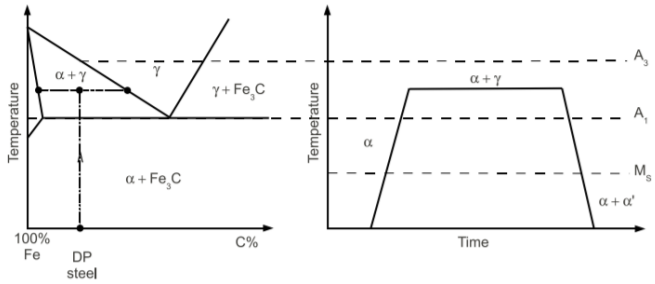

Figure 2.2: How to obtain a typical ferrite-martensite microstructure. The left figure shows a schematic phase diagram for steel. The right figure shows a thermal treatment (Landron 2011).

2.2 Mechanical Behaviour of DP Steels

The mechanical behaviour of DP steels depends on the properties of the soft ferrite phase and the hard martensite phase. In addition to its composition, the behaviour of the ferrite phase depends on the grain size. It is reported by Jiang et al. (1995) that the effect of ferrite grain size in DP steels follows the Hall-Petch relation. Meaning, both the yield stress and ultimate tensile strength of DP steels are inversely proportional to the ferrite grain size. The influence of carbon content on the martensite strength is frequently investigated in the literature. An experimental study was conducted by Pierman et al. (2014). The study showed that the yield stress of the martensite phase was independent of the martensite carbon content, while the ultimate tensile strength increased. However, it is often assumed linear relationships between both the yield stress and ultimate tensile strength and the carbon content as a simplification (Byun & Kim 1993, Concepcion et al. 2015, Leslie 1981).

The mechanical behaviour of DP steels does not only depend on the properties of the ferrite and martensite itself, but the morphology and their volume fraction are also key microstructural characteristics. In general, it is established that the martensite volume fraction increases the ultimate tensile strength and decreases the ductility of the DP steel (Byun & Kim 1993, Davies 1978, Peng-Heng & Preban 1985, Pierman et al. 2014). Furthermore, Bag et al. (1999) investigated the influence of martensite volume fraction in an experimental study. It was reported that the strength of the DP steel increased with the martensite volume fraction up to

55%, where a further increase of martensite volume fraction reduced the strength. Several experimental studies have investigated the influence of martensite morphology. It is reported that elongated martensite phases are beneficial for strength and ductility compared to equiaxed martensite particles, since the martensite particles to a greater extent constrain the plastic flow in the ferrite phase (Abid et al. 2017, Adamczyk & Grajcar 2007, Pierman et al. 2014).

As previously mentioned, the continuous yield of DP steels is a beneficial property. It is caused by the volume expansion that occurs during austenite to martensite transformation. Martensite has a body centred cubic (BCC) or a body centred tetragonal (BCT) crystal structure while austenite has a face centred cubic (FCC) crystal structure. This expansion causes residual stresses in the microstructure to occur, which leads to geometrically necessary dislocations at the ferrite-martensite interfaces. The number of dislocations increases with the volume fraction of martensite and leads to an increasingly smooth flow curve. This is the reason for why the stress-strain curves of DP steels do not have the characteristic yield point elongation of conventional steels, but rather a continuous yielding (Amirmaleki et al. 2016, Kadkhodapour et al. 2011). Furthermore, the yield surface of DP steels has been investigated in the literature. Hou et al. (2019) described the evolution of yield behaviour for DP590, DP780 and DP980 experimentally. It was stated that an anisotropic yield criterion and a non-associated flow rule were necessary to accurately describe the behaviour.

Cyclic loading is frequently investigated in order to determine the Bauschinger effect in a material. The Bauschinger effect is recognized as early yield after load reversal, and it has several contributions. For instance, the Bauschinger effect may appear in polycrystalline materials due to a so-called Masing effect. The orientation of the polycrystals causes yield to not occur simultaneously in every grain, and the amount of plastic flow in the different crystals varies. This gives rise to residual stresses in the material, which contributes to the Bauschinger effect when the load is reversed. It is also reported that the Bauschinger effect could appear in single crystals (Kocks & Mecking 2003, Milligan et al. 1966). Regarding the Bauschinger effect in DP steels, a compression-tension load experimental study was conducted by Yoshida et al. (2002), which revealed that DP590 exhibited a Bauschinger effect. Another experimental study conducted by Erdogan & Priestner (2002) investigated the effect of martensite content and prestrain (the strain

before load reversal) on the Bauschinger effect in DP steels. A lower Bauschinger effect with 18% martensite volume fraction than with 25% was reported. Additionally, it was found that whether the load started in tension or compression had no influence on the Bauschinger effect, and that the Bauschinger effect increased when the prestrain increased from 0.4% to 2.2%.

The DP steels fracture in a ductile manner, and the fracture mechanism is characterized by nucleation, growth and coalescence of voids. According to Paul (2013), fracture in DP steels is caused by the incompatible deformation between the two phases. The strain in the soft ferrite localizes close to the hard martensite particles where the voids nucleate either by martensite particle cracking or ferrite-martensite decohesion. Generally, particle cracking dominates when the material matrix is hard, while decohesion of the particle-matrix interface often occurs in materials with softer matrix. Ahmad et al. (2000) found that for DP steels where the martensite volume fraction is low, decohesion is the primary mode, while for higher martensite volume fractions, the martensite particle cracking is the main mode. The void evolution continues with void growth as the plastic strain increases, where the stress triaxiality and the Lode parameter have been shown to be important parameters. The stress triaxiality is the ratio between the hydrostatic stress and the von Mises equivalent stress, while the Lode parameter describes the deviatoric stress state. The plastic strain to failure decreases when the stress triaxiality and Lode parameter increases and decreases, respectively (Dunand & Mohr 2014, Gruben et al. 2013, Hancock & Mackenzie 1976, Hopperstad et al. 2003). Lastly, the growing voids coalesce, which accelerates the void evolution, and could be considered as a precursor for failure (Garrison & Moody 1987).

2.3 Microstructure-Based Modelling of DP Steels

When modelling DP steels, special attention should be given to the microstructure. This is important because the behaviour of DP steels depends heavily on the microstructure. As a result of this, a micromechanical modelling technique called the representative volume element (RVE) method is often used when modelling DP steels. An RVE is a small representative volume of the microstructure of a multi-phase material in which the different phases are modelled with their respective characteristics such as volume fraction, morphology and plasticity. It could be considered as a volume large enough to represent the macroscopic properties of

interest, but small enough to be computational efficient. Through RVE modelling, the general characteristics of the entire microstructure of the material should be described properly (Thomser et al. 2009, Uthaisangsuk et al. 2011).

The RVE method facilitates a clear connection between the microscopic properties, such as chemical composition, volume fraction, morphology and grain size, and the macroscopic properties, such as Young's modulus, yield stress, hardening and Bauschinger effect (Tasan et al. 2015). This allows for streamlined parametric studies of the micromechanical effects of the microstructure. Micromechanical modelling using the RVE method can be summarized in four steps; defining the RVE, defining mechanical behaviour of each material phase, application of boundary conditions and simulation of deformation, and homogenization (Amirmaleki et al. 2016). There are many ways of executing these steps, and methods based on newer works are presented below. In addition, methods of microstructure-based modelling of fracture are proposed.

In general, there are two different methods of representing the RVE. The first method generates RVEs based on the microstructure observed by use of microscopy. By use of this, the phase fraction and distribution of martensite and ferrite can be described properly in the RVEs. Because two dimensional (2D) modelling requires less computational power than three dimensional (3D) modelling, a considerable amount of research has been devoted to 2D RVEs (Amirmaleki et al. 2016, Ramazani, Schwedt, Aretz, Prahl & Bleck 2013). However, it is reported that 3D modelling is more accurate as the 2D RVEs underestimated the flow curves (Ramazani, Mukherjee, Quade, Prahl & Bleck 2013, Uthaisangsuk et al. 2011). For 3D RVEs, an effective approach is to model the DP steel as a matrix of the ferrite phase with a distribution of inclusions of the martensite phase (Mori & Tanaka 1973). Here, the 3D RVE is generated based on the average microstructure of the phase map from scanning electron microscopy (SEM) (Ramazani et al. 2012, Saai 2019). Amirmaleki et al. (2016) did this to generate 3D RVEs. The 3D RVEs resembled the actual microstructure in terms of martensite morphology in a statistical sense, and resulted in an accurate model. This method can, however, lead to large RVEs if the microstructure is highly irregular. Examples of RVEs based on real microstructure are shown in Figure 2.3 and 2.4 for a 2D and a 3D RVE, respectively.

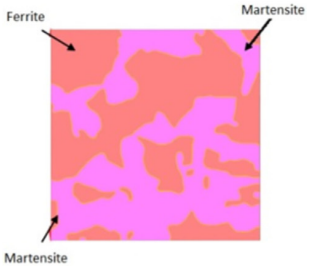

Figure 2.3: 2D RVE based on real microstructure obtained from scanning electron microscopy (Uthaisangsuk et al. 2011).

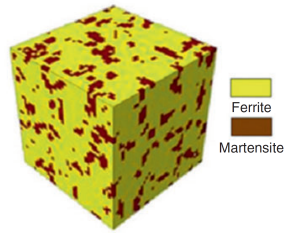

Figure 2.4: 3D RVE based on real microstructure (Ramazani, Mukherjee, Quade, Prahl & Bleck 2013).

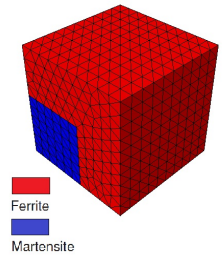

Figure 2.5: Example of an idealized 3D RVE with only one martensite particle. Such an approach is used herein.

The second method is defining the smallest RVE where the macroscopic properties can be represented. These RVEs are in general smaller than those created through statistical representation (Kouznetsova 2002). This method allows for simplistic and idealized RVEs that are less computationally demanding, like the one shown in Figure 2.5.

The second step when using RVEs is to define the phase characteristics, where it is often assumed that the plasticity of the two phases can be modelled separately. To model the plasticity of both phases in the DP steels, dislocation based modelling is often used as it takes into account the intra-phase micromechanical attributes. A commonly used dislocation based model for defining the flow behaviour of both phases was developed by Rodriguez & Gutiérrez (2003). They defined the flow stress of the single phase, σ, as a function of equivalent plastic strain, p, as

$$\sigma = \sigma_0 + \Delta\sigma_c + \alpha \cdot M \cdot \mu \cdot \sqrt{b} \cdot \sqrt{\frac{1 - \exp(-Mk_r p)}{k_r \cdot L}} \tag{2.1}$$

where σ_0 takes lattice friction based upon chemical composition into account (Buessler 1999). Added strength from precipitations and carbon in the solution is included through $\Delta\sigma_c$. Additionally, α is a constant, M is the Taylor factor, μ is the shear modulus and b is Burgers vector. The recovery rate, k_r, and the dislocation mean free path, L, are also included (Bergström 1970). The final term constitutes the work-hardening in the material.

In the third step when using an RVE, boundary conditions are applied. Boundary conditions are important as they impose the constraints that allow the RVEs to be compatible with themselves. There are two different boundary conditions commonly used; namely homogeneous and periodic boundary conditions. Homogeneous boundary conditions ensures either no displacements or no slope at the boundary (Chang 2015). Periodic boundary conditions allow the RVE to have an arbitrary deformation on the boundary, but constrain the boundary to allow for an arrangement of periodic RVEs. This is done by constraining the displacements of the nodes on the boundary to be compatible with the displacements of the corresponding nodes on the opposite boundary. This is shown in Figure 2.6 with the pairs of equivalent edges A-B, C-D and E-F. When the RVEs are stacked periodically, equivalent nodes from two neighbouring RVEs will move in unison and the boundary between the RVEs will coincide (Nygårds & Gudmundson 2002). Ramazani et al. (2012) showed the influence of choosing either homogeneous or periodic boundary conditions. For both boundary conditions, the solution converged when the size of the RVE and the number of martensite islands increased. Further, it was shown a slower convergence and overestimation of the stress-strain curve when homogeneous boundary condition was used compared to periodic boundary condition.

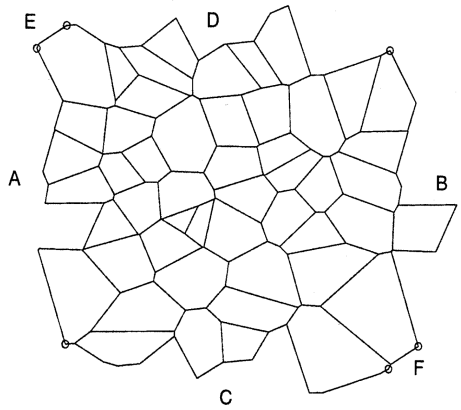

Figure 2.6: An RVE with three pairs of equivalent edges; A-B, C-D and E-F, where the ends of the edges are marked by circles (Nygårds & Gudmundson 2002).

To apply loading to the RVE, Nygårds & Gudmundson (2002) proposed the use of dummy nodes. These dummy nodes have degrees of freedom that corresponds to the average strains, $\overline{\varepsilon}_{ij}$, obtained at the macroscopic level. The dummy nodes are

then coupled with the nodal degrees of freedom at the boundaries. The coupling is done through the Equation (2.2), where α and β are equivalent nodes as explained above, while u_i is the displacement vector and x_j is the position vector. The same nodes that are used to impose the displacement are also used to extract the average stresses through reaction forces.

$$u_i^{\beta} - u_i^{\alpha} = \bar{\varepsilon}_{ij}(x_j^{\beta} - x_j^{\alpha}). \tag{2.2}$$

The final step in the micromechanical modelling is the homogenization strategy. This step relates the micro-scale behaviour of the RVEs to the macro-scale behaviour of the material. The main difference between the micro-scale and macro-scale is that in the macro-scale, the material can be assumed homogeneous, but in the micro-scale it is highly heterogeneous. Thus, the non-uniform stress and strain fields in micro-scale are averaged in order to obtain uniform stress and strain in macro-scale. The first-order homogenization procedure could be used to include micromechanical modelling into large scale simulations, and it can be broken down into the three following steps.

The first step is to calculate the deformation at every macroscopic integration point. This deformation is used to impose boundary conditions on the RVEs at micro-scale. The next step is to solve the boundary value problems at the micro-scale by using the corresponding RVE at that material point. In the final step, the solution to the boundary value problem is used to calculate the macroscopic average stresses as explained earlier. Figure 2.7 illustrates these three steps. Through this homogenization procedure, the stress-strain relation on the macro-scale is obtained (Kouznetsova 2002). This homogenization procedure is computationally heavy, especially for 3D RVEs. Therefore, it may be beneficial to use the micro-scale modelling only to calibrate the characteristics of a homogeneous material model to be used at the macro-scale.

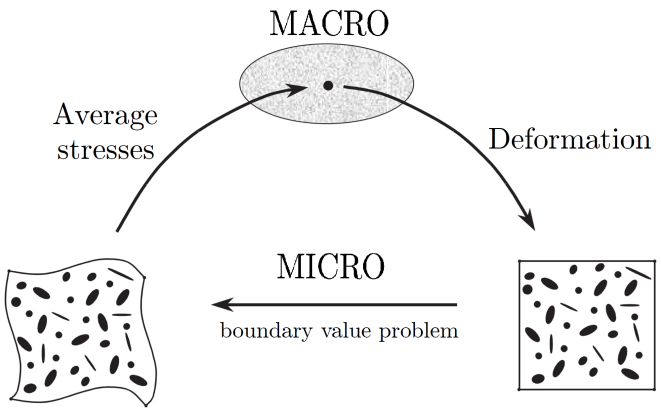

Figure 2.7: First-order computational homogenization procedure (Kouznetsova 2002).

Several numerical studies have been conducted with an RVE to investigate fracture in DP steel. In the following, an introduction of some often used approaches based on an RVE are presented. However, only details regarding the Gurson model are given. It is frequently stated in the literature that strain localization caused by the incompatible deformation between the ferrite and martensite phase could be considered as a precursor to failure. Thus, the influence of stress state on the failure mode and ductility in DP steels has been investigated by considering the plastic strain localization in an RVE (Paul 2013, Sun et al. 2009). Both the failure mode and ductility were found to depend on the stress state.

Other numerical studies introduce damage models in the different phases in order to reproduce the reported failure mechanisms. For instance, the Gurson-Tvergaard-Needleman porous plasticity model introduces material softening in the RVE, while cohesive zone modelling could be used to control the ferrite-martensite decohesion or martensite particle cracking. In combination with a cohesive zone model, Uthaisangsuk et al. (2009) used the Gurson-Tvergaard-Needleman model to estimate the void evolution in the ferrite matrix and to describe the ferrite-martensite decohesion. West et al. (2012) used the Gurson-Tvergaard-Needleman model to calibrate a damage model for DP steels. Ramazani, Schwedt, Aretz, Prahl & Bleck (2013) used cohesive zone modelling in the martensite phase to represent the observed martensite cracking for a DP steel with 46% martensite volume fraction.

As indicated above, porous plasticity models could be used to represent the effect of void evolution in a material. In such cases, the work-hardening of the material matrix is countered by the material softening due to void growth. Porous plasticity models are called coupled damage models since they introduce damage into the constitutive relations. An example is the Gurson model, where the void volume fraction, $f = \frac{V_f}{V_f+V_M}$, is added to the yield criterion. V_f and V_M are the total volume of voids and matrix material, respectively. It was first proposed by Gurson (1977), but it was later modified by Chu & Needleman (1980), Tvergaard (1981) and Tvergaard (1982) in order to take void nucleation and coalescence into account. The yield criterion, Φ, is shown in Equation (2.3) and is known as the Gurson-Tvergaard-Needleman (GTN) model. Several other extensions of the Gurson model have been published to improve the performance of the model in other stress states. For instance, Madou & Leblond (2012) extended the Gurson model to improve the performance at low stress triaxialities. However, the extensions increase the complexity of the yield criterion and are not discussed herein.

$$\Phi = \left(\frac{\sigma_{eq}^{VM}}{\sigma_M}\right)^2 + 2q_1 f^* \cosh\left(\frac{3}{2} q_2 \frac{\sigma_H}{\sigma_M}\right) - 1 - q_3 f^{*2} \leq 0. \tag{2.3}$$

The damage parameters q_1, q_2 and q_3 in Equation (2.3) were introduced by Tvergaard, and $q_1 = 1.5$, $q_2 = 1.0$ and $q_3 = {q_1}^2$ were proposed as standard values for metals. σ_{eq}^{VM} and σ_H are the macroscopic von Mises equivalent stress and hydrostatic stress, while σ_M is the flow stress of the matrix material. The effective void volume fraction, f^*, includes the decrease of load-carrying capacity associated with void volume fraction and void coalescence, and is explained when Equation (2.8) is presented. The void evolution, $\dot{f}$, in the GTN model is described by

$$\dot{f} = \dot{f}_n + \dot{f}_g. \tag{2.4}$$

The former term, $\dot{f}_n$, denotes the void evolution caused by nucleation of voids and the latter, $\dot{f}_g$, represents the void growth and is described by

$$\dot{f}_g = (1 - f)\dot{\varepsilon}_v^p, \tag{2.5}$$

where $\dot{\varepsilon}_v^p = \frac{\dot{V}_f}{V}$ is the plastic volumetric strain rate. The nucleation could either be stress- or strain-driven. However, only a strain-driven nucleation is available in

Abaqus (ABAQUS 2019), and is described as

$$\dot{f}_n = A(\varepsilon_M^p)\dot{\varepsilon}_M^p, \tag{2.6}$$

where ε_M^p is the plastic strain of the matrix material and

$$A(\varepsilon_M^p) = \frac{f_N}{s_N\sqrt{2\pi}} \exp\left[-\frac{1}{2}\Big(\frac{\varepsilon_M^p - \varepsilon_N}{s_N}\Big)^2\right]. \tag{2.7}$$

Evidently, Equation (2.7) is a normal distribution with the three statistical parameters f_N, s_N, and ε_N, which are the volume fraction of void-nucleating particles, the associated standard deviation and expected plastic strain at nucleation, respectively.

Void coalescence is accounted for in the GTN model by the effective void volume fraction, f^*. The void evolution is accelerated beyond a critical void volume fraction, f_c, and all stress carrying capacity is lost when the void volume fraction at fracture, f_F, is reached. f^* is defined as

$$f^* = \begin{cases} f & \text{if } f \leq f_c \\ f_c + \frac{(\bar{f}_F - f_c)}{f_F - f_c}(f - f_c) & \text{if } f_c < f < f_F, \quad \bar{f}_F = \frac{q_1 + \sqrt{q_1^2 - q_3}}{q_3} \\ \bar{f}_F & \text{if } f \geq f_F. \end{cases} \tag{2.8}$$

Throughout this study, it is varied whether or not the void nucelation and void coalescence are included in the model. Thus, the model is not called GTN model herein, but consequently denoted as the Gurson model.

3 Methods

Both experimental and numerical methods used in this study are described in this chapter. The experimental methods are presented first. Then follow the numerical methods, focusing on the plasticity and fracture of DP steels. The numerical methods section is composed of the use of different representative volume elements. Which representative volume elements that were used and how they were established are presented first. The application of them follows where yielding, work-hardening, fracture and micro-macro transition are the main topics. The same sequence of topics is maintained throughout the thesis.

3.1 Experiments

In this study, experimental data from uniaxial tension tests (UT), central hole tests (CH), and cyclic load tension-compression tests were used. The two former tests were conducted in advance of this study by the research group SIMLab (SIMLab 2020), and the data were supplied by Postdoctoral Researcher Maria Jesus Perez Martin. It is emphasized that these experiments were not conducted by the authors of this study, and few details regarding these test procedures are given. The cyclic load tension-compression tests were conducted in this study, and of that reason, a more detailed description of the procedure follows. That being said, except for the anti-buckling device used in the cyclic load tests, the steps in the different tests resemble each other. Meaning, the details presented below are to a great extent also applicable for the uniaxial tension tests and the central hole tests. The shape of the specimens are shown in Figure 3.1.

The cyclic load laboratory tests were conducted in order to investigate the effect of load reversal in DP steels, where the influence of martensite volume fraction on the Bauschinger effect was of particular interest. The DP steels tested were Docol 500DP, 600DP, 800DP and 1000DP. The shape of the specimens is shown in Figure 3.1 to the right. It was chosen to obtain uniformly distributed strains over the gauge length without experiencing buckling during compression. In general, the specimens were loaded both in tension and compression during the tests, and

a specially designed anti-buckling device was utilized to prevent buckling during compression. The anti-buckling device was similar to the one used by Marcadet & Mohr (2015), and is depicted in Figure 3.2. The device consisted of three plates, six springs and six bolts, and the specimens and the spacers were clamped by use of high pressure grips.

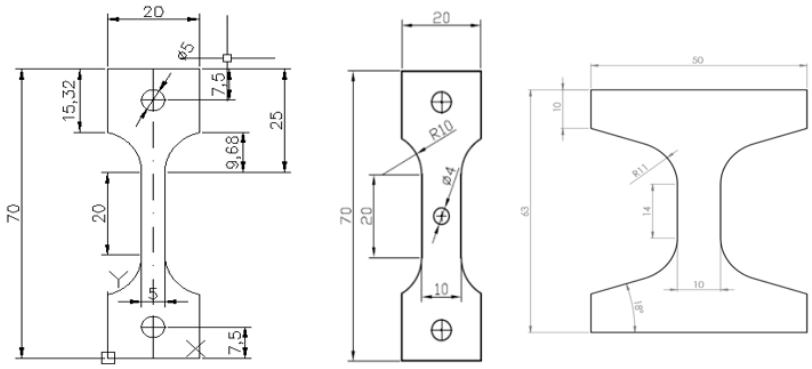

Figure 3.1: Drawing of the specimens used in the uniaxial tension tests (left), central hole tests (middle), and the cyclic load tests (right).

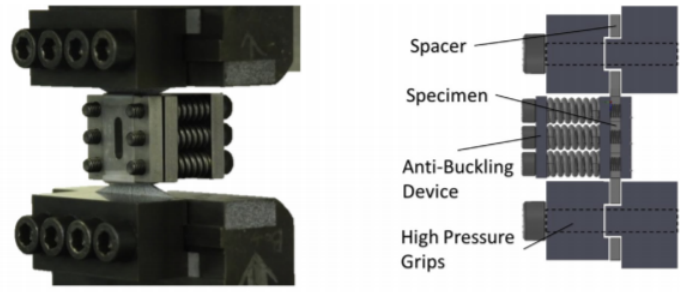

Figure 3.2: Drawing of the anti-buckling device (Marcadet & Mohr 2015).

As Figure 3.2 shows, the plates and the springs provided pressure in the slender part of the specimens. To be consistent with Marcadet & Mohr (2015), the desired transverse pressure for Docol 800DP was 3 MPa. Linear interpolation gave the desired transverse pressures for the other steel qualities, which were 3.75 MPa, 2.25 MPa and 1.88 MPa for Docol 1000DP, 600DP and 500DP, respectively. In the experiments however, the transverse pressure was limited by the length of the threaded part of the bolts. The applied transverse pressure was 2.47 MPa for all steels except for Docol 500DP, where the applied pressure was 1.75 MPa. Fur-

thermore, the plates were provided with an opening in the centre. This was due to the desire to utilize Digital Image Correlation (DIC) to accurately capture the displacement in the gauge area. Teflon tape was used on the two plates in contact with the specimens to lower the friction.

Prior to testing, the area of the specimens in the gauge length was measured with a micrometer with an accuracy of ± 0.01 mm. The width of all specimens was 10.00 mm. The thickness of Docol 500DP was 1.90 mm, while for Docol 600DP, 800DP and 1000DP it was 1.02 mm. Further, the specimens were sandpapered in the clamped areas to create better grip, and they were washed with alcohol to rinse away the rust on the surface. After the specimens were mounted in the anti-buckling device they were painted with a black and white speckle pattern in the opening to facilitate a 2D DIC. Pictures were taken with a frequency of 1 Hz by two high resolution cameras during testing. Both of them were located perpendicular to the plane of motion, where one of them captured the motion of the whole specimen, while the other only captured the motion in the gauge area. The cameras used were of type BASLER acA2440-75. Both on left and right side of the cameras, lights were mounted in order to reduce the shadow in the gauge area caused by the anti-buckling device.

The machine conducting the tests was an Instron 5985 with a 100 kN load cell. The load cell measured applied force with a frequency equal to that of the cameras. To achieve quasi-static loading conditions, the desired nominal strain rate in each test was set to $\dot{\varepsilon} = 5 \cdot 10^{-4} 1/\text{s}$. Thus, the displacement rate of the tests was $v = 0.42$ mm/min. Five specimens of each DP steel quality were at disposal. In general, four load reversal tests were conducted for each DP steel quality, where the magnitude of prescribed displacement varied. For these tests, two cycles of load reversal were done. In the first three tests, the specimens were first compressed and then stretched in tension, before the loading sequence was repeated. The fourth test started in tension and was then compressed. The fifth specimen for Docol 500DP and 800DP was spent when the clamping system was calibrated. For Docol 600DP and 1000DP, the fifth specimen was loaded in tension until fracture with the anti-buckling device detached.

The first test was conducted with a specimen of the Docol 800DP where the prescribed displacement was -1 mm in compression and then stretched to 0.5 mm in

tension. The applied torque on the bolts in the high pressure grips was 8 Nm, and resulted in slipping. Further, the torque was through trial and error incrementally increased to 32 Nm, where no slipping of the specimen was observed. The subsequent tests were successfully conducted with a torque of 32 Nm, and the loading sequences are listed in Table 3.1. Except for Docol 800DP, two specimens of each steel quality were at disposal after successfully completing the three first load reversal tests. The first experiment with load reversal, which started with tension (Docol 500DP, RL4), failed because of slipping. From this point on, the torque on the bolts was increased to 50 Nm. Further, one tension-compression load reversal test of each steel quality was successfully completed. The two remaining specimens were of type Docol 600DP and 1000DP, and were used to conduct pure tension to fracture experiments without the anti-buckling device. This was done in order to evaluate the effect of the anti-buckling device. Of 20 possible tests, 18 valid experimental data sets were obtained from the experiments: Four data sets from Docol 500DP and 800DP, and five data sets from Docol 600DP and 1000DP.

Table 3.1: Loading sequence of the different tests with respect to prescribed displacement. As an example, -1 to 0.5 means that specimen first was loaded to -1 mm in compression then stretched to 0.5 mm in tension.

Test	Docol 500DP [mm]	Docol 600DP [mm]	Docol 800DP [mm]	Docol 1000DP [mm]
RL1	-1 to 0.5	-0.8 to 0.4	Failed	-0.8 to 0.4
RL2	-0.8 to 0.4	-0.6 to 0.3	-1 to 0.5	-0.6 to 0.3
RL3	-0.5 to 0.25	-0.4 to 0.2	-0.8 to 0.4	-0.4 to 0.2
RL4	Failed	2 to 0	-0.5 to 0.35	1.5 to 0
RL5	2 to 0	-	1.5 to 0	-
T1	-	Tension to Fracture	-	Tension to Fracture

3.2 Post-Processing Experimental Data

DIC was used in order to obtain sufficient accuracy of the displacements within the specimens for all the tests. It measures the displacement by tracing the movement in the black and white speckle pattern. In this case, eCorr (Fagerholt et al. 2013, Fagerholt 2019) has been used. The tracing was done by meshing the specimen in the initial frame, where the specimen was not yet loaded. Having a finely meshed grid allows for accurate representation of high displacement gradients, but it introduces grey-value noise. On the other hand, a coarse mesh negates the grey-value noise, but it is less accurate and it is unable to represent the same gradients as a

fine mesh. Of this reason, both a coarse (50 x 50 pixels) and a fine mesh (25 x 25 pixels) were tested initially to ensure that the results of the analysis was not mesh dependent. Resultingly, the fine mesh was used for every analysis.

Further, to minimize the effect of noise in grey-values, a vector over the gauge length of the specimens was used to obtain the elongation of the specimens. When possible, a vector with initial length of 11 mm was chosen for the cyclic load specimens. Both a global and a local extensometer were used when post-processing the uniaxial tension tests and the central hole tests in order to capture both the overall and localized behaviour. The global vector covered the whole gauge length with a vector length of 20 mm. The local vector length was 2 mm and the vector was located in the diffuse neck in the uniaxial tension tests and at one of the sides of the central hole in the central hole tests. In the tests with the anti-buckling device attached, a couple of restricting phenomena occurred occasionally. Firstly, when the specimens were deformed to a certain extent, parts of the speckle-pattern moved out of the well-lit zone. The second phenomenon was that the front plate cast shadows in the semicircle parts of the window. These phenomena were circumvented by the use of a shorter vector, which should not have a consequential effect on the overall accuracy.

Thus, the output from the DIC in this case was the engineering strain, ε_e, of the defined vector. The corresponding engineering stress, σ_e, was obtained by use of force, F, measurements from the testing machine and the initial measured area, A_0, of the specimens.

$$\sigma_e = \frac{F}{A_0}. \tag{3.1}$$

In uniaxial tension and compression, the true stress, σ_t, and logarithmic strain, ε_l, up to necking were obtained by use of the following equations.

$$\sigma_t = \sigma_e(1 + \varepsilon_e), \quad \varepsilon_l = \ln(1 + \varepsilon_e). \tag{3.2}$$

Further, the plastic strain, ε_l^p, was calculated by use of strain decomposition and one dimensional (1D) Hooke's law. E denotes the Young's modulus.

$$\varepsilon_l^p = \varepsilon_l - \frac{\sigma_t}{E}. \tag{3.3}$$

Engineering stress-strain, true stress-strain, and true stress vs. plastic strain curves were created depending on the tests. All mathematical operations and plotting were done by use of MatLab (MathWorks 2020).

In the cyclic load tests, the equivalent stress and plastic strain were used to evaluate the kinematic hardening. In uniaxial tension and compression the equivalent stress was defined as $\sigma_{eq} = |\sigma_t|$. The equivalent plastic strain was obtained by assuming associated flow rule and that it was work conjugate to the equivalent stress. In uniaxial tension and compression, the increment of the equivalent plastic strain then becomes $dp = |d\varepsilon_l^p|$. In general, yield was defined to start at a plastic strain of 0.2%. Because of a cyclic load, there were multiple points of onset of yield. From the preceding point of load reversal, the next yield point was defined as the point when the increase in equivalent plastic strain, p, equals 0.002. Knowing the stresses at the yield points and the points of load reversal, the difference in stress between load reversal and the following yield was found. This difference was used to calculate a ratio that illustrates the magnitude of the Bauschinger effect. This relation is denoted the r-ratio, and is calculated by

$$r = \frac{2\sigma_A - (\sigma_A - \sigma_B)}{2\sigma_A} = \frac{\sigma_A + \sigma_B}{2\sigma_A}, \tag{3.4}$$

where σ_A is the stress at load reversal and σ_B is the stress at yield after load reversal, as shown in Figure 3.3.

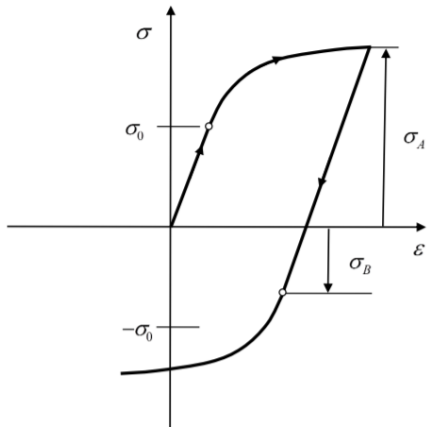

Figure 3.3: Illustration of the Bauschinger effect, and the stresses σ_A and σ_B (Hopperstad & Børvik 2017).

If there was no Bauschinger effect, σ_B would be equal in value but opposite sign of σ_A. This would lead to an r-ratio of 0. On the contrary, if the material started yielding at load reversal, σ_B would be almost equal to σ_A and the r-ratio would be approaching 1. This demonstrates that the r-ratio is increasing with an increasing Bauschinger effect and kinematic hardening. To compare the Bauschinger effect in the different DP steels, the r-ratio was calculated between the first load reversal and the subsequent yield for the load reversal tests displayed in Table 3.1.

3.3 The Idealized RVEs

The micromechanical FE modelling framework for plasticity and fracture of DP steels established in this study is based on the RVE method presented in Chapter 2. Different RVEs were tested, and the micromechanical FE modelling framework was consolidated by the modelling decisions that yielded the RVE that most accurately resembled the DP steel behaviour. The RVEs used and how they were created are presented in the following.

In this study, the martensitic islands were introduced with either cubical or spherical shape, but only one shape per RVE. The martensitic islands were mainly located in the centre of the RVEs, either as one cube or one sphere. In addition, RVEs with the martensite divided between the centre and the corners were also constructed. A 50% martensite distribution between the centre and corners was primarily used in this study, but the effect of using other distributions was also examined. Thus, four different RVEs were investigated during this study, and they are shown in Figure 3.4 and 3.5 for Docol 500DP. Pictures of the RVEs with the other steel qualities are presented in Appendix A.1 in Figure A.1.1 to A.1.8. It is emphasized that none of them resembled the actual microstructure of the DP steels. Thus, these RVEs were idealisations of the complex microstructure, and they were used to find trends by changing parameters rather than to reproduce the actual behaviour. Of that reason, the behaviour of these RVEs was also compared with an RVE with a more realistic distribution of the martensite phase. This RVE was not created by the authors of this study, and the comparison is assigned its own section to clearly separate the results obtained by using the different RVEs.

The idealized RVEs were modelled by using the finite element code Abaqus/Standard (ABAQUS 2019). Since the RVEs were symmetrical, only one eight of the RVEs

was modelled. The RVEs were created as a 3D deformable solid, and the elements used were the quadratic tetrahedron C3D10 elements. In general, the mesh size used was approximately ten elements per side length of the symmetrical model. This corresponded to roughly 7500 elements depending on the size and shape of the martensite islands. For the idealized RVEs, homogeneous boundary conditions were used, ensuring plane and perpendicular surfaces. The boundary conditions were implemented by constraining all nodes on a surface to have the same displacement in the direction of the surface normal as a master node on the same surface. The master nodes chosen were the node in origin and the one on the diagonally opposite side for the symmetrical and free surfaces, respectively. Furthermore, the node in the origin was fixed.

Figure 3.4: Docol 500DP: Illustration of the RVEs with cubical martensite. Martensite only in the centre to the left, while it is distributed both in the centre and the corners to the right. The blue and red parts represent the martensite and ferrite, respectively.

Figure 3.5: Docol 500DP: Illustration of the RVEs with spherical martensite. Martensite only in the centre to the left, while it is distributed both in the centre and the corners to the right. The blue and red parts represent the martensite and ferrite, respectively.

Load was either applied to the RVEs as prescribed displacement or as surface tractions. Prescribed displacement was used to obtain 1D stress states, while surface tractions were applied to obtain different plane stress states. The reaction forces used to find the average stresses in the RVE were extracted from the node in the origin, which was the fixed point in the model. The displacements used to find the average strains were extracted from the node on the diagonally opposite side

of origin. Because homogeneous boundary conditions were used, Equation (2.2) as Nygårds & Gudmundson (2002) presented was not needed to obtain the strains. Thus, $\sigma_e = \frac{F}{A_0}$, $\sigma_t = \frac{F}{A}$, $\varepsilon_e = \frac{L-L_0}{L_0}$, and $\varepsilon_l = \ln \frac{L}{L_0}$ were used to obtain engineering and true stresses and strains, respectively. A and A_0 are the current and initial area, L and L_0 are the current and initial side lengths, and F is the reaction force, respectively.

It was assumed that the behaviour of the DP steels could be derived from the behaviour of the two phases. An elasto-plastic material model was utilized for each phase, and it was assumed that the von Mises yield criterion with isotropic hardening and associated flow rule sufficed for both phases. The flow stress curves for the ferrite, σ^f, and martensite, σ^m, were in this thesis given and assumed representative, as they were calibrated by use of actual micromechanical parameters in Equation (2.1). The flow stress curves for the different steel qualities are presented in Figure 3.6. For each steel quality, the martensite phase flow curve is the higher curve, while the ferrite phase curve is the lower one. The flow stress curves were implemented in Abaqus by tabulating 200 equally spaced points from each curve.

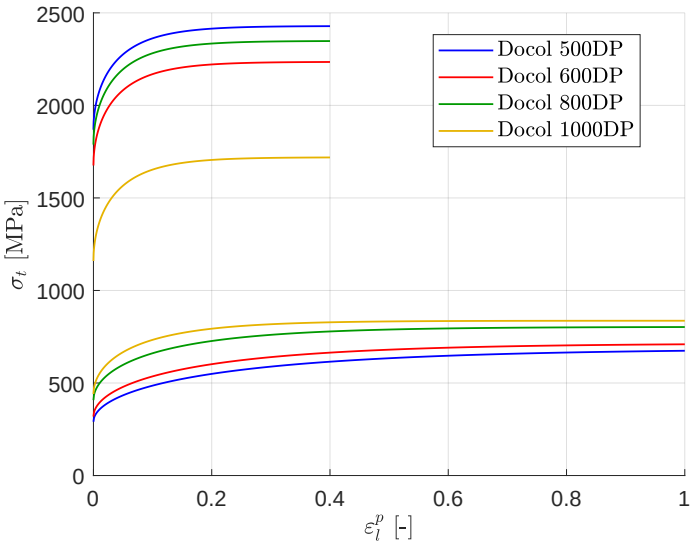

Figure 3.6: Flow stress curves for the different phases for the different steel qualities. The martensite phase for the different steel qualities are the upper curve, while ferrite is the lower.

The following sections present the use of the idealized RVEs. The preliminary studies are first presented, where the sensitivity and volume locking of the RVEs are considered. Then follows the presentation of the numerical study on yielding, work-hardening and ductile fracture of DP steels. Lastly, the calibration procedure used to propose material models for DP steels applicable to large-scale FE simulations is presented.

3.4 Preliminary Studies of the RVEs

3.4.1 Sensitivity Study

Before the idealized RVEs were used to produce results, the sensitivity of the models was investigated. Meaning, the type of element, the number of elements, and the length of the time increment used were varied. These sensitivity studies were conducted by use of the RVE with spherical martensite in the centre, and the load was uniaxial tension. Firstly, the mesh sensitivity was tested. The number of elements tested was 288, 1078, 2413, 5614, 7446 and 10203. Further, the time increment sensitivity in the simulations was checked. The time increment must be small enough to capture yield points with sufficient accuracy. The time period of the simulation was $t = 1\,\mathrm{s}$, and the time increments $\Delta t = 0.001\,\mathrm{s}$, $\Delta t = 0.005\,\mathrm{s}$, $\Delta t = 0.01\,\mathrm{s}$, and $\Delta t = 0.05\,\mathrm{s}$ were tested. Elements shaped as both tetrahedron and hexahedron were used to check element sensitivity, where C3D4, C3D10, C3D8R, C3D8, C3D20R, and C3D20 were tested and the number of elements was held constant.

3.4.2 Volumetric Locking

The elements chosen for the RVEs in this study were the quadratic tetrahedrons C3D10. Quadratic tetrahedrons are versatile in their ability to construct different geometries, which is a clear advantage when meshing the spherical sections in the RVEs. The elements are, however, prone to volumetric locking, and they were studied for this effect in addition to being compared to other similar finite elements. Volumetric locking could occur in fully integrated elements where the material is almost incompressible (Dassault Systèmes 2014). Materials like steel, which have a Poisson's ratio ν of 0.3, do not exhibit volumetric locking in the elastic domain, but it may occur in the plastic domain, where the slope of the stress-strain curve flattens. An increase in strain in the plastic domain leads to a small change in

stress, thus the increase of elastic strain is only a small part of the increase of total strain. With the plastic strains dominating, the total deformation is thus almost isochoric. When the behaviour approaches isochoric, the element may behave too stiffly if spurious strains develop in the integration points.

To evaluate whether volumetric locking was occurring, the pressure in the integration points was checked. If the pressure is varying heavily from element to element in a checkerboard pattern, volumetric locking arises. An element that can alleviate the volumetric locking is the hybrid formulation of C3D10, namely the C3D10H element. This element treats the pressure stress as an independent variable coupled to the displacement solution, and thus removes the singular behaviour that occurs when the bulk modulus diverges to infinity as a result of ν approaching 0.5 (Bell 2013). Volumetric locking was examined in a uniaxial tension simulation both with and without the implementation of the Gurson model. As the material softening due to void growth is governed by the pressure in the Gurson model, volumetric locking could have a greater impact on the results. In addition to checking whether a potential checkerboard pattern was alleviated by the hybrid elements, true stress-strain curves were made to see what effect the hybrid elements had on the overall performance of the RVEs.

3.5 Numerical Study of the DP Steels

A numerical study on yielding, work-hardening and ductile fracture of DP steels was performed. The following presents the content of the study. How it was done and which RVEs were used in the different parts are presented.

3.5.1 Yielding and Work-Hardening

To evaluate the RVEs capability of replicating the DP steels, a number of properties were studied. Uniaxial tension was first considered to see how well yielding and work-hardening of the four RVEs coincided with experimental data. The RVEs were exposed to uniaxial tension by using prescribed displacement. The energy distribution in the RVEs during this loading state was also considered, and strain energy and plastic dissipation in the two phases were therefore obtained. With the distribution of energy, it was possible to see how the engagement of the martensite phase was affected by different distributions and shapes of the martensite islands.

Acknowledging that the RVEs used in this study were simplified models, a more advanced model was used in order to compare the effectiveness of the simplified model. This advanced model was created by Saai (2019), and real microstructure of Docol 500DP from scanning electron microscopy was taken into account when distributing the martensite. In addition, periodic boundary conditions were imposed in this model. The model used a finer mesh with 62500 elements in order to recreate the real microstructure in a statistical sense, and the elements used were the linear hexahedron C3D8R. Figure 3.7 shows a picture of the RVE and the distribution of the martensite phase.

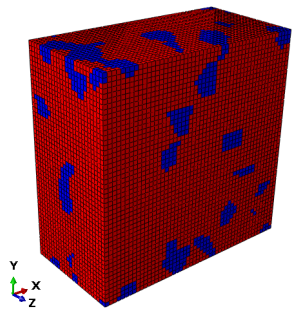

Figure 3.7: Docol 500DP: Illustration of the RVE with a more realistic distribution of the martensite phase. The blue and red parts represent the martensite and ferrite, respectively.

The investigation of the more advanced model was done in order to evaluate the RVEs used in this study. Both the computation time and the response in terms of stress-strain curves for different stress states were considered. In addition, homogeneous boundary conditions, where the edges were kept straight and perpendicular, were implemented in order to investigate the importance of the boundary conditions.

3.5.2 Iso-Curves

Then yielding in the RVEs in different stress states was evaluated. The yielding was found by loading the RVE to a point where the equivalent stress exceeded the uniaxial yield stress. This was done in a variety of plane stress states to obtain a yield surface, or more exactly, an iso-curve. An iso-curve resembles a yield surface. To produce an iso-curve, the plastic dissipation per volume, D_p, for the different stress states was considered. The plastic dissipation per volume was defined as

all plastic dissipation, $ALLPD$, in the model divided by the current RVE volume. In this project, uniaxial tension was used as a reference case to define the plastic dissipation per volume at 0.1%, 0.2% and 0.5% plastic strain. For each stress state, the instants when the plastic dissipation per volume was equal to the values from uniaxial tension were found. The points on the iso-curves were then obtained by extracting the corresponding stresses at these instants.

To get sufficiently fine iso-curves, 24 simulations were conducted for each RVE where the ratio between the average stresses in the two loading directions, σ_{11} and σ_{22}, was varied. These simulations constituted four simulations in pure tension and compression in the two main directions, seven simulations in the first and third quadrant with ratios between σ_{11} and σ_{22} of 1, 0.25, 0.5 and 0.75 and their inverses, and three simulations in the second and fourth quadrant with ratios of -0.5, -1 and -2. The loads applied in these simulations were surface tractions acting over whole sides with magnitudes that caused the equivalent stress to exceed the yield stress.

Iso-curves were provided for all four steel qualities when using the RVEs with martensite phase only located in the centre. Regarding the two RVEs with martensite phase both in the centre and the corners, it was assumed sufficient to only provide iso-curves for two different steel qualities for each RVE in order to notice the effect. Docol 500DP and 1000DP were chosen for the RVE with spherical martensite since the martensite volume fraction was the smallest and largest for these steel qualities, respectively. For the RVE with cubical martensite, having a martensite volume fraction greater than 0.25 led to overlapping of the martensite phases. Therefore, iso-curves for Docol 800DP instead of Docol 1000DP were created when using the RVE with cubical martensite.

3.5.3 Kinematic Hardening

The third property evaluated was the amount of kinematic hardening in the RVEs. The RVEs were exposed to the same loading cycles as the specimens in the laboratory tests. Because it was the first yield after load reversal that was of interest, it was enough to simulate only one load cycle. In the load reversal simulations, the RVEs were loaded by prescribed displacement to be able to get the same strains as in the experiments. In terms of the r-ratio, the post-processing of the simulations

was similar to that of the experiments, as explained previously.

Further, it was investigated numerically how the martensite volume fraction affected the Bauschinger effect. Simulations of the RVEs with the martensite concentrated in the centre with material data from Docol 500DP and varying martensite volume fraction were conducted. The volume fraction was varied between 0-100% to give information on how the Bauschinger effect varied over the whole domain. In the RVE with spherical martensite in the centre, the volume fraction can only reach 52% before the diameter of the sphere exceeds the length of the unit cell. Therefore, the martensite and ferrite phases switched sections at 50% volume fraction, so that for a volume fraction over 50% it was effectively the ferrite that was in the shape of a sphere. It was not evaluated how the Bauschinger effect varied with martensite volume fraction for the RVEs with martensite both in the centre and the corners. This was because of the restrictions in the geometry. For the RVE with cubical martensite, the martensite volume fraction cannot exceed 25%, but from 75% it can be modelled if the two phases changes places. The same holds for the RVEs with spheres. Here the geometry has a limit at 68%. By altering the RVEs in this manner, they are not comparable to the ones that have the phases in their respective places.

3.5.4 Fracture

The numerical study on ductile fracture of DP steels was limited to only consider the idealized RVE with cubical martensite in the centre and uniaxial tension. The ductile fracture was investigated by introducing the Gurson model described in Chapter 2. The objective of the fracture study was to investigate whether or not the reported void nucleation, growth and coalescence in DP steels could be captured by the idealized RVE. This was done by first considering the influence of the parameters included into the Gurson model, before the obtained fracture mechanisms in the idealized RVE were investigated.

To investigate fracture in the RVE, the previously described Abaqus model (Section 3.3) was adjusted through the following steps. To represent the evolution of voids, the Gurson model was used to model the ferrite behaviour. The values for q_1, q_2 and q_3 in Equation (2.3) were set to 1.5, 1.0 and 2.25, respectively. These are standard values for metals in most cases, and were assumed sufficient. Thus, they were kept

constant throughout this study. It was chosen to use Abaqus/Explicit because it allowed for element erosion, and the elements used were of type C3D10M. Element erosion was implemented as a porous failure criterion in the ferrite material model, in which the critical void volume fraction, f_c, and void volume fraction at total failure, f_F, were the parameters. These parameters were kept constant in order to reduce the number of adjustable parameters. The fixed values were 0.02 and 0.2 for f_c and f_F, respectively. Note that the void nucleation feature was not included in this fracture study. The time period chosen was $t = 0.001\,\mathrm{s}$ and prescribed velocity in one direction was applied to establish uniaxial tension. The magnitude of the velocity was increased gradually from 0 to 1000 mm/s in the first 10% of the simulation. Since time scaling was utilised, it was checked that the kinetic energy was less than 1% of the internal energy in the energy balance of the simulation.

Thus, it was chosen to only vary the initial void volume fraction, f_0, parameter in this fracture study. Values in the range 10^{-2} to 10^{-4} of the f_0-parameter were tested. The engineering stress-strain curves were compared with those from the uniaxial tension experiments. Topics of discussion are the influence of the Gurson model parameters and the obtained fracture mechanisms.

3.6 Homogenization

The calibration procedure used to propose material models for DP steels is presented in the following. The objective was to obtain material models based on the the central hole experiments and the idealized RVE with cubical martensite in the centre. This was done by homogenizing the behaviour of the RVE. Meaning, the yielding and work-hardening obtained in the idealized RVE were reproduced by one single homogeneous element. The central hole experiments were used as a reference case in order to determine when fracture should initiate. The calibration procedure is called the micro-macro approach herein and it consists of five steps, which are presented in the following. Figure 3.8 gives an overview of the approach and examples of how the obtained parameters are used further in the approach.

The first step of the approach was to calibrate the plasticity parameters of the material model for each steel quality. The calibration was based on the idealized RVE with cubical martensite in the centre exposed to uniaxial tension. The material model was fitted the true stress vs. plastic strain curve of the RVE (without

using Gurson model) up to a plastic strain of unity for all steel qualities. The von Mises equivalent stress was defined by an extended Voce hardening law in Equation (3.5) where p is the equivalent plastic strain, σ_0 is the yield stress, and (Q_{Ri},C_{Ri}) are the hardening parameters. In this case, seven parameters were calibrated when using three terms. The calibration was done using the Solver in Excel.

$$\sigma_{eq} = \sigma_0 + \sum_{i=1}^{n} Q_{Ri}(1 - \mathrm{e}^{-C_{Ri}p}). \tag{3.5}$$

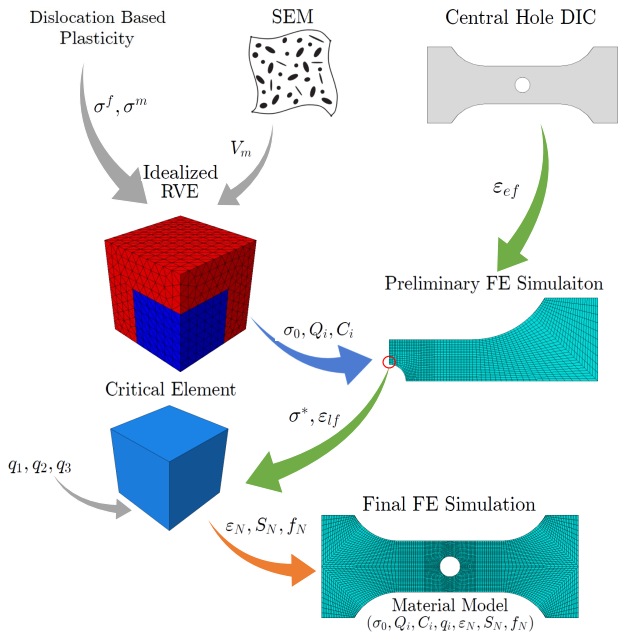

Figure 3.8: An overview of the micro-macro approach with examples of how the obtained parameters are used further in the approach.

The next step in the approach was to conduct central hole tests both experimentally and numerically for all the steel qualities. The central hole tests were used due to more stable stress triaxiality and less scatter in the fracture strain for repeated tests compared to the uniaxial tension tests. As previously mentioned, the central hole tests were conducted in advance of this study. Numerically, one eight of the central hole specimen was modelled in Abacus/Explicit. It was modelled as a 3D

deformable solid with C3D8R elements. The material model was elasto-plastic with the calibrated three-termed Voce law from the last step, and prescribed velocity was applied as load. Figure 3.9 shows the symmetric numerical model used.

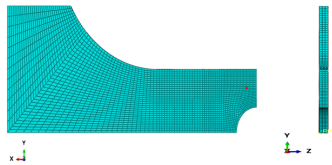

Figure 3.9: The symmetric numerical model used to simulate the central hole test. The red dot marks the virtual extensometer node.

The aim of this step was to locate the critical element in the numerical model and to obtain both the true stress-strain history and the stress triaxiality in that critical element all the way to fracture. First, the engineering strain where the specimen fractured experimentally, ε_{ef}, was found. This engineering strain was reproduced in the numerical model, and the corresponding increment was defined as the increment when final fracture should occur. It is emphasized that the virtual extensometer lengths used to calculate the engineering strain at failure both experimentally and numerically were of equal length. The local extensometer with length 2 mm was used in this case (the red dot in Figure 3.9). Then, the critical element in the numerical model was defined as the element with the highest equivalent plastic strain at final fracture. The true stress-strain curve, strain at final fracture, ε_{lf}, and stress triaxiality, σ^*, for this element were extracted. The true stress-strain curve was obtained by using the element stress and strain components in the loading direction (x-direction in Figure 3.9).

The approach continued by considering the RVE, where the Gurson model was implemented in the ferrite phase and the effect of void evolution was investigated either by introducing initial void volume fraction or void nucleation. The applied loading condition corresponded to the stress triaxiality found in the critical element. It was assumed that an average stress triaxiality over strain, $\overline{\sigma}^*$, was sufficient. The true stress-strain curve from the RVE was compared to the one from the critical element. In this step, the main focus was to initiate fracture in the RVE at the fracture strain in the critical element. The initial void volume fraction, f_0, parameter was varied in order to fit the fracture strain of the RVE to the fracture strain in the critical element. Regarding void nucleation, only the expected plastic

strain at nucleation, ε_N, was varied, while the associated standard deviation, S_N, and void volume nucleation fraction, f_N, were fixed with the values 0.05 and 0.01, respectively. In order to apply the desired stress triaxiality and to pass limit points in the stress-strain curve, surface tractions and the Riks-algorithm were used in the numerical model of the RVE. Since the Riks-algorithm was available only in Abaqus/Standard, the porous failure criterion was not applicable.

The next step in the approach was to include the Gurson model into the homogeneous material model. This was done by considering fracture in the single homogeneous C3D8R element shown in Figure 3.10. For the single homogeneous element, the average triaxiality from the critical element was applied, as done previously for the RVE. The aim was to obtain a reduction in the true stress-strain curve around the fracture strain in the critical element. The initial void volume fraction and void nucleation features were included separately into the Gurson model. The Riks algorithm was utilized, and thus a porous failure criterion was not used.

As the final step, numerical simulations of the central hole tests were carried out. In contrast to the numerical model described in the second step, only symmetry in the thickness direction was utilized and the material model calibrated during this approach was used. Figure 3.11 shows the numerical model where the nodes used as virtual extensometer are marked with red dots. The accuracy of the engineering stress-strain curve from this simulation should to a larger extent resemble the experimental data.

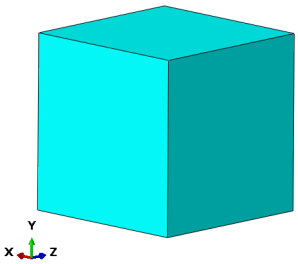

Figure 3.10: The single homogeneous element used to simulate the critical element in the central hole test.

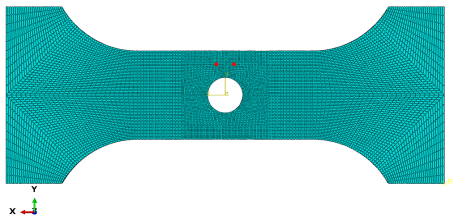

Figure 3.11: The numerical model used to simulate the central hole test in the final step, where the red dots mark the virtual extensometer nodes.

4 Experiments

The results and discussion from the cyclic load laboratory tests are presented in the following. An evaluation of the anti-buckling device is first presented before the findings on how the martensite volume fraction influences the Bauschinger effect in DP steels are addressed.

The anti-buckling device has not been used before, and it should therefore be checked that no additional effects, other than buckling resistance, was provided. Figure 4.1 to 4.4 show the data obtained from the cyclic load experiments as true stress-strain curves for the different steel qualities and the different loading sequences. Every figure contains three load reversal tests where the loading started in compression and one load reversal test that started in tension. Both Figure 4.2 and 4.4 contain one curve where the specimen, without the anti-buckling device, was stretched in tension until failure.

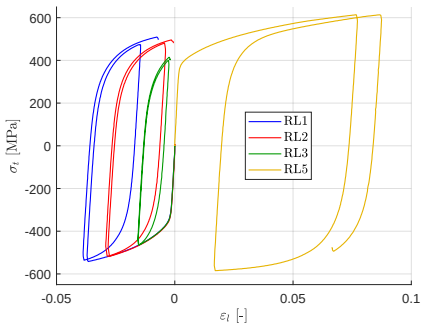

Figure 4.1: Docol 500DP: True stress-strain curves for the different loading sequences.

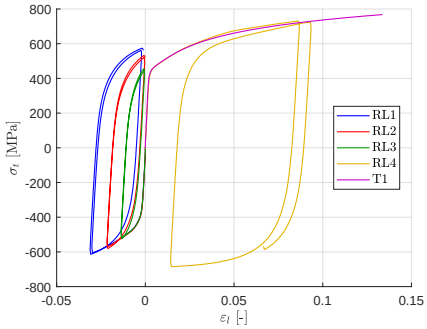

Figure 4.2: Docol 600DP: True stress-strain curves for the different loading sequences.

In addition to the experimental data obtained in this study, the true stress vs. plastic strain curves from the uniaxial tension tests conducted with other specimens were provided by the supervisors of this study. In Figure 4.5, the results obtained by using the two different specimen geometries are plotted together. The continuous lines represent the curves from this study, where the curves T1 and RL5

up to the first load reversal were used. The dashed lines are the curves obtained from the uniaxial tension experiments conducted prior to this study. In general, the curves obtained in this study are shifted upwards.

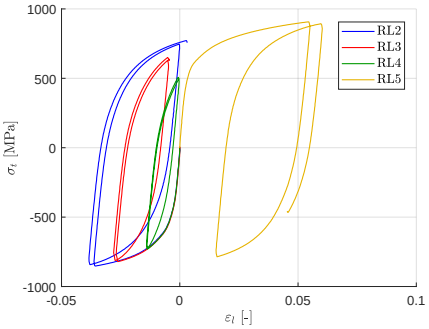

Figure 4.3: Docol 800DP: True stress-strain curves for the different loading sequences.

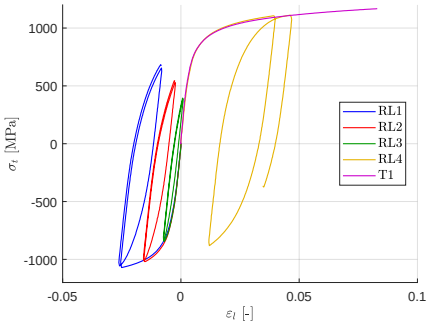

Figure 4.4: Docol 1000DP: True stress-strain curves for the different loading sequences.

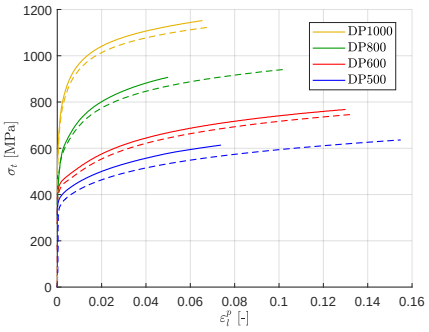

Figure 4.5: Comparison of experimental results obtained by use of different specimens. The continuous lines and the dashed lines represent the results from the cyclic load tests and uniaxial tension tests, respectively.

By use of linear regression in MatLab it was found that the slope of the curves in the elastic domain of Figure 4.1 to 4.4, both in the beginning and past the load reversal points, was in the range of 170 GPa-230 GPa. The estimated values were in the order of magnitude of the theoretical value of Young's modulus for steel, 210 GPa. The scatter in the estimates appeared because of the approach used. Neither the laboratory tests nor the DIC measurements were appropriate to estimate the Young's modulus (Chen et al. 2016). Thus, the test results showed the

stiffness of the system. Furthermore, the tension-compression load reversal tests up to load reversal almost coincided with the pure tension tests where the anti-buckling device was not attached. These findings indicate that the anti-buckling device did not affect the stiffness of the system significantly. Based on this, the cyclic load laboratory tests have provided the desired results, and the trends regarding kinematic hardening found from the experimental results should resemble the actual behaviour of the DP steels.

Having said that, it should be kept in mind that the two curves in tension in Figure 4.2 and 4.4 did not coincide perfectly. The design of the anti-buckling device could therefore be improved further with respect to performance. Furthermore, Figure 4.5 shows that the results from the cyclic load experiments did not coincide with the previously conducted uniaxial tension experiments. The increased strength experienced in this study was caused by either the specimen geometry or the use of the high pressure grip. Commonly for standard uniaxial tensile specimens, the length of the gauge area is several times the width. For instance, the length was around five times the width for the specimens used in the uniaxial tension tests conducted prior to this study. In this study, the length was only 1.4 times the width (seen in Figure 3.1). It is plausible that the strains in the gauge length were non-uniform, and that the geometry of the specimen was not optimal for uniaxial tension and compression. The consequence of the increased strength was not considered as critical, but it should be kept in mind when comparing the RVEs with experimental data. Thus, the cyclic load laboratory tests were only used to consider the kinematic hardening in DP steels in this study.

Figure 4.6 shows the r-ratio, which represents the Bauschinger effect (Equation (3.4)) plotted together with the corresponding equivalent plastic strain before load reversal for the different steel qualities. The star points with lines in-between depict the r-ratio obtained from the compression-tension load reversal tests, while the single star points depict the tests that started in tension.

The main tendency in Figure 4.6 is evident; the r-ratio increases with the steel quality. Furthermore, the increase in r-ratio from Docol 500DP to 600DP and from Docol 800DP to 1000DP was smaller than the increase between Docol 600DP to 800DP. It was noticed that the Bauschinger effect stagnated or even reached a limit point when increasing the equivalent plastic strain. On the other hand,

the largest Bauschinger effect was obtained in the tests that started in tension where the specimens were stretched the most. Whether this indicates that the Bauschinger effect was more dominant for tests that started in tension, or that the Bauschinger effect increases with the equivalent plastic strain, was not clear as only a few data points constituted the results. A possible explanation for the trend may be that, during tension the specimen became more slender, which relaxed the springs and decreased the overall stiffness of the system before load reversal, and that this caused an earlier yield after load reversal.

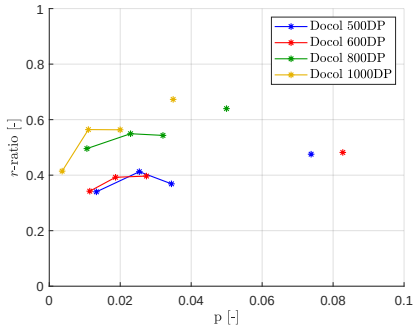

Figure 4.6: The Bauschinger effect shown in terms of the r-ratio from the experimental data.

As mentioned in Chapter 2, Erdogan & Priestner (2002) stated that the Bauschinger effect was higher for a DP steel with 25% martensite volume fraction than with 18%. Further, it was stated that the Bauschinger effect increased when the prestrain increased from 0.4 to 2.2%, and that the sign of the prestrain did not influence the Bauschinger effect. Thus, the trend observed in Figure 4.6 regarding the Bauschinger effect increasing with the martensite volume fraction appears reasonable. Furthermore, whether tension-compression tests give rise to larger Bauschinger effect than compression-tension tests seems unlikely, since it has been stated that the sign of prestrain does not affect the Bauschinger effect. It has also been mentioned in the literature that the Bauschinger effect tends to saturate when the prestrain increases (Milligan et al. 1966), which may explain why the r-ratio tends to stagnate for each steel quality when the plastic strain before load reversal increases.

The behaviour of the different DP steels depends on several parameters, including the martensite volume fraction, carbon content, grain size and shape and morphol-

ogy between ferrite and martensite (Anbarlooie et al. 2018). It is probable that the trends observed regarding the Bauschinger effect were not caused by one single parameter, but rather the result of changing several of them. As explained in Chapter 2, Kocks & Mecking (2003) stated that the Masing effect in polycrystals and transient effects within single crystals contribute to the Bauschinger effect, which means that the Bauschinger effect is dependent on the ferrite morphology. In this study, special attention was given only to the martensite and its volume fraction.

The martensite volume fractions were 0.13, 0.18, 0.25 and 0.50 for Docol 500DP, 600DP, 800DP and 1000DP, respectively. In the literature, it is frequently mentioned that in DP steels, the ferrite phase is soft providing high ductility of the material, while the martensite phase is strong contributing with strength. When the DP steel starts to deform plastically, the ferrite deforms plastically, while the martensite remains elastic due to its higher yield stress. This means that the elastic strains in the martensite are larger than in the ferrite. Of this reason, the martensite would load the ferrite in the opposite direction during unloading of the DP steel, which contributes to an earlier yield in the case of load reversal. Thus, the Bauschinger effect should be larger for materials with higher martensite content, at least up to a certain limit.

Based on Figure 4.6, this effect was small for the change between Docol 500DP and 600DP, and Docol 800DP and 1000DP. In the latter case, it is plausible that the effect decreased (or even vanished) because the microstructure became dominated by martensite. Thus, the interaction between the ferrite and martensite was of less importance, since also the martensite deforms plastically during loading. A reasonable statement would be that the r-ratio eventually reaches a maximum by further increasing the martensite volume fraction, before it starts decaying. It is emphasized that this was not observable in the experimental work, but it has been proven to be true for the RVEs as it was investigated in the numerical study. In contrast, if the martensite volume fraction decreases below a certain level, the change of the Bauschinger effect would also vanish, since the microstructure becomes dominated by ferrite. The mechanism described above becomes less significant, such that the Bauschinger effect obtained is mainly caused by the ferrite phase alone and its grain structure. In summary, Figure 4.6 shows that the Bauschinger effect is dependent on the steel quality. Docol 500DP and Docol 1000DP experienced

the least and the most Bauschinger effect, respectively, which indicates that the martensite volume fraction affects the Bauschinger effect in DP steels.

The uncertainty in the number of data points is emphasized, as the trends were based on only four data points for each steel quality. If one or several points are slightly changed, the trends may be different. In order to obtain more reliable trends, a greater number of tests should be conducted. Both a wider range of equivalent plastic strain and several attempts of each test, in order to discover a possible scatter in the results, should be considered.

5 Preliminary Studies of the RVEs

The RVEs have been tested to see what behaviour they exhibit. Before comparing the results from the RVEs with the experimental data, the sensitivity study and the section about volumetric locking are presented. The sensitivity study was conducted to determine the element type, the number of elements and the time increment necessary in the simulations.

5.1 Sensitivity Study

For the mesh and time increment sensitivity studies, the RVE with spherical martensite in the centre for Docol 800DP was used. Figure 5.1 shows the true stress-strain curves obtained by varying the number of C3D10 elements used. The response converged when the number of elements increased, and the change was small beyond 7500 elements. In Figure 5.2 it can be observed that yield was reproduced accurately for every time increment chosen, and a small improvement was obtained by using $\Delta t = 0.01\,\mathrm{s}$ compared with $\Delta t = 0.05\,\mathrm{s}$. The effect of varying element type is shown in Figure 5.3. Here, the RVE with spherical martensite in the centre for Docol 500DP was used. The linear tetrahedron element, C3D4, was overly stiff, while only small differences in response were observed between the quadratic tetrahedron C3D10 element and the hexahedron shaped elements, C3D8R, C3D8, C3D20R and C3D20.

The sensitivity study shows the importance of the choices made when creating the RVEs. The consequence of selecting either an insufficient element, too coarse a mesh, or too large a time increment is less accurate results. Based on the sensitivity study, a mesh consisting of 7500 elements or more, a time increment equal or smaller than $\Delta t = 0.01$s, and the quadratic tetrahedron element C3D10 or the hexahedron elements need to be used in order to obtain the accurate solutions. This is in accordance with the Abacus Analysis User's Guide section 28.1.1, which advises against using first-order tetrahedrons (C3D4) as they are overly stiff and has very slow convergence rates (ABAQUS 2019). On the other hand, it is impractical to choose more elements, or a smaller time increment than necessary since it

increases the cost of the simulation without increasing the accuracy significantly.

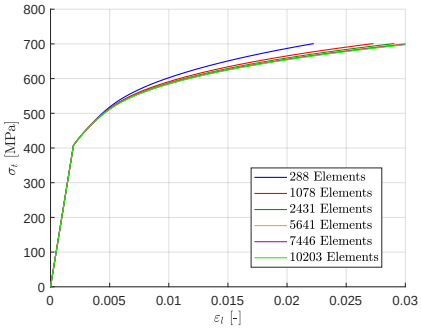

Figure 5.1: Docol 800DP: True stress-strain curves showing mesh sensitivity obtained with the RVE with spherical centre in uniaxial tension.

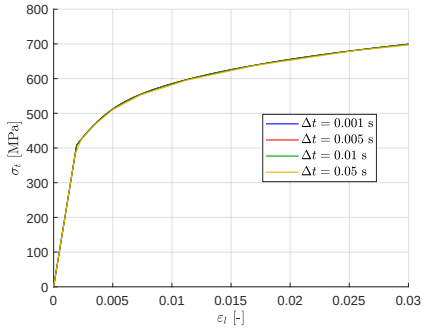

Figure 5.2: Docol 800DP: True stress-strain curves showing time increment sensitivity obtained with the RVE with spherical centre in uniaxial tension.

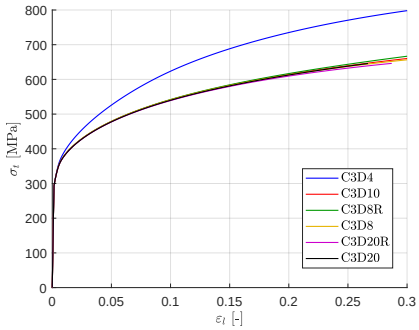

Figure 5.3: Docol 500DP: True stress-strain curves showing element sensitivity obtained with the RVE with spherical martensite in the centre in uniaxial tension.

Figure 5.3 indicates that several elements are reasonable for this analysis. The tetrahedron element C3D10 was chosen based on its versatility and simplicity when it comes to meshing the spheres. Regarding the mesh and time increment, approximately 7500 elements and $\Delta t = 0.01\,\mathrm{s}$ were used thenceforth, but the time increment was changed where necessary in order to capture yield accurately depending on the length of the simulation. Note however, that different RVEs were used in the sensitivity study. Additionally, other RVEs are used more extensively later in the study, so the choice of RVEs for the sensitivity was not optimal and the results could have differed somewhat.

5.2 Volumetric Locking

The results and discussion from the volume locking investigation are presented in the following. In addition to investigating the occurrence of volume locking, the hybrid formulation of the used element, C3D10H, is considered. In this study, RVEs both with and without the Gurson model in the ferrite material model are used. Thus, volume locking is considered in both cases. It was assumed sufficient to only consider uniaxial tension and the RVE with cubical martensite in the centre for Docol 600DP.

The case without the Gurson model implemented was first considered. As explained in Section 3.4.2, the field output for pressure of the RVE was plotted and investigated for checkerboard patterns. Figure 5.4 shows only the ferrite phase of the RVE when C3D10 was used, viewing from the centre and outwards. It is showing the ferrite-martensite interface, and the values plotted represent the pressure. Here, a checkerboard pattern of the pressure with a great variance in magnitude can be seen. This is signalling the occurrence of volumetric locking. An equivalent figure with the same colour spectrum was obtained through the use of the hybrid elements C3D10H, and is shown in Figure 5.5. Here, there is no marked variation in pressure between neighbouring elements, which makes it obvious that there are no checkerboard patterns. In the non-critical areas of the RVE, the pressure is the same for both the hybrid and non-hybrid elements.

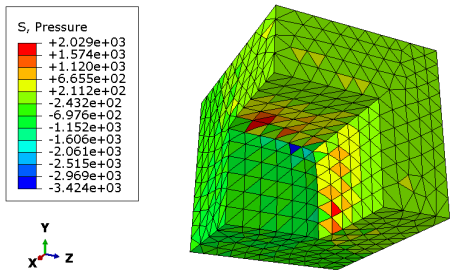

Figure 5.4: Docol 600DP: Pressure in the RVE with C3D10 elements. Only the ferrite phase is visible.

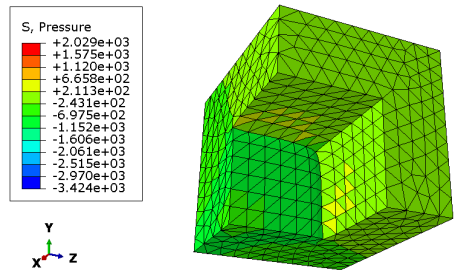

Figure 5.5: Docol 600DP: Pressure in the RVE with hybrid elements C3D10H. Only the ferrite phase is visible.

The corresponding true stress-strain curves are shown in Figure 5.6, where it can be seen that the RVE with hybrid elements display a softer behaviour than the RVE with C3D10 elements. The two curves are coinciding until yielding, which is

where the ancillary features in the hybrid element commences. The relative difference between the curves from the two element types is 1.4% at 0.4 true strain.

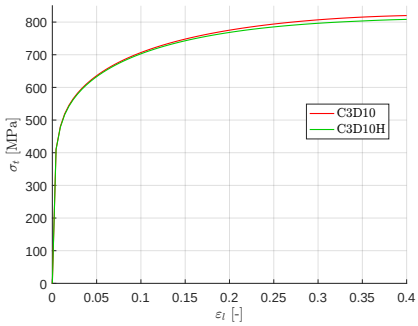

Figure 5.6: Docol 600DP: True stress-strain curves from the RVE with cubical martensite in the centre. Comparison between C3D10 and C3D10H elements.

By using the C3D10 elements, volumetric locking was occurring to a certain extent. This was evident from the inspection of the RVE, as a checkerboard pattern was clearly present in Figure 5.4. This was remedied by the use of hybrid elements, and the RVE without volumetric locking can be seen in Figure 5.5. However, when looking at Figure 5.6, the influence of the volumetric locking on the true stress-strain curve for the RVE was small and almost negligible. At most, the difference between the C3D10 and C3D10H elements was 11 MPa at a true strain of 0.4, which corresponds to a difference of 1.4%. Additionally, when taking into account the added expenses of the hybrid elements because of their extra internal variables, the hybrid elements were not desirable in the case without the Gurson model. An increase in the simulation time of 500% was frequently experienced when using hybrid elements. The hybrid elements were successful in eliminating the volumetric locking, but in this case, the amount of volumetric locking was low and using hybrid elements was therefore deemed superfluous.

It may be more important to assess the volumetric locking in the RVE when the Gurson model is implemented. This is because the plasticity and void growth are affected by the hydrostatic pressure in the Gurson model. Both the initial void volume fraction and void nucleation features were used in this study. Thus, volumetric locking was considered for both features. It was assumed sufficient to conduct only one test of each feature. An initial void volume fraction of $f_0 = 10^{-4}$ and void nucleation with $\varepsilon_N = 1$, $S_N = 0.05$ and $f_N = 0.01$ was imposed in the same RVE

as above.

The effect of the volumetric locking can be seen in the true stress-strain curves in Figure 5.7 and 5.8 when using the initial void volume fraction and void nucleation features, respectively. In contrast to the first case, the material softening occurred earlier and was more extensive in the RVE with hybrid elements than for the non-hybrid elements. Furthermore, the simulations stopped early. The reason for that was unclear since the void volume fraction was only approximately 0.02 when the simulations stopped. The material softening when using the void nucleation feature was delayed compared to the initial void volume fraction feature since the voids were not present initially.

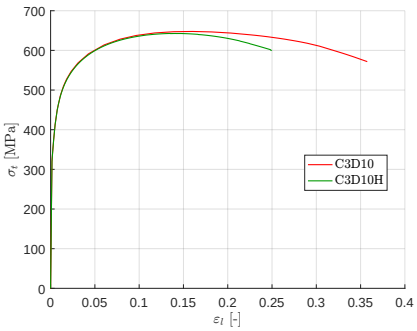

Figure 5.7: Docol 600DP: True stress-strain curves for the RVE with C3D10 and C3D10H elements with initial voids.

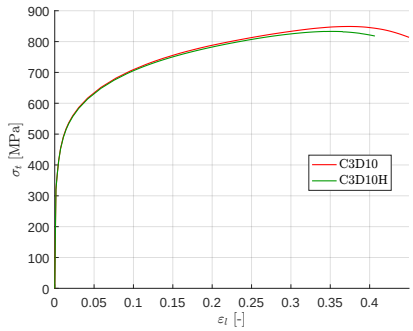

Figure 5.8: Docol 600DP: True stress-strain curves for the RVE with C3D10 and C3D10H elements with void nucleation.

These findings show that it was important to consider volume locking when the Gurson model was included. However, the C3D10H elements were not available in Abaqus/Explicit. The Abaqus Analysis User's Guide section 28.1.1 recommended to use the modified formulation of the elements instead, since they exhibit minimal volumetric locking. Thus, it was chosen to use the C3D10M elements in the fracture study (ABAQUS 2019). In Chapter 7, the Gurson model was used together with Abaqus/Standard, and an attempt at using the C3D10H element was done. However, the hybrid elements were more computationally demanding and were in some cases less robust and caused simulations not to finish as mentioned above. Thus, the normal C3D10 elements was used because the simulations with the hybrid elements tended to stop prematurely.

6 Numerical Study of the DP Steels

This chapter presents the results and discussion from the numerical study. Section 6.1 covers yielding and work-hardening of the four different RVEs in uniaxial tension. In addition, the comparison of the idealized RVEs with an RVE based on a realistic martensite distribution follows at the end of this section. Further, Section 6.2 presents the yielding in different stress states, while Section 6.3 considers the kinematic hardening and the Bauschinger effect as a function of martensite volume fraction. Lastly, ductile fracture is considered in Section 6.4.

6.1 Yielding and Work-Hardening

The behaviour of the RVEs in terms of yielding and work-hardening is presented in the following. The RVEs are compared with the experimental data from the uniaxial tension tests up to necking. An in-depth analysis of uniaxial tension provides knowledge of how this simplistic modelling of the DP steels was able to reproduce physical properties. This simplicity, as explained in Section 3.3, stems from the simple shapes of the martensitic phase, namely cubical and spherical. When convenient, the data points are plotted with square and circle shapes when the martensite phase is cubical or spherical, respectively, in order to easily separate the results from the RVEs. Finally, a more realistic RVE is introduced and compared with the idealized RVEs.

In Figure 6.1 to 6.4, the experimental data from the uniaxial tension tests and corresponding results obtained from the RVEs with martensite only in the centre are compared. The dashed blue lines are the experimental results up to necking. The red and green lines are the RVEs with cubical and spherical martensite in the centre, respectively. The results obtained from the RVE with cubical martensite in the centre almost coincided with the experimental data. In general, both the yielding and the work-hardening were captured to a great extent. Additionally, the continuous yielding of the DP steels was captured in this RVE. The RVE with spherical martensite in the centre exhibited a softer behaviour, but the work-hardening rate in the plastic domain resembled both the experiments and the RVE

with cubical martensite.

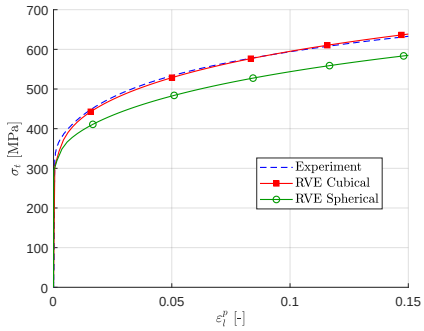

Figure 6.1: Docol 500DP: True stress vs. plastic strain curves obtained from the RVEs with cubical and spherical martensite phase in the centre and the experimental data in uniaxial tension.

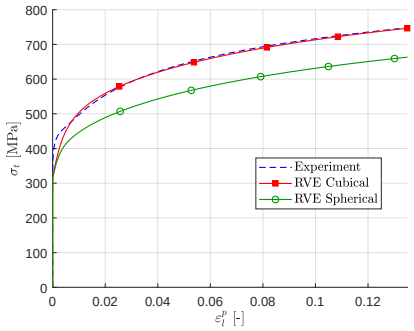

Figure 6.2: Docol 600DP: True stress vs. plastic strain curves obtained from the RVEs with cubical and spherical martensite phase in the centre and the experimental data in uniaxial tension.

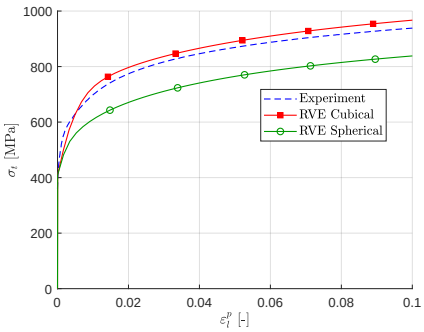

Figure 6.3: Docol 800DP: True stress vs. plastic strain curves obtained from the RVEs with cubical and spherical martensite phase in the centre and the experimental data in uniaxial tension.

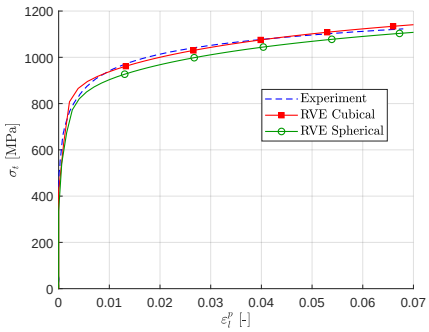

Figure 6.4: Docol 1000DP: True stress vs. plastic strain curves obtained from the RVEs with cubical and spherical martensite phase in the centre and the experimental data in uniaxial tension.

It can be seen from the figures that the yield stresses were approximately equal for the experiments and the RVEs for all steel qualities. The largest discrepancies occurred in the elasto-plastic transition phase. Initially, the experiments had the steepest work-hardening. This may be attributed by the geometrically necessary dislocations in the DP steels, which control the continuous yielding and vary with the microstructure. These were not included explicitly into the RVEs, and thus the

yielding did not coincide perfectly. However, the simplistic RVE exhibited the desired yielding mechanism, as opposed to the yield point elongation of conventional steels. The work-hardening rate for the RVE with cubical martensite compensated in average this difference, while the RVE with spherical martensite did not, which led to the soft behaviour. Considering the plastic domain, the slopes of the curves were nearly equal, which implies approximately equal work-hardening rates for the experiments and the RVEs. These findings indicated that the behaviour of the RVE, when it came to yielding and strength, was more dependent on the shape of the martensite phase, than the work-hardening rate in the plastic domain where only small differences were observable. Similar trends were found by Nygårds & Gudmundson (2002), who stated that the complex microstructure of DP steels was important to accurately predict the behaviour around the yield point.

The effect of distributing the martensite phase evenly both in the centre and the corners in terms of true stress vs. plastic strain curves is shown in Figure 6.5 and 6.6 for the RVEs with cubical and spherical martensite, respectively. The figures show the results obtained by use of Docol 600DP, but the trends were similar for the other steel qualities, shown in Appendix A.2. It was noticed that a softer response was obtained by distributing the martensite phase both in the centre and the corners compared to only in the centre.

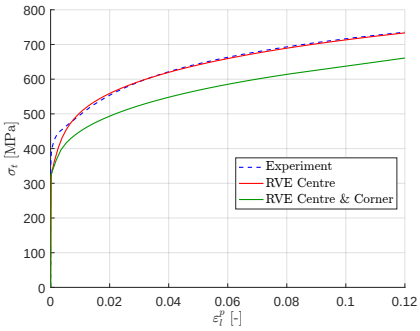

Figure 6.5: Docol 600DP: True stress vs. plastic strain curves obtained from experiments and both RVEs with cubical shape of martensite in uniaxial tension.

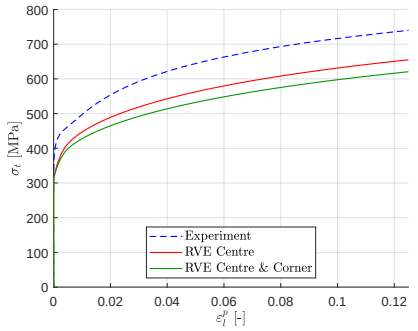

Figure 6.6: Docol 600DP: True stress vs. plastic strain curves obtained from experiment and both RVEs with spherical shape of martensite in uniaxial tension.

Further, a quick investigation was conducted where the martensite phase was distributed unevenly between the centre and the corners by using the RVE with cubical

martensite. Figure 6.7 shows how the true stress vs. plastic strain curve was affected by the distribution of the martensite. The softest behaviour was obtained when the martensite was divided evenly between the centre and the corners. The behaviour of having all the martensite in the corners was exactly the same as having all in the centre. Further, the behaviour was the same when the martensite was distributed with a 10% in the centre and 90% in the corners as when it was reversed.

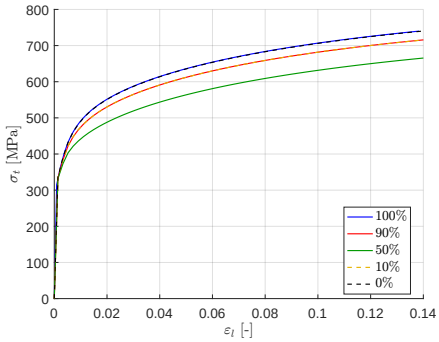

Figure 6.7: Docol 600DP: True stress vs. plastic strain curves obtained with the RVE with cubical martensite when varying the distribution of martensite between the centre and the corners. The percentage is the fraction of martensite that was located in the centre.

When considering the RVEs with martensite in the centre, the only difference between the RVEs was the geometry of the martensite, which implies that the geometry of the RVEs was the reason for the differences in strength. To understand the reasons to why this is, the spatial distribution of the von Mises equivalent stresses and equivalent plastic strains may be helpful to examine. Figure 6.8 and 6.9 show contour plots of the equivalent von Mises stresses in the ferrite at the same instant for the two RVEs with Docol 500DP. It is evident that the largest stresses at the loaded surface were concentrated in the middle of the surface (lower right corner).

Further, it is observed that the stress was more concentrated in the RVE with cubical martensite, while the stresses were in average higher in the RVE with spherical martensite. Higher stresses in the ferrite indicate larger strains. This means that the ferrite was more deformed in the RVE with spherical martensite in the centre compared with cubical martensite when they were exposed to the same loading. Since the ferrite contributed more than the martensite to the total

deformation, it becomes clear that total deformation of the RVE with spherical martensite must be the largest. This means that the force-displacement curves (and the stress-strain curves) are lower for the RVE with spherical martensite in the centre, which coincides with the results obtained earlier.

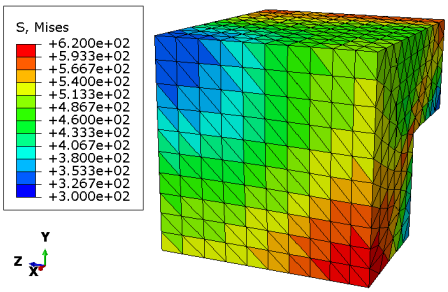

Figure 6.8: Equivalent von Mises stress in the ferrite part of the RVE with cubical martensite in the centre.

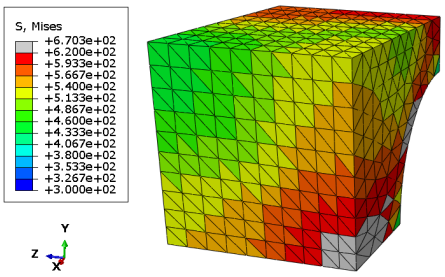

Figure 6.9: Equivalent von Mises stress in the ferrite part of the RVE with spherical martensite in the centre.

The different response obtained by changing the shape of the martensite could also be explained by considering the martensite, and how much of it is engaged plastically during deformation. Figure 6.10 and 6.11 show contour plots of the equivalent plastic strain in the martensite when it is shaped as a cube and sphere, respectively. As for the contour plot of the ferrite above, the plots are from the same instant in uniaxial tension and the material is Docol 500DP. Evidently, the plots show that plastic strain only occurred in the cubical martensite, while the spherical martensite remained elastic. Thus, the cubical martensite contributed more compared to the spherical, and caused an increase of the strength.

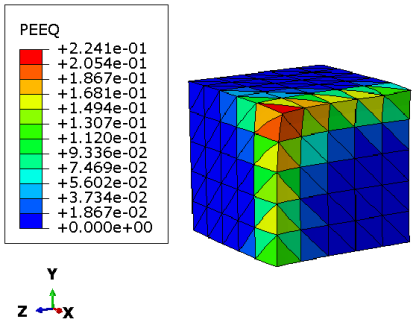

Figure 6.10: Equivalent plastic strain in the martensite cube in the centre.

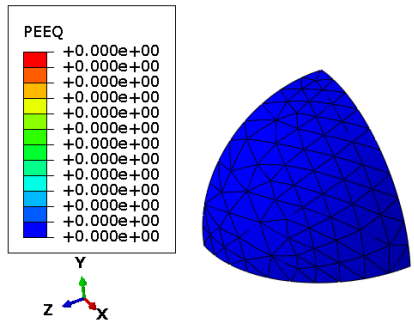

Figure 6.11: Equivalent plastic strain in the martensite sphere in the centre.

This reasoning is further supported by the distribution of energy in the models, as shown in Figure 6.12 and 6.15. These figures show the sum of the element elastic strain energy (ELSE) and sum of the element plastic dissipation (ELPD) in the different phases in the RVEs for Docol 500DP in uniaxial tension. The curves obtained from the RVEs with only martensite in the centre and martensite both in centre and corners are the continuous and dashed lines, respectively. Evidently, the energy was predominantly absorbed in the ferrite phase through plastic dissipation. This holds true for all four RVEs. The elastic strain energy in the ferrite phase was low compared to the plastic dissipation and the increase in strain energy was small. When the martensite reached the plastic domain, the plastic dissipation in martensite grew faster than the elastic strain energy, but more so with the martensite only in the centre than with the martensite in the centre and corners. All energy curves were lower when the martensite was distributed.

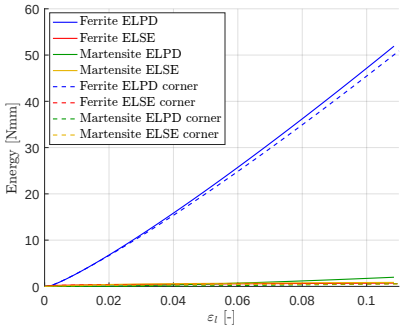

Figure 6.12: Docol 500DP: Strain energy and plastic dissipation in the different phases of the RVEs with cubical martensite.

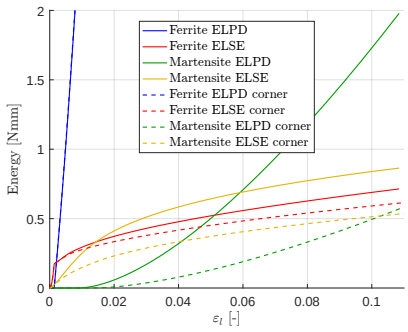

Figure 6.13: This figure shows the same graphs as the figure to the left, only zoomed in on the lower graphs.

For the spherical martensite, there was no plastic dissipation and most of the energy was accumulated as plastic dissipation in the ferrite phase. For the cubical martensite, however, there was a considerable amount of plastic dissipation; about 8.2% of the total energy with the martensite in the centre and about 3.4% with the distributed martensite. Evidently, the cubical shaped martensite was more engaged, which increased the strength. Furthermore, the same argument shows why the RVE with cubical martensite in the centre exhibited more strength than when also distributing the martensite in the corners. In summary, the energy distribution shows that the geometric shape of the martensite affects the engagement of

the martensite, and through that, the strength of the RVE.

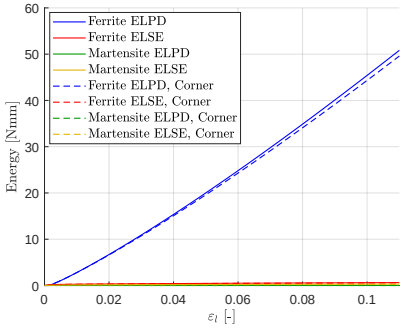

Figure 6.14: Docol 500DP: Strain energy and plastic dissipation in the different phases of the RVEs with spherical martensite.

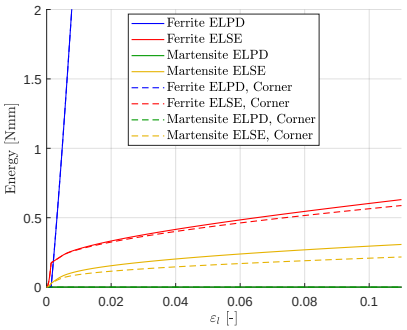

Figure 6.15: This figure shows the same graphs as the figure to the left, only zoomed in on the lower graphs.

It is worth mentioning that for Docol 1000DP, the difference in response between the RVEs with cubical and spherical centre was smaller than for the other steel qualities. A picture of the RVE with a spherical centre is shown to the left in Figure 6.16, where it is noticed that the radius of the martensite sphere was almost equal to the symmetric side length. Thus, artificial effects seemed to occur due to certain parts of the ferrite became slender. In this study, the use of the RVE with cubical martensite in the centre and corners was also restricted. When the volume fraction martensite was equal to or higher than 0.25 (as for Docol 800DP and Docol 1000DP), the martensite phases were overlapping. It is recommended to consider the geometry of these RVEs before use. RVEs where the size of the martensite is approaching the side length of RVE, or where the martensite phases in the centre and the corners are overlapping should be avoided.

Figure 6.16: Docol 1000DP: The RVEs with spherical martensite where the volume fraction is 0.50. The blue parts are the martensite, and the red parts are the ferrite.

As a basis for this study, it was assumed that the dual phase material behaviour could be represented by the material behaviour of the two phases alone. The flow curves for the ferrite and martensite were based on dislocation based theory, where the flow curves of the martensite phase were adjusted such that numerical simulations fit the experimental results obtained in a previous work. It is emphasized that the flow stress curves for both phases were calibrated in previous work, and were not necessarily optimal for the RVEs herein. However, this assumption was considered as sufficient, since the data from the RVEs with cubical martensite in the centre resembled the data from the experiments in Figure 6.1 to Figure 6.4 to a great extent. Thus, these results indicated that it was how the martensite interacted in the RVE that was of importance rather than the uncertainties in the flow curves of the martensite, and a calibration of the martensite phases was considered as unnecessary in this study.

Before constructing the RVEs, some assumptions had to be made, and their performance was a direct consequence of this. For the RVEs it was assumed simple geometry and dispersion of martensite phases, that there was fixed contact between the phases and that the edges remained straight and perpendicular to each other. In a qualitative study like this, it was therefore not deemed necessary for the simulation results to fit the experimental data perfectly. A key advantage in the RVEs was the simplistic modelling of martensitic islands. The simplicity made it easy to change the shape, the volume fraction and the distribution of the martensite. However, it also restricted the RVEs from having a volume fraction over certain thresholds for some geometries. Having a single cubical martensite phase in the centre has shown to give the most accurate results as the martensite was more engaged in this configuration. Thus, this RVE is determined to constitute the framework for plasticity and fracture of DP steels in this study, and it is focused on this RVE in the further studies. Other advantages that follow subsequently from this simplicity are that the modelling becomes straightforward and that the computational costs are severely reduced compared to more physical models, which are considered in the following section.

Introduction of a More Realistic RVE

The RVE with a more realistic distribution of the martensite phase presented in Section 3.5.1 was compared with the uniaxial tension experiments and the RVE

with cubical martensite in the centre, and they are denoted the advanced RVE, experimental data and simplified RVE, respectively. Figure 6.17 shows the true stress vs. plastic strain curves from the advanced and simplified RVEs and the experimental data in uniaxial tension. Both the advanced and simplified RVEs resembled the experiment.

Further, the advanced and simplified RVEs were exposed to biaxial tension and plane strain tension in order to evaluate the response in other stress states. The equivalent stress-strain curves are shown in Figure 6.18 and 6.19, respectively. In the case of biaxial tension a lower work-hardening rate for the advanced RVE was observed. The curves coincided in the beginning, but beyond 0.1 equivalent plastic strain, the simplified model experienced higher stress levels than the advanced model. The trend was similar when considering plane strain tension. Also in this case, higher work-hardening rate was experienced in the simplified model for large plastic strains. However, a somewhat softer behaviour in the beginning was obtained.

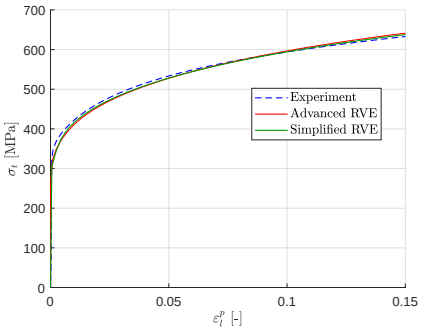

Figure 6.17: Docol 500DP: True stress vs. plastic strain curves from the experimental data, the advanced and simplified RVEs in uniaxial tension.

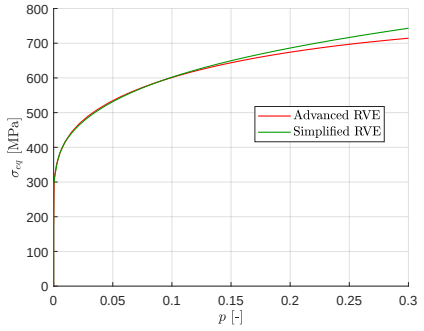

Figure 6.18: Docol 500DP: Equivalent stress-strain curves from the advanced and simplified RVEs in biaxial tension.

Evidently, the behaviour of the advanced and simplified RVEs resembled each other in uniaxial tension, biaxial tension and plane strain tension. The curves almost coincided in uniaxial tension, while differences were noticed in the work-hardening rate in the case of biaxial tension and plane strain tension, as shown in Figure 6.17, 6.18 and 6.19, respectively. The reason for the differences was the simplifications made in the simplified RVE. Locating the martensite phase in the centre and using

the homogeneous boundary condition may both have contributed to the stiffer behaviour. Since the experimental data only covered uniaxial tension, it was unclear which RVE that was the most accurate.

On the other hand, the computational time needed to run the analyses was far from equal for the two RVEs. Several hours were used in order to complete the analysis of the advanced RVE, compared to only a few minutes in the case of the simplified RVE. This demonstrates one of the main advantages of the simplified RVEs used in this study, which is that the idealised models have a greater computational effectiveness compared to models where the actual microstructure is implemented.

Lastly, the advanced RVE was modified, where homogeneous boundary conditions were used instead of periodic boundary conditions. The modified advanced RVE is compared with the original advanced model in uniaxial tension in Figure 6.20. It was observed that higher stress levels at a given equivalent plastic strain was obtained by using homogeneous boundary conditions compared to periodic boundary conditions.

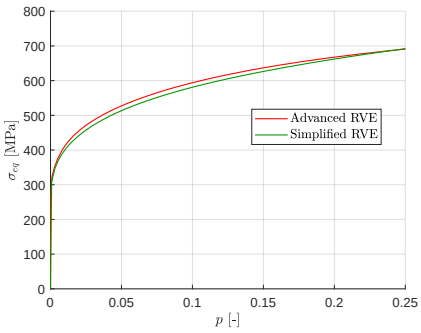

Figure 6.19: Docol 500DP: Equivalent stress-strain curves from the advanced and simplified RVEs in plane strain tension.

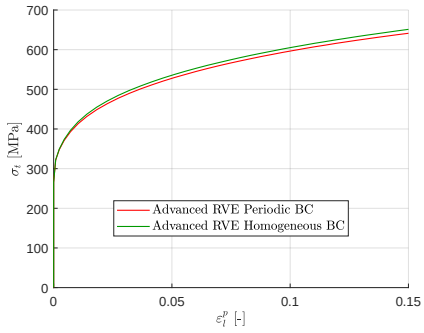

Figure 6.20: Docol 500DP: True stress vs. plastic strain curves showing the effect of implementing the homogeneous boundary conditions in the advanced RVE in uniaxial tension.

Figure 6.20 shows that a softer behaviour was obtained by using the periodic boundary conditions compared to the homogeneous boundary conditions, which was due to the homogeneous boundary conditions constraining the RVE more. According to Nygårds & Gudmundson (2002), artificial edge effects appeared when homogeneous

boundary conditions were used. However, the difference in response was small in this case. Ramazani et al. (2012) also stated that periodic boundary conditions in general give a softer response than homogeneous ones. Further in the paper, it was shown that the responses converged from above toward the same limit when the number of martensite islands increased. Based on this, the response of a simplified RVE with periodic boundary conditions would experience a larger softening than that shown in Figure 6.20, since only one martensite island was used. This was not investigated further since a softer behaviour decreases the accuracy compared to experimental data.

6.2 Iso-Curves

This section presents the iso-curves found by using the four RVEs. The iso-curves show when yielding of the material occurs at different stress states. In general, 24 points were used to create the iso-curves. As in the previous section, the data points are plotted with square and circle shapes in order to easily separate the results from the different RVEs.

In Figure 6.21, three iso-curves obtained by use of the RVE with cubical martensite only in the centre for Docol 500DP are shown together with the Hershey ($m = 6$) yield locus. The plotted iso-curves are at plastic dissipation per volume levels equivalent to that of uniaxial tension with a plastic strain of 0.1%, 0.2% and 0.5%. Similar iso-curves for all steel qualities are shown in Appendix A.3 in Figure A.3.16 to A.3.19. It is noticed that all iso-curves in Figure 6.21 resemble the shape of the Hershey ($m = 6$) yield locus. The same holds for the other steel qualities, shown in Appendix A.3. The exponent that yields the most accurate Hershey yield locus for these DP steels, $m = 6$, coincides well with previous work on yield surfaces in steels (Hershey 1954, Hosford 1972).

In Figure 6.22, the iso-curves obtained by use of the RVEs with cubical and spherical shaped martensite in the centre for Docol 500DP are presented. The lines and the squares are the points obtained by use of the RVE with a cubical centre of martensite, while the circles are the points obtained by use of the RVE with a spherical centre. Similar figures for all the steel qualities are found in the Appendix A.3 in Figure A.3.20 to A.3.23. It is evident that the spherical centre provides a softer behaviour, which is illustrated by the circle points being positioned inside

the corresponding square points. The distances between the circle points and the corresponding squares are quite constant, such that the shape of the iso-curves is similar for both the cubical and spherical martensite.

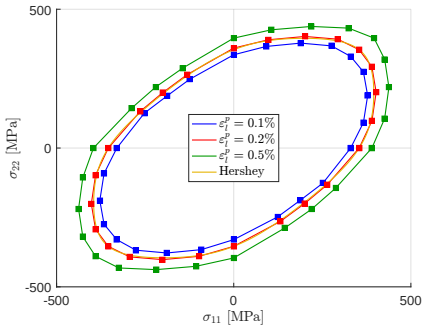

Figure 6.21: Docol 500DP: Three iso-curves obtained by use of the RVE with cubical martensite in the centre and the Hershey yield locus at 0.2% plastic strain.

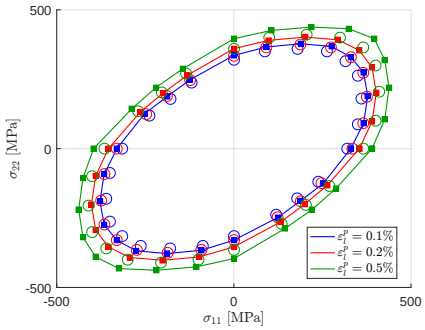

Figure 6.22: Docol 500DP: Iso-curves obtained by use of the RVEs with cubical and spherical martensite in the centre.

To evaluate the effect of distributing the martensite between multiple islands, iso-curves for RVEs with 50% of the martensite in the centre and 50% in the corners were also created. Figure 6.23 and 6.24 show the iso-curves obtained by use of the RVEs with cubical martensite for Docol 500DP and 800DP, respectively. The curves with symbols are the RVEs with martensite only in the centre, while the ones without symbols have martensite in the corners in addition. Similar curves obtained by use of the RVEs with spherical martensite for Docol 500DP and 1000DP are provided in Appendix A.3 in Figure A.3.26 and A.3.27, respectively. It is noticed that for all materials, the iso-curves for the RVEs with distributed martensite are lower than for the RVEs with all the martensite in the centre. This is consistent with the uniaxial tension simulations; the RVEs with a distributed martensite were softer than the ones with all the martensite in the centre.

All four RVEs and the different steel qualities were used to create in total twelve different sets iso-curves, where each curve differs in magnitude. The differences were the results of changing material, martensite volume fraction, distribution and shape of the martensite phase. The trends observed in uniaxial tension also appeared when considering the iso-curves. It was observed (for instance in Figure 6.22) that the RVEs with cubical shaped martensite experienced a higher stress than the cor-

responding RVEs with spherical martensite at the same plastic strain/dissipation. Furthermore, the RVEs with martensite only concentrated in the centre obtained a higher stress than the corresponding RVEs where martensite was also distributed in the corners as shown in Figure 6.23 and 6.24.

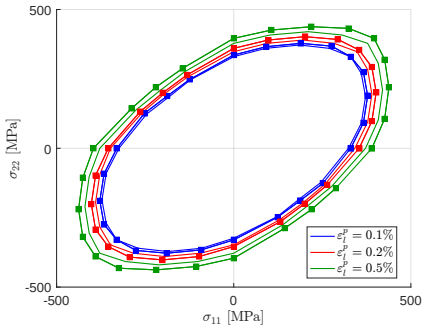

Figure 6.23: Docol 500DP: Iso-curves obtained by using the RVEs with cubical martensite only in the centre and distributed between the centre and the corners.

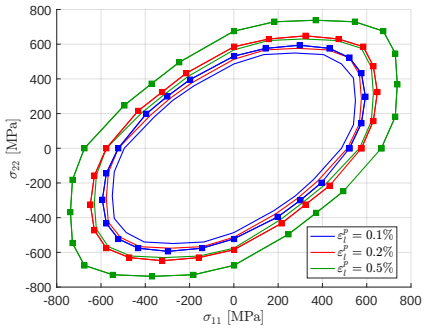

Figure 6.24: Docol 800DP: Iso-curves obtained by using the RVEs with cubical martensite only in the centre and distributed between the centre and the corners.

The iso-curves found by use of the different RVEs resembled the Hershey yield criterion. To determine whether the iso-curves obtained by using the different RVEs were reasonable or not, they were compared with results obtained by using an experimentally approach. The expansion of the yield surface has been experimentally investigated by Hou et al. (2019) for the materials DP590, DP780 and DP980, which corresponds to Docol 600DP, 800DP and 1000DP, respectively, and is shown in Figure B.1.1 to B.1.3. Hou et al. (2019) stated that it was necessary to use an anisotropic yield criterion combined with a non-associated flow rule to obtain the best fit. That an anisotropic yield criterion with a non-associated flow rule provided the better accuracy was as expected, since more parameters were used to create the fit to the experimental data.

However, it was noticed that the shape of the yield surfaces obtained experimentally and the shape of the iso-curves from this study were quite similar when comparing Figure B.1.1-B.1.3 with corresponding iso-curves in Figure A.3.21-A.3.23. One thing to note was that the Hershey yield locus was reasonably accurate, based on its simplicity and the complex microstructure in DP steels. This result contradicts that from Nygårds & Gudmundson (2002), who found that a Hill criterion

was more appropriate when a two phase ferritic/pearlitic steel was considered. For that result, a very different plane strain 2D RVE was used, which is most likely the reason for the deviance in the shape of the iso-curves compared to the ones from Hou et al. (2019) and those created herein.

6.3 Kinematic Hardening

The cyclic load laboratory tests were numerically reproduced by use of the RVEs. This was done in order to investigate the Bauschinger effect in DP steels as a function of the martensite volume fraction. Figure 6.25 and 6.26 show the results obtained from the laboratory tests and by use of the RVE with cubical martensite in the centre for Docol 500DP, respectively. Red symbols indicate the points of load reversal, while the blue symbols indicate the yielding after load reversal at 0.2% equivalent plastic strain higher than at the corresponding load reversal. The results for all steel qualities and for all four RVEs are included in Appendix A.4 in Figure A.4.28 to A.4.42.

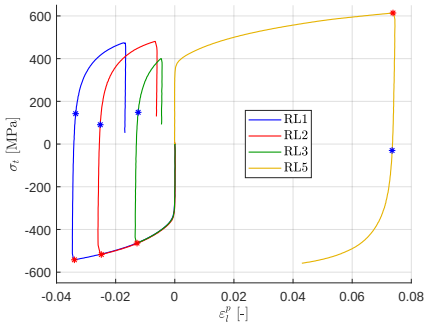

Figure 6.25: Docol 500DP: True stress vs. plastic strain curves from the laboratory tests. Red and blue points indicate load reversal points and yield points, respectively.

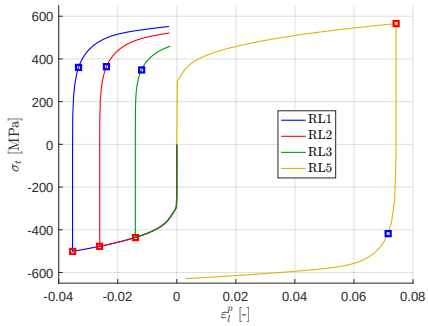

Figure 6.26: Docol 500DP: True stress vs. plastic strain curves from the RVE with cubical martensite in the centre. Red and blue points indicate load reversal points and yield points, respectively.

When taking into account Figure 4.5, which shows that the specimens in the cyclic load laboratory tests were overly stiff compared to the uniaxial tension ones, the difference in stress between the experiments and the RVEs was as expected. The results from the RVE with cubical martensite in centre resembled the laboratory tests, while the other RVEs provided results that were too soft. After load rever-

sal, it was observed that the yield stress was lower than the stress at load reversal. This is illustrated by the blue symbols, which have a lower stress magnitude than the red ones for all the tests. This means that there was at least some kinematic hardening in the RVEs.

Figure 6.27 and 6.28 show the r-ratio obtained from the laboratory tests and from the RVE with cubical centre, respectively. Clearly, the Bauschinger effect experienced was consistently lower for the RVE than for the experiments. The reason for this is that mechanisms other than the strength difference between the phases contribute to the Bauschinger effect in DP steels, which are evidently not captured in the RVE. As mentioned earlier, Kocks & Mecking (2003) stated that there exists both a Masing effect in polycrystals and transient effects within single crystals, which contribute to the Bauschinger effect. These effects were not captured because of the simplicity inherent in the RVEs. To get a sense of the magnitude of the other effects, the difference in r-ratio between the numerical and experimental obtained data may give a reasonable estimate.

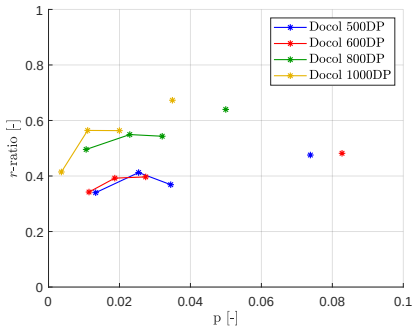

Figure 6.27: The r-ratio from the laboratory tests for all steel qualities.

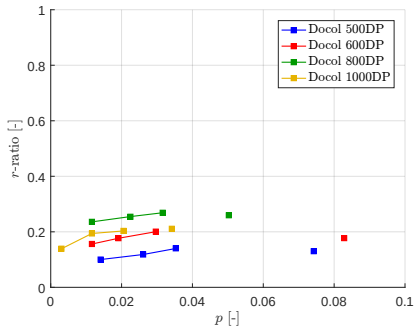

Figure 6.28: The r-ratio from the RVE with cubical centre for all steel qualities.

Similar plots for all four RVEs are provided in Appendix A.4 in Figure A.4.43 to A.4.46. When comparing the RVEs with cubical to the RVEs with spherical martensite in the centre, the ones with a spherical martensite displayed the least amount of kinematic hardening. One reason for this is that, as explained earlier, the degree to which the martensite is engaged depends on its geometrical shape. With a greater stress in the martensite phase, a greater stress will be applied to the ferrite phase in the case of load reversal, which increases the r-ratio.

Figure 6.28 shows that the Bauschinger effect experienced in the RVE increased with the steel qualities, except for Docol 1000DP where it decreased compared to Docol 800DP. This is reasonable because not only the martensite volume fraction affects the Bauschinger effect experienced in the RVE. The strength differences between the phases also play an important role. The Docol 1000DP martensite flow curve was considerably lower than the corresponding flow curve for the other steel qualities (Figure 3.6), which decreased the Bauschinger effect compared to Docol 800DP even though the martensite volume fraction increased. Further in Figure 6.28, it is not evident that the largest effect occurs in tension and at large plastic strains as observed in Figure 6.27. This supports the suggestion regarding that in the laboratory tests during tension, the specimen became more slender, which relaxed the springs and caused an earlier yield after load reversal. It is still emphasized that this is only speculations around the observed trend.

Further, the two RVEs with martensite concentrated in the centre were used to investigate the effect of only changing the martensite volume fraction, while keeping the material properties of each phase constant. This was done for Docol 500DP, which had the martensite phase of highest strength and weakest ferrite phase of all steel qualities considered. The applied load corresponded to the $RL1$ laboratory test. Figure 6.29 shows the different r-ratios obtained by only changing the volume fraction of the martensite. As previously mentioned, the Bauschinger effect comes here solely from the difference in strength between the two phases. The Bauschinger effect approached zero when the volume fraction went towards either 0% or 100%, and the Bauschinger effect peaked at a volume fraction of 60% martensite, which corresponded to an r-ratio of 0.5.

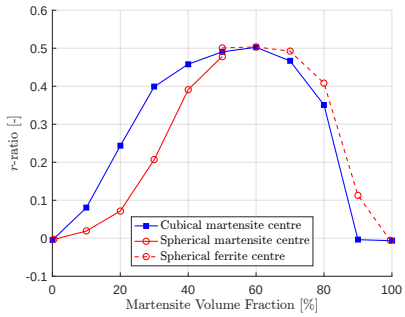

Figure 6.29: Docol 500DP: The Bauschinger effect shown in terms of the r-ratio when varying martensite volume fraction in the RVEs with martensite only in the centre.

Up to 50% volume fraction, the RVE with a cubical centric martensite had a higher Bauschinger effect than the RVE with a spherical centric martensite. At 50% volume fraction, the RVE with spherical centric martensite exhibited a leap in the Bauschinger effect as a result of the ferrite and martensite phases switching places. This was done because the radius of the martensite sphere exceeded the limits of the RVE beyond this volume fraction. The results beyond 50% martensite volume fraction for the RVE with a centric sphere are plotted with a dashed line, and should be treated with caution, as the effect of inverting the phase placement has not been examined thoroughly.

It is also seen that a martensite volume fraction in the range 20-80% was necessary to obtain a significant contribution to the Bauschinger effect. The contribution was small when the martensite volume fraction was 10% or less. For comparison, Docol 500DP had a martensite volume fraction of 13%. It is expected to achieve similar trends if this numerical investigation had been conducted with the other steel qualities. However, the peak value of the r-ratio is probably going to decrease, since the strength difference between the ferrite and the martensite phase is the largest in Docol 500DP.

6.4 Fracture

The results from the fracture study conducted with the RVE with cubical martensite in the centre are presented in the following. The objective was to investigate whether or not the described void nucleation, growth and coalescence in DP steels could be reproduced by the idealized RVE. This was done by introducing the Gurson model and an initial void volume fraction into the ferrite material model. Abaqus/Explicit was used such that the porous failure criterion became available. As explained in Section 5.2, a hybrid formulation of the element should be used to alleviate volume locking when the Gurson model is used. However, it was not available when using Abaqus/Explicit. The element type used was the C3D10M, and it was chosen based on the recommendation in the Abaqus Analysis User's Guide section 28.1.1. It was chosen to only calibrate the initial void volume fraction parameter, f_0. The other parameters, q_1, q_2, q_3, f_c and f_F, were fixed with the values 1.5, 1.0, 2.25, 0.02 and 0.2, respectively. The calibration was done for all materials by use of the RVE with cubical martensite in the centre.

In Figure 6.30 to 6.33, the engineering stress-strain curves obtained with the RVE by varying the initial void volume fraction are shown for all the steel qualities. They were compared to the experimental data obtained from the uniaxial tension tests. Note that this is not a realistic comparison. The uniaxial tension specimens experienced geometrical softening due to necking in addition to the material softening. However, the uniaxial tension tests were used as references since no other data were available. Of that reason, it was not crucial that the curves from the RVE and the experiment resembled each other, as the main objective was to describe how the used parameters influenced the results and to investigate the obtained fracture mechanism.

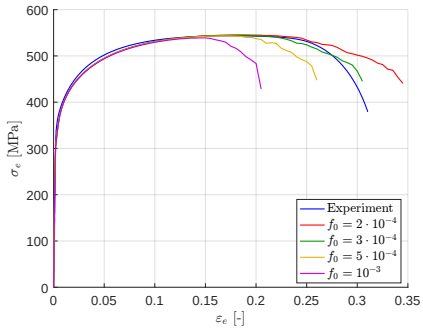

Figure 6.30: Docol 500DP: Engineering stress-strain curves for the RVE with cubical centre when varying f_0.

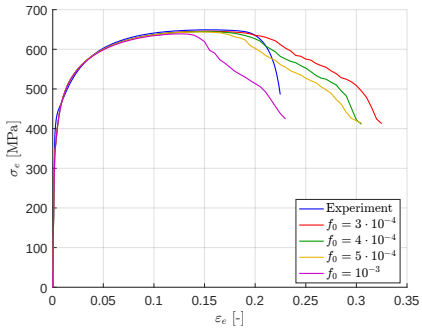

Figure 6.31: Docol 600DP: Engineering stress-strain curves for the RVE with cubical centre when varying f_0.

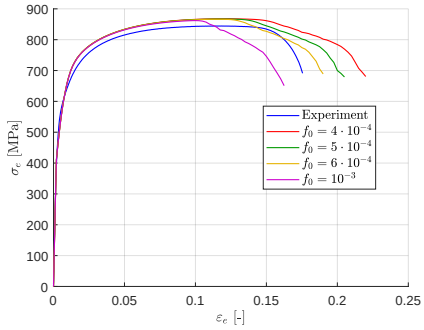

Figure 6.32: Docol 800DP: Engineering stress-strain curves for the RVE with cubical centre when varying f_0.

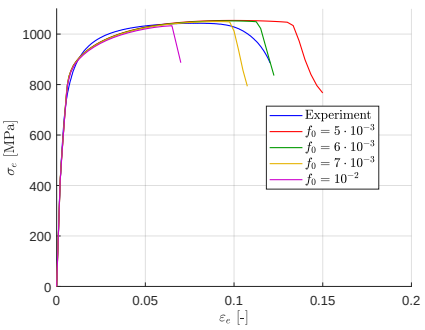

Figure 6.33: Docol 1000DP: Engineering stress-strain curves for the RVE with cubical centre when varying f_0.

Evidently in Figure 6.30 to 6.33, the higher the initial void volume fraction was, the earlier fracture occurred in the RVEs. A rough estimate of a representative value for the initial void volume fraction was obtained such that fracture was initiated at the same strain for the RVE and the experiment. This was done by considering the engineering stress-strain curve, and the initial void volume fraction was found nearly equal for Docol 500DP, 600DP and 800DP, while a significantly larger initial void volume fraction was necessary for Docol 1000DP. The initial void volume fractions, f_0, obtained this way are given in Table 6.1 for the different steel qualities.

Table 6.1: A rough estimate of a representative value for the initial void volume fraction parameter for each steel quality.

DP Steel	f_0 [-]
Docol 500DP	$3 \cdot 10^{-4}$
Docol 600DP	$4 \cdot 10^{-4}$
Docol 800DP	$4 \cdot 10^{-4}$
Docol 1000DP	$7 \cdot 10^{-3}$

First, it is emphasized that the parameters in the Gurson model are not uniquely defined, and similar results may be obtained by using different sets of parameters. The void volume fraction is multiplied by q_1 in Equation (2.3). Hence, an increase of the void volume fraction, f, may be compensated by a decrease of q_1. Faleskog et al. (1998) estimated the q_i-parameters as a function of strain hardening rate by using unit cells, where values other than the standard values for metals were found. Further, it was stated that properly calibrated q_i values were important to correctly reproduce fracture with the Gurson model. Thus, the material parameters used in this study may be inappropriate for the DP steels. However, the q_1 and q_2 values used for DP steels in the literature are ambiguous. Parameter values both below and above the recommended standard parameters values for metals occur (Santos et al. 2019, West et al. 2012). Considering the time required for calibrating the q_i-parameters and that a different parameter set would probably be obtained for each steel quality, makes the comparison between the materials challenging. The assumption made regarding the use of standard values in the Gurson model for all materials was considered as sufficient in this study.

The influence of the parameters f_0, f_c and f_F was evaluated by considering the evolution of the void volume fraction in the model. Figure 6.34 shows the void volume fraction from the integration point with the greatest void volume frac-

tion as a function of engineering strain. A steady void growth was obtained from the f_0 listed in Table 6.1 to the $f_c = 0.02$. The void growth accelerated beyond this point. This shows how the Gurson model takes void coalescence into account when the porous failure criterion is utilized. The corresponding engineering strains were approximately 0.17, 0.16, 0.14 and 0.10 for the different steel qualities, which approximately corresponds to where the engineering stress-strain curves in Figure 6.30 to 6.33 start decaying, respectively. The void growth continued until the void volume fraction reached $f_F = 0.2$, where all stress carrying capacity in that integration point was lost. The element is removed when all its integration points have failed.

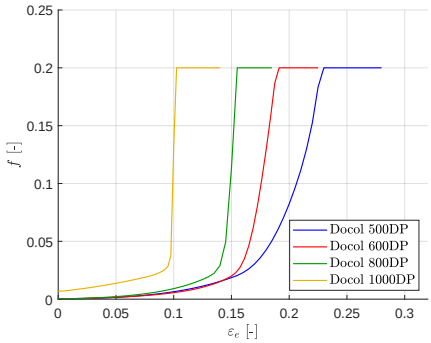

Figure 6.34: Void volume fraction from the integration point with the greatest void volume fraction as a function of engineering strain for the different steel qualities.

Evidently, all parameters were important for the void evolution, and the results could be significantly changed by adjusting these parameters. For instance, the curves in Figure 6.34 would shift to the left and right if f_0 and f_c were increased, respectively. Furthermore, an increase of f_F would delay the complete loss of stress carrying capacity. The slope of these curves depends on the $\bar{f}_F$ parameter, which is a function of the q_i parameters, as shown in Equation (2.8). Summarized, each of the void volume fraction parameters, f_0, f_c and f_F, were crucial in this case in order represent the material behaviour correctly.

It is still emphasized that the f_0-parameter in the Gurson model used in the RVEs exposed to uniaxial tension should give conservative estimates. In addition to material softening due to evolution of voids, the specimen experienced geometrical softening because of cross section area reduction. Only material softening was

present in the RVE through the Gurson model, and it must therefore be more extensive to compensate for the absence of geometrical softening.

Experimental studies have indicated that the initial void volume fraction in DP steels was not important for the fracture mechanism. Toda et al. (2017) analyzed the damage evolution in DP steels with 30% martensite volume fraction by considering images from experiments. It was observed that the voids were present at early stages in the loading process. However, these voids exhibited only moderate void growth. After maximum load, further void nucleation caused by martensite cracking was observed. These voids experienced rapid growth and dominated the ductile fracture mechanism. Thus, the initial void volume fraction may be of minor importance for fracture in DP steels, and the key mechanism to capture seems to be the rapid growth of voids beyond load maximum. Notice that this is not a contradiction of the discussion in the paragraphs above, and it does not imply that the f_0-parameter in the Gurson model is of minor importance. It only means that the void evolution in the experiments and in the Gurson model were different in this case. Since no void nucleation was introduced into the Gurson model, the f_0-parameter was essential in order to initiate the void growth.

The void nucleation feature in the Gurson model could be considered as an alternative to the initial void volume fraction feature. Three void nucleation parameters describe the nucleation in a statistical sense, which provide more flexibility compared to the f_0-parameter. The void nucleation could be beneficial if the desire is to ensure void evolution only beyond load maximum as described by Toda et al. (2017). By choosing a small standard deviation, S_N, the voids would mainly nucleate close to the expected plastic strain at nucleation, ε_N, in contrast to the initial void volume fraction feature where the voids are present initially. The amount of void nucleation is controlled by the void volume nucleation fraction, f_N, which could be chosen in the order of magnitude of the f_c-parameter to ensure rapid void growth after nucleation. Another alternative could be to choose a large f_N-parameter. In such a case, the void growth becomes superfluous since the void nucleation feature ensures the rapid void evolution. Combining a small standard deviation, S_N, and a large void volume nucleation fraction, f_N, results in a large and sudden increase in void volume fraction, which could be called a nucleation burst.

However, such nucleation bursts have a main disadvantage. As stated in Chapter 2, the void growth increases with the hydrostatic stress, which implies that the plastic strain to failure decreases when the hydrostatic stress increases. Thus, the expected plastic strain at nucleation, ε_N, should be a function of the hydrostatic stress to provide accurate results when the stress state changes. The ε_N-parameter does not depend on the hydrostatic stress state, meaning that the void evolution cannot be controlled solely by a nucleation burst. Notice how this deficiency is to a lesser extent present when the initial void volume fraction feature is utilized since the voids are present from the beginning.

However, using the Gurson model when the stress triaxiality is low has been reported to yield poor results (Gologanu et al. 1993). The Gurson yield criterion (Equation (2.3)) does not include the Lode parameter, which is important for the ductility in such stress states. Several improvements of the Gurson model are proposed in the literature to increase the accuracy when the stress state changes, consequently increasing the complexity of the original Gurson model (Madou & Leblond 2012). This fracture study was limited to only consider stress triaxiality equal to 0.33. It would have been interesting to investigate fracture in other stress states with high and low stress triaxialities as well, such as biaxial tension and pure shear, respectively.

Further, the failure mechanism in the RVE for the different steel qualities was investigated in uniaxial tension. The initial void volume fractions presented in Table 6.1 were used. Figure 6.35 to 6.38 present contour plots of the equivalent plastic strain right after initiation of element erosion, where the martensite phase was removed for illustration purposes. It was noticed that the element erosion occurred where the plastic strain was localized and where the void volume fraction was largest, which was either at the ferrite-martensite boundary or on the outer loading surface.

Ductile fracture is frequently studied in the literature, where it is reported that nucleation, growth, and coalescence of voids are the main mechanisms. In DP steels, the nucleation of voids is caused by either cracking of martensite particles or by decohesion of the ferrite-martensite interface. Here, an initial void volume fraction was introduced into ferrite material model, while no failure criterion was introduced in the martensite. Thus, the desired fracture mechanism in the RVE

was strain localization at the ferrite-martensite interface, which causes rapid void growth that eventually leads to reduction of stress carrying capacity followed by element erosion. This represents the decohesion of the ferrite-martensite interface. The decohesion of the ferrite-martensite interface was present for Docol 500DP and 600DP, as shown in Figure 6.35 and 6.36.

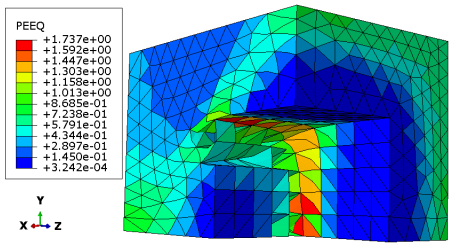

Figure 6.35: Docol 500DP: Contour plot of the equivalent plastic strain in the RVE where the cubical martensite in centre was removed. The picture was taken right after the element erosion had started.

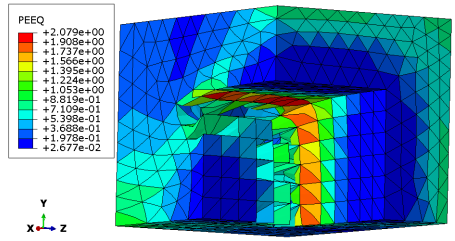

Figure 6.36: Docol 600DP: Contour plot of the equivalent plastic strain in the RVE where the cubical martensite in centre was removed. The picture was taken right after the element erosion had started.

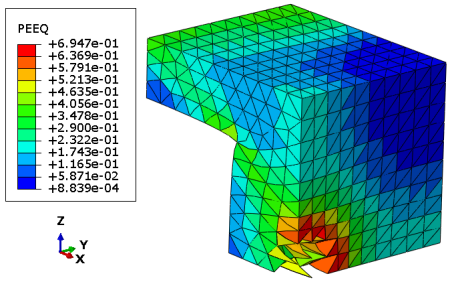

Figure 6.37: Docol 800DP: Contour plot of the equivalent plastic strain in the RVE where the cubical martensite in centre was removed. The picture was taken right after the element erosion had started.

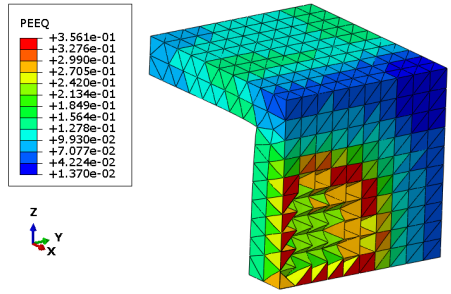

Figure 6.38: Docol 1000DP: Contour plot of the equivalent plastic strain in the RVE where the cubical martensite in centre was removed. The picture was taken right after the element erosion had started.

In contrast, Figure 6.37 and 6.38 show that for Docol 800DP and 1000DP, the desired fracture mechanism was not present and all of the element erosion was located at the loading surface. The element erosion occurred due to the large stress and strain concentrations observed at the loading surface. This was more evident for Docol 1000DP, and may indicate that the idealized RVE where all of the martensite was located in the centre led to more inaccuracies when the martensite volume frac-

tion increased, and substantiated the speculation about artificial effects appearing when the martensite phase becomes too large in size.

Despite this, the desired fracture mechanism for Docol 500DP and 600DP was achieved, which implies that reasonable results were obtained by introducing f_0, f_c, and f_F in the Gurson model. It is possible that the desired failure mechanism for Docol 800DP and 1000DP was not captured since martensite particle cracking was not included in the RVE in this study. According to Speich et al. (1979), void formation in DP steels occurs because of decohesion of the ferrite-martensite interface for low martensite volume fractions and martensite particle cracking for high martensite volume fractions. Moreover, as previously mentioned, Toda et al. (2017) stated that martensite particle cracking initiated the rapid void growth beyond maximum load when the martensite volume fraction was 30%. In comparison, the martensite volume fraction in Docol 800DP and 1000DP is 25% and 50%, respectively. Thus, it is plausible that the Gurson model used with f_0, f_c and f_F was insufficient in representing the void evolution, and that particle cracking must be introduced in the models of these steel qualities in order to initiate the void evolution at the ferrite-martensite interface.

In order to represent the martensite particle cracking, a brittle failure criterion could be introduced into the martensite material model. This would affect the void evolution indirectly. The particle cracking would decrease the strength contribution from the martensite, which would increase the stresses and strains in the ferrite phase and eventually lead to more void growth. Thus, the brittle failure criterion would not be considered as void nucleation in the Gurson model, but it would increase the void growth since the stresses and strains in the ferrite increase. This was not investigated further in this study since attention was only given to the ferrite phase and the Gurson model. Furthermore, it is expected that the morphology of the martensite becomes increasingly important when introducing a brittle failure criterion, and that the idealized RVE with cubical martensite only in the centre would give different results than an RVE with more realistic martensite distribution. However, this is only speculations, and it would be interesting to investigate the influence of a brittle failure criterion.

Another feature in Abaqus that could be used to represent the decohesion of the ferrite-martensite interface is the cohesive zone modelling. The cohesive behaviour could be considered as an attraction between different instances or as sticky particles. The cohesive behaviour could be modelled in Abaqus either by introducing cohesive elements or by defining a cohesive interaction between surfaces. In addition to the cohesive behaviour, damage initiation and evolution could be introduced such that the cohesive behaviour could diminish as the deformation continues. For further information regarding how to model the cohesive behaviour by use of cohesive elements and surface interaction it is recommended to read the Abaqus Analysis User's Guide section 32.5.1 and 37.1.10, respectively (ABAQUS 2019). For DP steels, the cohesive behaviour could be applied at the ferrite-martensite interface. An advantage of such modelling is that the fracture is forced to be located at the ferrite-martensite interface.

It is reported in the literature that the desired decohesion of ferrite-martensite interface was obtained by using cohesive zone modelling (Cornec et al. 2003, Sirinakorn & Uthaisangsuk 2018, Uthaisangsuk et al. 2009). However, the cohesive zone modelling has a disadvantage when it comes to the input parameters in the damage initiation and evolution. They are difficult to estimate based on physical quantities, and a trial and error sequence is often needed to obtain reasonable results. An attempt on the cohesive zone modelling based on surface interaction was conducted in this study. The results was not satisfactory, and of that reason it was omitted from this report. Convergence problems arose due to penetration of the sharp corners of the cubical martensite, and the results were considered as untrustworthy. A mesh refinement of the martensite phase was tested as an attempt to alleviate the convergence problem, but no improvement was observed. Further investigation was not conducted in this study. However, it is believed that the convergence problems experienced in this study could be alleviated by using cohesive elements, and it is recommended that any further investigation with cohesive zone modelling with the idealized RVE is based on that.

7 Homogenization

The objective of the homogenization was to propose and calibrate a material model for the DP steels based on the experimental data and the micromechanical modelling. This was done by conducting the micro-macro approach described in Section 3.6. In the following, keep in mind the simplicity of the approach. The behaviour of the complex DP steel microstructure was approximated by the idealized RVE and an applicable material model for DP steel was obtained by conducting this approach. This homogenization strategy is superior in terms of computational efficiency compared to the first-order homogenization strategy presented in Chapter 2.

The approach was based on the fracture strain of the central hole experiments. The idealized RVE with cubical martensite in the centre and Abaqus/Standard was used consequently. The approach was repeated for each steel quality, but primarily results obtained by using Docol 500DP are presented in the report. Docol 500DP was chosen since it provided the most accurate results. Similar figures as presented below obtained with the other materials are presented in Appendix A.5. It is not referred to these figures in the following text; however, they are presented in the same order as done below, and it should be easy for the reader to locate the corresponding figures for the other steel qualities.

The first step of the approach was to calibrate the plasticity parameters of a material model consisting of a homogeneous material for each steel quality. The calibration was based on the idealized RVE with cubical martensite in the centre exposed to uniaxial tension. Furthermore, three terms were used in the Voce hardening laws to fit the true stress vs. plastic strain curves up to a plastic strain of unity. The calibrated parameters of the Voce hardening laws are listed in Table 7.1, and the fitted stress-strain curve is shown together with the simulation of the RVE (without implementation of the Gurson model) for Docol 500DP in Figure 7.1. It is noticed that the fitted stress-strain curves coincide with the RVEs that they were based upon.

The micro-macro approach continued by conducting the central hole tests both

experimentally and numerically, where the previously calibrated material models were used in the numerical simulations. The engineering stress-strain curves from both are presented in Figure 7.2 for Docol 500DP. It is noticed that the numerical model resembled the experiment in the beginning, while larger differences occurred towards the end. For the other steel qualities, the stress level in the numerical model was too high in general. The observed differences were probably related to the work-hardening laws chosen, and the influence of work-hardening laws is investigated after completing the approach.

Table 7.1: The Voce hardening law parameters for the homogeneous material model for each steel quality based on the idealized RVE with cubical martensite in the centre.

DP Steel	σ_0 [MPa]	Q_{R1} [MPa]	C_{R1} [-]	Q_{R2} [MPa]	C_{R2} [-]	Q_{R3} [MPa]	C_{R3} [-]
Docol 500DP	290.7	129.2	168.6	209.8	10.68	455.3	0.805
Docol 600DP	319.3	159.5	217.2	170.9	23.32	344.4	2.649
Docol 800DP	407.4	310.2	198.0	181.4	22.75	281.7	3.600
Docol 1000DP	440.5	445.4	584.6	297.4	20.54	90.00	5.001

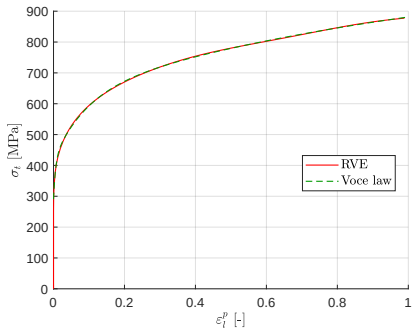

Figure 7.1: Docol 500DP: True stress vs. plastic strain curve obtained with the calibrated Voce hardening law shown together with the RVE with cubical centre it was based upon.

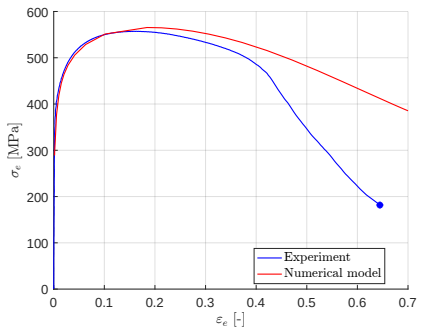

Figure 7.2: Docol 500DP: Engineering stress-strain curves from experimental and numerical central hole test. Blue star marks where fracture occurred in the experiment.

The engineering strain where the specimen fractured experimentally is marked with a blue star. This engineering strain was identified in the numerical model, and the corresponding increment was defined as the increment where final fracture should occur. Further, the critical element in the numerical model was located as the element with the largest equivalent plastic strain at final fracture. Both the true stress-strain curve and the stress triaxiality, σ^*, for this element were extracted

from the model and are shown in Figure 7.3 and 7.4, respectively. The true stress-strain curve was obtained by using the element stress and strain components in the loading direction (x-direction in Figure 3.9), which are denoted in the following as σ_{11} and ε_{11}, respectively. For simplicity, an average triaxiality, $\overline{\sigma}^*$, was calculated. It is shown as the red curve in Figure 7.4 and is listed in Table 7.2 for all steel qualities. The average triaxiality was applied to the RVE, and the true stress-strain curve obtained in the same way as for the critical element is included in Figure 7.3. The increment that corresponds to the final fracture in the specimen is marked with a red star to show at what strain fracture should occur. Small discrepancies were observed between the curves, which were mainly caused by the small differences in the stress state.

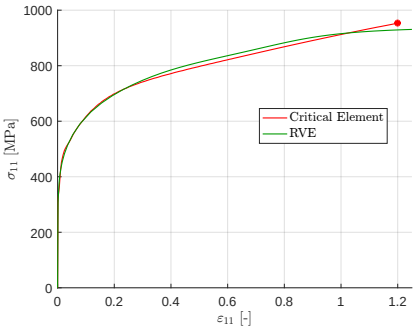

Figure 7.3: Docol 500DP: True stress-strain curve from the critical element shown together with RVE exposed to the average stress triaxiality.

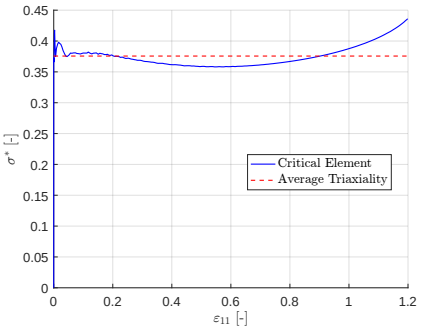

Figure 7.4: Docol 500DP: Stress triaxiality in the critical element shown together with the calculated average stress triaxiality.

Table 7.2: The average stress triaxiality based on the triaxiality in the critical element.

DP Steel	$\overline{\sigma}^*$ [-]
Docol 500DP	0.37
Docol 600DP	0.35
Docol 800DP	0.38
Docol 1000DP	0.35

For Docol 500DP, the critical element experienced strains larger than what the calibrated Voce hardening law was based upon. As a result, the end of the critical element curves were affected by extrapolation of the work-hardening law, which was considered unfavourable. The deformation of the critical element where ex-

trapolation was used corresponded to about 20% of the total deformation. It was assumed that the extrapolation of the work-hardening was sufficient in this case. However, it is recommended that the work-hardening law used in further work covers the whole deformation of the critical element to lower the uncertainties.

Introduction of the Gurson model into the RVE exposed to the average stress triaxiality was the next step in the approach. The goal of this step was to observe how the different features implemented into the Gurson model affected the overall behaviour of a heterogeneous microstructure. The initial void volume fraction and the void nucleation features were implemented in the Gurson model separately. This step resembled the investigation done in Section 6.4, but it had some differences. As mentioned in Section 3.6, the Riks-algorithm was utilized to obtain the desired stress triaxiality, and the porous failure criterion was not available. The hybrid formulation of the element, C3D10H, was tested. However, the simulations stopped prematurely as described in Section 5.2; thus, the normal C3D10 elements were used. Figure 7.5 and 7.6 show the results from introducing either initial void volume fraction or void nucleation, respectively. Only the expected plastic strain at nucleation, ε_N, was varied when considering void nucleation, while the standard deviation and void volume nucleation fraction were fixed with the values $S_N = 0.05$ and $f_N = 0.01$, respectively.

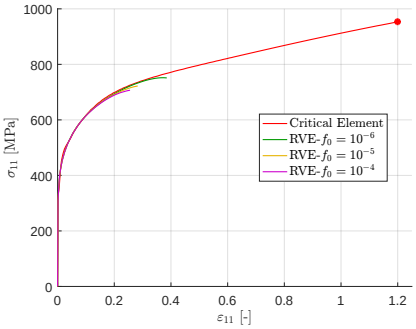

Figure 7.5: Docol 500DP: True stress-strain from the critical element and the RVE where the initial void volume fraction, f_0, feature was included and exposed to the average stress triaxiality.

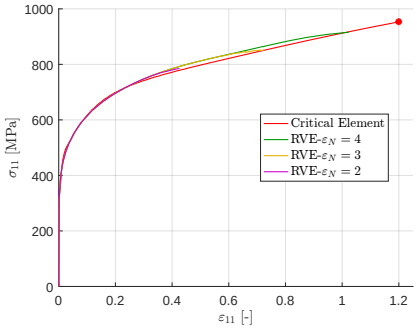

Figure 7.6: Docol 500DP: True stress-strain from the critical element and the RVE with the void nucleation feature controlled by changing ε_N included and exposed to the average stress triaxiality.

A rapid void growth when the strain increased was observed when using the initial void volume fraction feature in the Gurson model. Considering Figure 7.5, the

desired strain level was not achieved regardless of the f_0-parameter. Evidently, the stress and strain concentrations in the model led to a rapid void growth in the RVE as long as voids were present. The void evolution was affected by changing the initial void volume fraction, but the changes were insignificant compared to the desired strain level obtained in the critical element. In this case, it is evident that the initial void volume fraction feature was inadequate. It is more reasonable to compare the RVE with the critical element in the specimen than with the whole specimen. The RVE and the critical element experienced only material softening, and the effect of the geometrical softening was excluded from the results. This is in contrast to the former conducted fracture study where the uniaxial tension test specimens were used as reference cases.

Figure 7.6 shows that the desired strain level could be obtained by using the void nucleation feature when the expected plastic strain at nucleation, ε_N, was large. As for the case when using initial void volume fraction, these findings indicate that rapid void growth occurred in the RVE when the strain increased. However, the three parameters available using the void nucleation feature provided more flexibility compared to the f_0-parameter. By using $\varepsilon_N = 4$, $S_N = 0.05$ and $f_N = 0.01$, initiation of the rapid void growth was delayed. Note, this step was independent of the material models that were the results of the approach.

Including damage in the homogenized model was considered next in the approach. Here, the single element with the homogeneous material model, as shown in Figure 3.10, was exposed to the same triaxiality as the RVE. The goal of this step was to fracture the single element at the critical element fracture strain. This was done by including the Gurson model into the material model listed in Table 7.1, where either the initial void volume fraction or the void nucleation feature was introduced. Thus, the goal was to obtain a rapid reduction of the stress carrying capacity of the single element at the red star in Figure 7.3.

The results are shown in Figure 7.7 and 7.8 for initial void volume fraction and void nucleation, respectively. Evidently, a large initial void volume fraction needed to be introduced in order to notice the material softening in the single element. It is observed that the initial void volume fraction decreased the overall stress level. This indicates a steady void growth, and that the desired rapid void growth was not achieved in the single element. As for the RVE, more promising results were

obtained by using the void nucleation feature. The desired reduction of stress carrying capacity was achieved at the critical element fracture strain through nucleation burst by choosing $\varepsilon_N = 1.3$, $S_N = 0.05$ and $f_N = 0.3$.

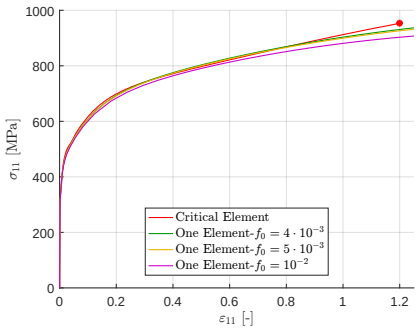

Figure 7.7: Docol 500DP: True stress-strain curves from the critical element and the homogeneous element where the initial void volume fraction, f_0, was included and exposed to the average stress triaxiality.

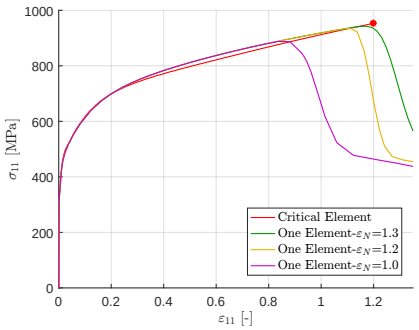

Figure 7.8: Docol 500DP: True stress-strain curves from the critical element and the homogeneous element where the void nucleation was included and exposed to the average stress triaxiality.

It is emphasized that the void nucleation parameters chosen here were not based on experimental observation, but introduced to ensure the desired rapid loss of stress carrying capacity. The authors of this study were aware that a void volume nucleation fraction of 0.3 was substantial and not necessarily realistic. Other combinations of the parameters could have been chosen and still achieved the desired reduction of stress carrying capacity. For instance, a smoother reduction would be obtained if the standard deviation was increased, while a smaller reduction would be obtained if the void volume nucleation fraction was decreased. However, the chosen parameters were considered sufficient since the goal was achieved.

Furthermore, the deficiency mentioned in Section 6.4 regarding the void nucleation feature is once again emphasized. The ε_N-parameter was not a function of the stress triaxiality. Thus, it is expected that the chosen combination of parameters yields poor results if the stress state changes. This deficiency could be remedied by use of a stress-driven void nucleation. Petit et al. (2019) used a Gurson model with stress- and strain-driven nucleation. Instead of the void nucleation described in Equation (2.7), a stress-driven nucleation criterion was included where the A-parameter in Equation (2.6) was a function of both the maximum principal stress and the plastic strain. Also stress-driven nucleation where the A-parameter was a

function of the stress triaxiality has been used in the literature (Dalloz et al. 2009). The stress-driven nucleation was not investigated further in this study since it was not available in Abaqus.

The final step of the micro-macro approach was to carry out a numerical simulation of the central hole test where only the symmetry plane in the thickness was used and where the homogeneous material model calibrated during this approach was used. A picture of the numerical model is shown in Figure 3.11. The goal was to represent fracture by obtaining an abrupt reduction of stress carrying capacity at the fracture strain. The use of initial void volume fraction in the Gurson model alone was considered as inadequate based on the results obtained with both the RVE and the single homogeneous element. Void nucleation provided more flexibility, and was considered appropriate in order to reproduce the desired rapid void growth. Thus, void nucleation parameters based on the single homogeneous material were used in the final simulation. For Docol 500DP, the parameters used were $\varepsilon_N = 1.3$, $S_N = 0.05$ and $f_N = 0.3$. Figure 7.9 shows the engineering stress-strain curves from the experiment and the final numerical simulation. In contrast to the preliminary results, the final numerical simulation shows an abrupt change at engineering strain 0.64. This corresponded to the fracture strain in the experiment, which is marked as the blue star.

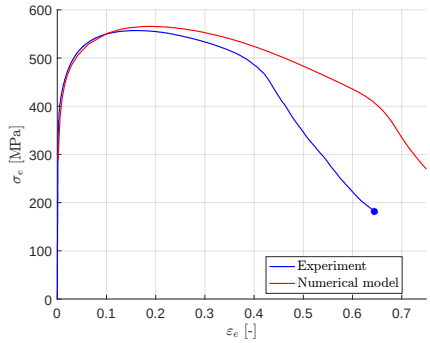

Figure 7.9: Docol 500DP: Engineering stress-strain curves from the experiment and the final simulation of central hole simulation.

Summarized, the objective of the micro-macro approach was to propose material models for the DP steels, called the homogeneous materials herein, that could be used in large scale simulations of structural components. The approach was based

on experimental data and micromechanical analyses. The central hole experiments were used as reference cases, and the main priority was to predict the fracture strains with sufficient accuracy. Porous elasto-plastic material models were proposed, where the Gurson model was given special attention. The work-hardening of the different material models was based on the behaviour of the idealized RVE with cubical martensite in the centre exposed to uniaxial tension. The effects of using initial void volume fraction and void nucleation was investigated. More flexibility was observed by using void nucleation in order to capture the rapid void growth experienced beyond load maximum in the idealized RVE and the single element. New simulations of central hole tests with the Gurson model included were conducted as the final step of the approach. An abrupt change was observed in the engineering stress-strain curves at the desired fracture strain. The Voce hardening parameters and the Gurson model parameters, which constitute the temporary material models for the DP steels after conducting the micro-macro approach, are listed in Table 7.1 and Table 7.3, respectively.

Table 7.3: The temporary Gurson model parameters for the homogeneous material model for each steel quality.

DP Steel	q_1 [-]	q_2 [-]	q_3 [-]	ε_N [-]	S_N [-]	f_N [-]
Docol 500DP	1.5	1.0	2.25	1.3	0.05	0.3
Docol 600DP	1.5	1.0	2.25	0.9	0.05	0.3
Docol 800DP	1.5	1.0	2.25	0.8	0.05	0.3
Docol 1000DP	1.5	1.0	2.25	0.6	0.05	0.3

The approach did not, however, accurately reproduce the stress level. It is addressed attention to Figure 7.2, where discrepancies were observed between the experimental test and numerical simulation in terms of the engineering stress-strain curve. Similar differences were also observed for the other steel qualities in Appendix A.5. It was speculated whether the differences occurred due to the work-hardening laws. They were based on the RVE with cubical martensite, which was an idealization of the actual microstructure. In order to show the dependency on the work-hardening law, new Voce hardening laws were calibrated based on the experimental data from the uniaxial tension tests up to necking. Figure 7.10 is similar to Figure 7.2, where the result from using the work-hardening law based on the uniaxial tension experiment is also included. Figure 7.11 to 7.13 are similar figures for the other steel qualities. Evidently, the numerical simulations with the Voce hardening laws based on the uniaxial tension experiments resembled the

central hole experiments to a greater extent. Thus, it is expected that better compliance between the experiment and the numerical simulation could be obtained if the RVEs resembled the DP steel microstructure to a greater extent. However, the work in this thesis is based on the idealized RVE, and to conduct the micro-macro approach with another RVE (for instance the one presented in Section 3.5.1) was considered as out of scope.

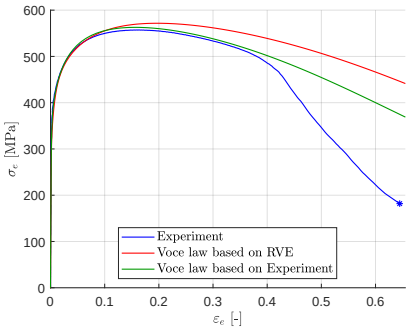

Figure 7.10: Docol 500DP: Engineering stress-strain curve from the CH simulations with different work-hardening laws.

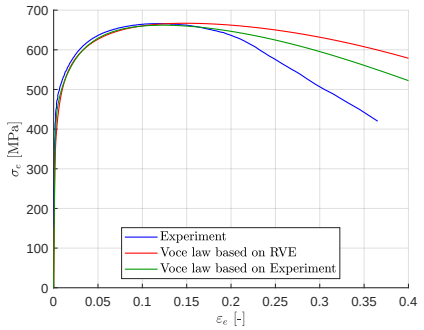

Figure 7.11: Docol 600DP: Engineering stress-strain curve from the CH simulations with different work-hardening laws.

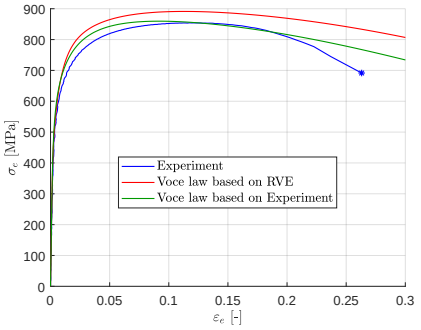

Figure 7.12: Docol 800DP: Engineering stress-strain curve from the CH simulations with different work-hardening laws.

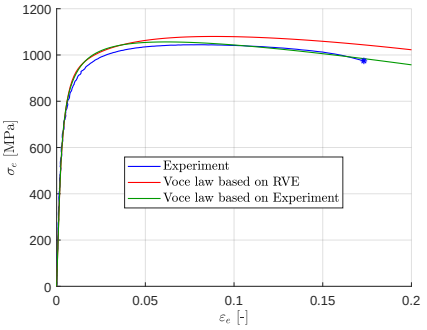

Figure 7.13: Docol 1000DP: Engineering stress-strain curve from the CH simulations with different work-hardening laws.

Even though the numerical simulations based on the uniaxial tension experiments improved the compliance with the experimental data, differences were still observed in Figure 7.10 to 7.13 beyond engineering strain of 0.4, 0.2, 0.2 and 0.15 for Docol 500DP, 600DP, 800DP and 1000DP, respectively. These differences may have been

caused by material softening due to crack initiation and propagation in the specimen. Thus, the material softening may have initiated earlier in the experiments than at the fracture strain used in this approach. Pictures from the experiments were investigated to confirm these speculations. Figure 7.14 and Figure 7.15 show the pictures from the DIC analysis of the experiments with Docol 500DP and 600DP, respectively. The pictures correspond to engineering strains of 0.4 and 0.2, and a crack is observed right below and above the hole, respectively. Thus, the material softening initiated earlier than at the fracture strain as assumed in the micro-macro approach. The approach could therefore be improved by considering the whole damage evolution, and not only the fracture strain. This could be done by lowering the expected plastic strain at nucleation, ε_N, such that void nucleation initiates at the strain corresponding to damage initiation in Figure 7.8.

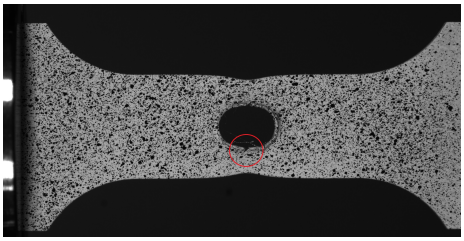

Figure 7.14: Docol 500DP: Picture from DIC analysis corresponding to 0.4 in engineering strain to show the crack initiation in the specimen. A crack is observable inside the red circle.

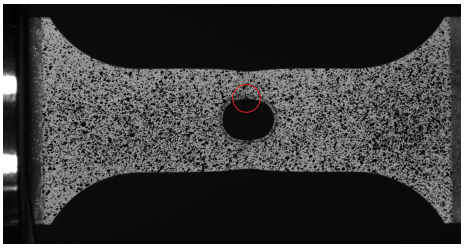

Figure 7.15: Docol 600DP: Picture from DIC analysis corresponding to 0.2 in engineering strain to show the crack initiation in the specimen. A crack is observable inside the red circle.

As seen in Figure 7.12 and Figure 7.13, the discrepancies between the experiment and numerical simulation become less prominent for Docol 800DP and 1000DP. The investigation of the pictures from the DIC analyses showed that the damage initiation and final fracture almost occurred simultaneously. In the case of Docol 800DP, only a small crack was observable in Figure 7.16 at the last frame before fracture. For Docol 1000DP, no crack prior to fracture was observed. Thus, it was not considered as important to calibrate damage initiation in Docol 800DP and 1000DP since the difference was small. In fact, an uncoupled damage criterion may be sufficient for Docol 800DP and 1000DP when time is of the essence.

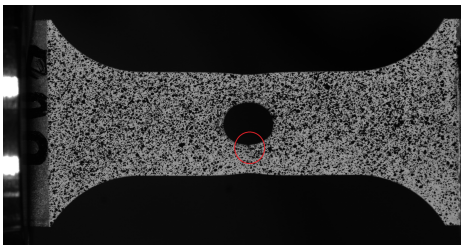

Figure 7.16: Docol 800DP: Picture from DIC analysis corresponding to 0.2 in engineering strain to show the crack initiation in the specimen. A crack is observable inside the red circle.

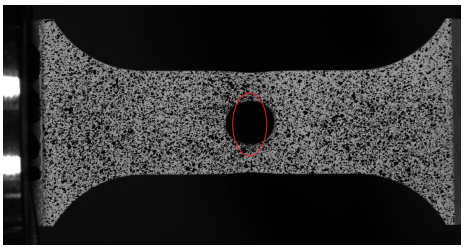

Figure 7.17: Docol 1000DP: Picture from DIC analysis corresponding to 0.15 in engineering strain to show the crack initiation in the specimen. No crack is observable inside the red circle.

The difference in damage evolution between the different steel qualities are primarily due to the strength and the martensite volume fraction of the DP steels. DP steels with high martensite volume fraction have high strength and low ductility compared to DP steels with low martensite volume fraction. How rapid the damage evolution is depends on the elastic strain energy released when a crack propagates. DP steels with high strength store more elastic energy than DP steels with low strength. Thus, more energy is released when a crack propagates in Docol 800DP and 1000DP compared to Docol 500DP and 600DP. Consequently, a larger stress redistribution and additional deformation of the uncracked material is caused, which leads to a more rapid crack propagation for Docol 800DP and 1000DP.

As stated above, the micro-macro approach could be improved by considering damage initiation instead of final fracture in the experiments. This improvement was done for Docol 500DP and 600DP as they exhibited considerable amount of damage evolution before fracture. Note, this was not done for Docol 800DP and 1000DP since the damage initiation and final fracture occurred almost simultaneously. This was done by repeating the two last steps of the approach. First, fracture was enforced in the single element at the critical element strain corresponding to damage initiation. Then, a final simulation of the central hole test was conducted with the new material model based on void nucleation.

For Docol 500DP, the calibrated parameters were $\varepsilon_N = 0.9$, $S_N = 0.05$ and $f_N = 0.3$. Figure 7.18 shows the true stress-strain curves from critical element

and the single element. The left and right red star marks the damage initiation and final fracture, respectively. The chosen void nucleation parameters give the desired rapid reduction of stress carrying capacity around damage initiation. The result of implementing the calibrated void nucleation parameters into the central hole simulation is shown in Figure 7.19. Similar results for Docol 600DP were obtained with $\varepsilon_N = 0.6$ and the figures are shown in Appendix A.5 in Figure A.5.67 and A.5.68.

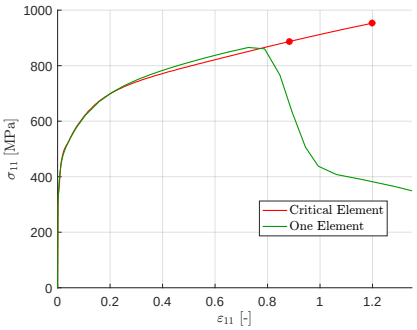

Figure 7.18: Docol 500DP: True stress-strain curves from the critical element and the homogeneous element with the void nucleation calibrated for damage initiation.

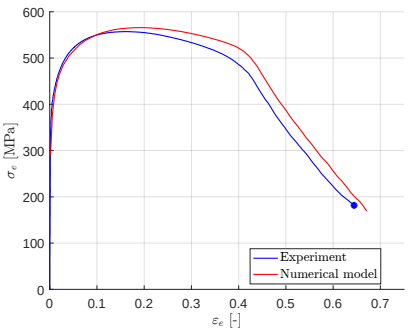

Figure 7.19: Docol 500DP: Engineering stress-strain curve from the central hole simulation based on damage initiation.

The improvement of the micro-macro approach provided satisfactory results for Docol 500DP and 600DP. The numerical simulations complied better with the experimental tests. Evidently, it is important to include the damage initiation when calibrating material models for Docol 500DP and 600DP, in contrast to Docol 800DP and 1000DP. Thus, the Voce hardening laws in Table 7.1 and the Gurson parameters in Table 7.4 constitute the proposed material models for the DP steels.

Table 7.4: The final Gurson parameters for the homogeneous material models.

DP Steel	q_1 [-]	q_2 [-]	q_3 [-]	ε_N [-]	S_N [-]	f_N [-]
Docol 500DP	1.5	1.0	2.25	0.9	0.05	0.3
Docol 600DP	1.5	1.0	2.25	0.6	0.05	0.3
Docol 800DP	1.5	1.0	2.25	0.8	0.05	0.3
Docol 1000DP	1.5	1.0	2.25	0.6	0.05	0.3

8 Conclusion

The main objective of this master project was to use micromechanical FE simulations to study the influence of martensite volume fraction and distribution on yielding, work-hardening and ductility. This was done by establishing a micromechanical FE modelling framework for plasticity and fracture of DP steels. In addition, cyclic load experiments were conducted in order to investigate the influence of martensite volume fraction on the Bauschinger effect. Finally, material models for DP steels applicable to large-scale FE simulations based on the experimental data and the micromechanical analyses were proposed. The four different DP steels considered in this study were Docol 500DP, 600DP, 800DP and 1000DP. The most important findings are presented in this chapter.

Cyclic load experiments were successfully conducted by use of an anti-buckling device for the four DP steels. The Bauschinger effect in the DP steels was evaluated by calculating a ratio between the stress at load reversal and the subsequent yield stress after load reversal, denoted as the r-ratio. The r-ratio increased with the DP steel quality, which indicated that the Bauschinger effect increased with the martensite volume fraction.

In this thesis, four different idealized RVEs were considered. The cubical RVEs were modelled as a ferrite matrix with martensite inclusions. The martensite was modelled with either cubical or spherical martensitic islands in the centre and each corner or only in the centre. For all steel qualities, the idealized RVE with a single cubical martensite island in the centre exhibited yielding and work-hardening closest to the uniaxial tension experimental data, and was considered as the micromechanical FE modelling framework. The other RVEs produced a too soft behaviour. This was studied through considering the energy in the different phases. It was found that the martensite was engaged to a greater extent in the RVEs with a single martensite cube and thus exhibited the strongest behaviour. The RVEs created were also compared to an RVE that was based on a realistic DP steel microstructure. Only small differences were observed between the idealized RVE with cubical martensite in centre and the RVE based on the realistic microstructure in terms

of the obtained stress-strain curves, but the latter RVE was more computationally demanding.

Further, the four idealized RVEs were used to create iso-curves for the yielding in the DP steels. For all steels, the RVE with cubical martensite in the centre showed the largest yield stress, and the yield stress decreased when the martensite was distributed in both the centre and the corners. The shape of the iso-curves resembled the Hershey yield locus with an exponent of $m = 6$. Furthermore, the iso-curves created herein resembled results obtained from an experimental study in the literature.

The Bauschinger effect was also considered in the RVEs in order to determine the contribution from the strength difference between the two phases. All RVEs displayed lower r-ratios than those found in the experiments. Evidently, it was not sufficient to consider only the martensite volume fraction and the ferrite-martensite strength difference to reproduce all of the Bauschinger effect in DP steels. The Bauschinger effect was also studied with varying martensite volume fraction. The Bauschinger effect increased with the martensite volume fraction until 60%. It then decayed as the volume fraction increased further.

The numerical study of ductile fracture of the DP steels was carried out by only using the RVE with cubical martensite in the centre. The study was limited to only consider uniaxial tension. The Gurson model was implemented into the ferrite material model where the initial void volume fraction and the porous failure criterion were used. It was found that the f_0, f_c and f_F parameters were important for the void evolution and consequently crucial for the ductility achieved in the RVE. Docol 500DP and 600DP displayed the decohesion of ferrite-martensite interface fracture mechanism, since stresses and strains localized at the interface. For Docol 800DP and 1000DP, decohesion of ferrite-martensite interface was not obtained as the stresses and strains were localized at the loaded surface. It was concluded that the Gurson model with f_0, f_c and f_F in the RVE was not sufficient in representing the failure mechanism when the martensite volume fraction increased as martensite particle cracking became important.

Lastly, material models were proposed for DP steels applicable to large-scale FE simulations based on the central hole test and the idealized RVE with cubical

martensite in the centre. This was done by conducting the micro-macro approach, where a homogeneous material model was obtained. The final material models were Gurson models, where the work-hardening was described by Voce hardening laws and damage was included through nucleation and growth of voids. Further, the approach revealed that considerable amount of damage evolution occurred in Docol 500DP and 600DP before final fracture, in contrast to Docol 800DP and 1000DP where damage initiation and final fracture almost occurred simultaneously. Thus, an uncoupled damage model may be sufficient for DP steels with high martensite volume fraction.

Future Work

This work was based on microstructure-based modelling and simulation to predict the behaviour of DP steels. However, the scope of this thesis was limited by the simplifications introduced in advance of this study. Furthermore, this thesis was limited by time, therefore additional investigation of the topics considered could be conducted. In this chapter further work that the authors of this study found interesting is suggested.

- It is important to consider the simplifications introduced. The micromechanical FE modelling framework for plasticity and fracture was based on the idealized RVEs, which was a simplification of the actual microstructure of DP steels. Some artificial effects were observed throughout the study regarding the incompatible deformation of the ferrite and martensite phase. It is recommended to use RVEs based on the actual microstructure of DP steels for further investigation of stress and strain localizations.

- Considerable attention was addressed to fracture and the Gurson model throughout this thesis. The study was limited to only consider stress states equal or close to uniaxial tension. An investigation of fracture in DP steels by use of the Gurson model in other stress states is suggested as further work. The influence of both high and low stress triaxialities should be investigated. Moreover, extensions of the Gurson model could be considered to compensate for the deficiencies of this model at low stress triaxialities. However, these extensions are not available in standard finite element software and additional subroutines need to be implemented.

- For simplicity, no calibration of the the q_i-parameters was conducted in this study and consequently, the standard values for metals were used. The authors are aware that the Gurson parameters are not unique and similar results may be obtained with different parameters. However, a calibration procedure for the Gurson parameters for DP steels is considered as beneficial.

- Different approaches could be investigated to capture the fracture mechanisms. A cohesive zone modelling approach could be used to model both

decohesion of the ferrite-martensite interface and martensite particle cracking. It is recommended that further investigation uses the approach based on cohesive elements in order to avoid convergence problems as described herein. Martensite particle cracking could also be modelled by using a brittle failure criterion available in standard finite element software.

- A further investigation of the micro-macro approach is appealing. For instance, it is recommended to include a failure criterion. This could be done by changing the approach in the following way: The porous failure criterion becomes available if Abaqus/Explicit is used instead of Abaqus/Standard. Then, the load could be applied as boundary conditions instead of surface tractions to traverse the limit points in the force-displacement curves of the RVE and the single element. The boundary conditions correspond to the deformation of the critical element. In addition, a void nucleation burst approach where the nucleation of voids depends on the stress state could be considered in further studies.

- The calibrated material models should be verified in other stress states. It is recommended to do the verification before the material models are used in simulations of structural components.

References

ABAQUS (2019). Abaqus 6.14 Documentation, Dassault Systèmes Simulia Corp. Providence Roas, Rhode Island.
URL: *http://ivt-abaqusdoc.ivt.ntnu.no:2080/texis/search/?query=wetting&submit.x=0&submit.y=0&group=bk&CDB=v6.14*

Abid, N. H., Al-Rub, R. K. A. & Palazotto, A. N. (2017), 'Micromechanical finite element analysis of the effects of martensite morphology on the overall mechanical behaviour of dual phase steel', *International Journal of Solids and Structures* **104-105**, 8–24.
URL: *http://dx.doi.org/10.1016/j.ijsolstr.2016.11.005*

Adamczyk, J. & Grajcar, A. (2007), 'Heat treatment and mechanical properties of low-carbon steel with dual-phase microstructure', *Journal of Achievements in Materials and Manufacturing Engineering* **22**(1), 13–20.

Ahmad, E., Manzoor, T., Ali, K. & Akhter, J. (2000), 'Effect of microvoid formation on the tensile properties of dual-phase steel', *Journal Of Materials Engineering And Performance* **9**(3), 306–310.
URL: *https://doi.org/10.1361/105994900770345962*

Amirmaleki, M., Samei, J., Green, D. E., van Riemsdijk, I. & Stewart, L. (2016), '3D micromechanical modeling of dual phase steels using the representative volume element method', *Mechanics of Materials* **101**(1), 27–39.
URL: *http://dx.doi.org/10.1016/j.mechmat.2016.07.011*

Anbarlooie, B., Kadkhodapour, J., Toudeshky, H. H. & Schmauder, S. (2018), Miromechanics of Dual-Phase Steels: Deformation, Damage, and Fatigue, *in* C. H. et al., ed., 'Handbook of Mechanics of Materials', Springer, Singapore.
URL: *https://doi.org/10.1007/978-981-10-6855-3_70-1*

Bag, A., Ray, K. & Dwarakadasa, E. (1999), 'Influence of Martensite Content and Morphology on Tensile and Impact Properties of High-Martensite Dual-Phase Steels', *Metallurgical And Materials Transactions A* **30A**, 1193–1201.
URL: *https://doi.org/10.1007/s11661-999-0269-4*

Bell, K. (2013), *An engineering approach to FINITE ELEMENT ANALYSIS of linear structural mechanics problems*, Fagbokforlaget Vigmostad & Bjørke AS, Kanalveien 51.

Bergström, Y. (1970), 'A dislocation model for the stress-strain behaviour of polycrystalline α-Fe with special emphasis on the variation of the densities of mobile and immobile dislocations', *Materials Science and Engineering* **5**(4), 193–200.
URL: *https://doi.org/10.1016/0025-5416(70)90081-9*

Buessler, P. (1999), 'Ecsc steel rtd first report'.

Byun, T. S. & Kim, I. S. (1993), 'Tensile properties and inhomogeneous deformation of ferrite-martensite dual-phase steels', *Journal of materials science* **28**(1), 2923–2932.

Chang, K.-H. (2015), *Chapter 18 - Structural Design Sensitivity Analysis*, Academic Press, pp. 1001–1103.
URL: *https://doi.org/10.1016/B978-0-12-382038-9.00018-1*

Chen, Z., Gandhi, U., Lee, J. & Wagoner, R. (2016), 'Variation and consistency of Young's modulus in steel', *Journal of Materials Processing Technology* **227**(1), 227–243.
URL: *https://doi.org/10.1016/j.jmatprotec.2015.08.024*

Chu, C. C. & Needleman, A. (1980), 'Void nucleation effects in biaxially stretched sheets.', *Journal of Engineering Materials and Technology* **102**(3), 249–256.

Concepcion, V. L., Lorusso, H. N. & G.Svoboda, H. (2015), 'Effect of carbon content on microstructure and mechanical properties of dual phase steels', *Procedia Materials Science* **8**(1), 1047–1056.
URL: *https://doi.org/10.1016/j.mspro.2015.04.167*

Cornec, A., Scheider, I. & Schwalbe, K.-H. (2003), 'On the practical application of the cohesive model', *Engineering Fracture Mechanics* **70**(1), 1963–1987.
URL: *http://doi.org/10.1016/S0013-7944(03)00134-6*

Dalloz, A., J.Besson, Gourgues-Lorenzon, A. F., Sturel, T. & Pineau, A. (2009), 'Effect of shear cutting on ductility of a dual phase steel.', *Engineering Fracture Mechanics* **76**(10), 1411–1424.
URL: *https://doi.org/10.1016/j.engfracmech.2008.10.009*

REFERENCES

Dassault Systèmes (2014), *Abaqus 6.14 Online Documentation - Abaqus Anlaysis User's Guide*. Section 28.1.1 Solid (continuum) elements, Accessed on: Mar. 02, 2020.

Davies, R. (1978), 'Influence of martensite composition and content on the properties of dual phase steels', *Metallurgical Transactions A* **9**(5), 671–679.

Dunand, M. & Mohr, D. (2014), 'Effect of Lode parameter on plastic flow localization after proportional loading at low stress triaxialities', *Journal of the Mechanics and Physics of Solids* **66**(1), 133–153.
URL: *https://doi.org/10.1016/j.jmps.2014.01.008*

Erdogan, M. & Priestner, R. (2002), 'Effect of martensite content, its dispersion, and epitaxial ferrite content on Bauschinger behaviour of dual phase steel', *Materials Science and Technology* **18**(4), 369–376.
URL: *https://doi.org/10.1179/026708302225001679*

Fagerholt, E. (2019), 'Software dic - ecorr', `http://folk.ntnu.no/egilf/ecorr/doc/`. [Online; Accessed 13.03.2020].

Fagerholt, E., Børvik, T. & Hopperstad, O. S. (2013), 'Measuring discontinuous displacement fields in cracked specimens using digital image correlation with mesh adaptation and crack-path optimization', *Optics and Lasers in Engineering* **51**(3), 299–310.
URL: *https://doi.org/10.1016/j.optlaseng.2012.09.010*

Faleskog, J., Gao, X. & Shih, C. F. (1998), 'Cell model for nonlinear fracture analysis – I. Micromechanics calibration', *International Journal of Fracture* **89**(1), 355–373.

Fonstein, N. (2015), *Advanced High Strength Sheet Steels - Physical Metallurgy, Design, Processing and Properties*, Springer International Publishing, Springer Cham Heidelberg New York Dordrecht London.
URL: *https://doi.org/10.1007/978-3-319-19165-2*

Garrison, W. & Moody, N. (1987), 'Ductile Fracture', *J. Phys. Chem. Solids* **48**(11), 1035–1074.

Gologanu, M., Leblond, J.-B. & Devaux, J. (1993), 'Approximate models for ductile metals containing non-spherical voids—Case of axisymmetric prolate ellipsoidal

cavities.', *Journal of the Mechanics and Physics of Solids* **41**(11), 1723–1754.
URL: *https://doi.org/10.1016/0022-5096(93)90029-F*

Gruben, G., Vysochinskiy, D., Coudert, T., Reyes, A. & Lademo, O. (2013), 'Determination of Ductile Fracture Parameters of a Dual-Phase Steel by Optical Measurements', *An International Journal for Experimental Mechanics* **49**(1), 221–232.
URL: *https://doi.org/10.1111/str.12030*

Gurson, A. L. (1977), 'Continuum Theory of Ductile Rupture by Void Nucleation and Growth: Part I - Yield Criteria and Flow Rules for Porous Ductile Media', *Journal of Engineering Materials and Technology* **99**(1), 2–15.

Hancock, J. W. & Mackenzie, A. C. (1976), 'On the mechanisms of ductile failure in high-strength steels subjected to multi-axial stress-states', *Journal of the Mechanics and Physics of Solids* **24**(2-3), 147–160.
URL: *https://doi.org/10.1016/0022-5096(76)90024-7*

Hershey, A. V. (1954), 'The plasticity of an isotropic aggregate of anisotropic face centered cubic crystals', *Journal of Applied Mechanics* **21**(3), 241–249.

Hopperstad, O. S. & Børvik, T. (2017), *Material mechanics - Part 1*, NTNU.

Hopperstad, O. S., Børvik, T., Langseth, M., Labibes, K. & Albertini, C. (2003), 'On the influence of stress triaxiality and strain rate on the behaviour of a structural steel. Part I. Experiments', *European Journal of Mechanics - A/Solids* **22**(1), 1–13.
URL: *https://doi.org/10.1016/S0997-7538(02)00006-2*

Hosford, W. F. (1972), 'A generalized isotropic yield criterion', *Journal of Applied Mechanics* **39**(4), 607–609.

Hou, Y., Min, J., Guo, N., Lin, J., Carsley, J. E., Stoughton, T. B., Traphöner, H., Clausmeyer, T. & Tekkaya, A. E. (2019), 'Investigation of evolving yield surfaces of dual-phase steels', *Journal of Materials Processing Tech.* pp. –.
URL: *https://doi.org/10.1016/j.jmatprotec.2019.116314*

Jiang, Z., Guan, Z. & Lian, J. (1995), 'Effects of microstructural variables on the deformation behaviour of dual-phase steel', *Materials Science and Engineering A* **190**(1), 55–64.

Kadkhodapour, J., Schmauder, S., Raabe, D., Ziaei-Rad, S., Weber, U. & Calcagnotto, M. (2011), 'Experimental and numerical study on geometrically necessary dislocations and non-homogeneous mechanical properties of the ferrite phase in dual phase steels', *Acta Materialia* **59**(1), 4387–4394.
URL: *https://doi.org/10.1016/j.actamat.2011.03.062*

Kocks, U. & Mecking, H. (2003), 'Physics and phenomenology of strain hardening: the FCC case', *Progress in Materials Science* **48**(1), 171–273.

Kouznetsova, V. (2002), Computational homogenization for the multi-scale analysis of multi-phase materials, PhD thesis, Department of Mechanical Engineering, Technische Universiteit Eindhoven.
URL: *https://doi.org/10.6100/IR560009*

Landron, C. (2011), Ductile damage characterization in Dual-Phase steels using X-ray tomography, PhD thesis, INSA de Lyon.
URL: *https://tel.archives-ouvertes.fr/tel-00738820*

Leslie, W. C. (1981), *The physical metallurgy of steels*, Hemisphere Publishing Corp., Hemisphere Publishing Corp.

Madou, K. & Leblond, J. B. (2012), 'A Gurson-type criterion for porous ductile solids containing arbitrary ellipsoidal voids-I: Limit-analysis of some representative cell.', *Journal of the Mechanics and Physics of Solids* **60**(5), 1020–1036.
URL: *https://doi.org/10.1016/j.jmps.2011.11.008*

Marcadet, S. J. & Mohr, D. (2015), 'Effect of compression-tension loading reversal on the strain to fracture of dual phase steel sheets', *Elsevier* **72**(1), 21–43.
URL: *http://dx.doi.org/10.1016/j.ijplas.2015.05.002*

MathWorks (2020), 'Matlab', `https://se.mathworks.com/products/matlab.html`. [Online; Accessed 13.03.2020].

Mazinani, M. & Poole, W. (2007), 'Effect of Martensite Plasticity on the Deformation Behavior of a Low-Carbon Dual-Phase Steel', *Metallurgical and Materials Transactions A* **38**, 328–339.
URL: *https://doi.org/10.1007/s11661-006-9023-3*

Milligan, R. V., Koo, W. H. & Davidson, T. E. (1966), 'The Bauschinger Effect in a High-Strength Steel', *Journal of Fluids Engineering, Transactions of the ASME*

88(2), 480–488.
URL: *https://doi.org/10.1115/1.3645883*

Mori, T. & Tanaka, K. (1973), 'Average stress in matrix and average elastic energy of materials with misfitting inclusions', *Acta Metallurgica* **21**(5), 571–574.
URL: *https://doi.org/10.1016/0001-6160(73)90064-3*

Nygårds, M. & Gudmundson, P. (2002), 'Micromechanical modeling of ferritc/pearlitic steels', *Material Science and Engineering: A* **325**(1-2), 435–443.
URL: *https://doi.org/10.1016/S0921-5093(01)01509-X*

Paul, S. K. (2013), 'Real microstructure based micromechanical model to simulate microstructural level deformation behavior and failure initiation in DP 590 steel', *Materials & Design* **44**(1), 397–406.

Peng-Heng, C. & Preban, A. (1985), 'The effect of ferrite grain size and martensite volume fraction on the tensile properties of dual phase steel', *Acta Metallurgica* **33**(5), 897–903.
URL: *https://doi.org/10.1016/0001-6160(85)90114-2*

Petit, T., Besson, J., Ritter, C., Colas, K., Helfen, L. & Morgeneyer, T. F. (2019), 'Effect of hardening on toughness captured by stress-based damage nucleation in 6061 aluminum alloy.', *Acta Materialia* **180**, 349–365.
URL: *https://doi.org/10.1016/j.actamat.2019.08.055*

Pierman, A.-P., Bouaziz, O., Pardoen, T., Jacques, P. & Brassart, L. (2014), 'The influence of microstructure and composition on the plastic behaviour of dual-phase steels', *Acta Materialia* **73**(1), 298–311.
URL: *https://doi.org/10.1016/j.actamat.2014.04.015*

Ramazani, A., Mukherjee, K., Prahl, U. & Bleck, W. (2012), 'Modelling the effect of microstructural banding on the flow curve of dual-phase (DP) steels', *Computational Materials Science* **52**(1), 46–54.
URL: *https://doi.org/10.1016/j.commatsci.2011.05.041*

Ramazani, A., Mukherjee, K., Quade, H., Prahl, U. & Bleck, W. (2013), 'Correlation between 2D and 3D flow curve modelling of DP steels using a microstructure-based RVE approach', *Materials Science and Engineering: A* **560**(1), 129–139.
URL: *https://doi.org/10.1016/j.msea.2012.09.046*

Ramazani, A., Schwedt, A., Aretz, A., Prahl, U. & Bleck, W. (2013), 'Characterization and modelling of failure initiation in DP steel', *Computational Materials Science* **75**(1), 35–44.
URL: *https://doi.org/10.1016/j.commatsci.2013.04.001*

Rodriguez, R.-M. & Gutiérrez, I. (2003), Unified formulation to predict the tensile curves of steels with different microstructures, *in* 'THERMEC'2003', Vol. 426 of *Materials Science Forum*, Trans Tech Publications Ltd, pp. 4525–4530.

Saai, A. (2019), 'Casa-mm5: Microstructure based finite element modelling of dp steels and martensitic steels'. Centre for Advanced Structural Analysis (CASA), NTNU. Research Programme: Metallic materials.

Santos, R. O., Silveira, L. B., Moreira, L. P., Cardoso, M. C., Silva, F. R. F., dos Santos Paula, A. & Albertacci, D. A. (2019), 'Damage identification parameters of dual-phase 600–800 steels based on experimental void analysis and finite element simulations.', *Journal of Materials Research and Technology* **8**(1), 644–659.
URL: *https://doi.org/10.1016/j.jmrt.2018.04.017*

SIMLab (2020), 'Structural impact laboratory', `https://www.ntnu.no/kt/simlab`. [Online; Accessed 28.05.2020].

Sirinakorn, T. & Uthaisangsuk, V. (2018), 'Investigation of damage initiation in high-strength dual-phase steels using cohesive zone model', *International Journal of Damage Mechanics* **27**(3), 409–438.
URL: *https://doi.org/10.1177/1056789516679718*

Speich, G., Miller, R. L., Kot, R. A. & Morris, J. W. (1979), *Structure and properties of dual phase steels*, 1 edn, The Metallurgical Society of AIME, Warrendale, Pa.

Sun, X., Choi, K. S., Liu, W. N. & Khaleel, M. A. (2009), 'Predicting failure modes and ductility of dual phase steels using plastic strain localization', *International Journal of Plasticity* **25**(1), 1888–1909.
URL: *https://doi.org/10.1016/j.ijplas.2008.12.012*

Tasan, C., Diehl, M., Yan, D., Bechtold, M., Roters, F., Schemmann, L., Zheng, C., Peranio, N., Ponge, D., Koyama, M., Tsuzaki, K. & Raabe1, D. (2015), 'An Overview of Dual-Phase Steels: Advances in Microstructure-Oriented Processing and Micromechanically Guided Design', *Annual Review of Materials Research*

75(1), 391–431.
URL: *https://doi.org/10.1146/annurev-matsci-070214-021103*

Thomser, C., Uthaisangsuk, V. & Bleck, W. (2009), 'Influence of Martensite Distribution on the Mechanical Properties of Dual Phase Steels: Experiments and Simulation', *Steel research international* **80**(88), 582–587.
URL: *https://onlinelibrary.wiley.com/doi/abs/10.2374/SRI09SP046?sid=vendor%3Adatabase*

Toda, H., Takijiri, A., Azuma, M., Yabu, S., Hayashi, K., Seo, D., Kobayashi, M., Hirayama, K., Takeuchi, A. & Uesugi, K. (2017), 'Damage micromechanisms in dual-phase steel investigated with combined phase- and absorption-contrast tomography', *Acta Materiaila* **126**(1), 401–412.
URL: *http://dx.doi.org/10.1016/j.actamat.2017.01.010*

Tvergaard, V. (1981), 'Influence of voids on shear band instabilities under plane strain conditions.', *International Journal of Fracture* **17**(4), 389–407.

Tvergaard, V. (1982), 'On localization in ductile materials containing spherical voids.', *International Journal of Fracture* **18**, 237–252.

Uthaisangsuk, V., Prahl, U. & Bleck, W. (2009), 'Failure modeling of multiphase steels using representative volume elements based on real microstructures', *Procedia Engineering* **1**(1), 171–176.
URL: *https://doi.org/10.1016/j.proeng.2009.06.040*

Uthaisangsuk, V., Prahl, U. & Bleck, W. (2011), 'Modelling of damage and failure in multiphase high strength DP and TRIP steels', *Engineering Fracture Mechanics* **78**(3), 469–486.
URL: *https://doi.org/10.1016/j.engfracmech.2010.08.017*

West, O., Lian, J., Münstermann, S. & Bleck, W. (2012), 'Numerical Determination of the Damage Parameters of a Dual-phase Sheet Steel.', *ISIJ International* **52**(4), 743–752.

Yoshida, F., Uemori, T. & Fujiwara, K. (2002), 'Elastic–plastic behavior of steel sheets under in-plane cyclic tension–compression at large strain', *International Journal of Plasticity* **18**(5-6), 633–659.
URL: *https://doi.org/10.1016/S0749-6419(01)00049-3*

A Simulations

A.1 Representative Volume Elements

Figure A.1.1: Docol 500DP: Illustration of the RVEs with cubical martensite. Martensite only in the centre to the left, while it is distributed both in the centre and the corners to the right. The blue and red parts represent the martensite and ferrite, respectively.

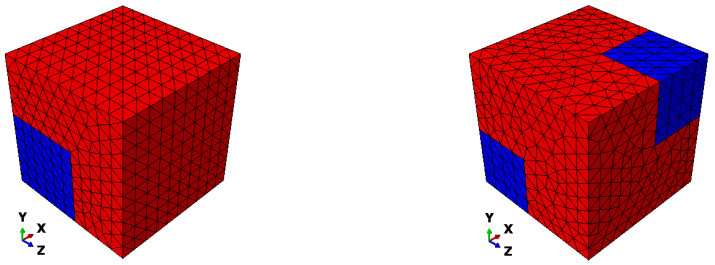

Figure A.1.2: Docol 600DP: Illustration of the RVEs with cubical martensite. Martensite only in the centre to the left, while it is distributed both in the centre and the corners to the right. The blue and red parts represent the martensite and ferrite, respectively.

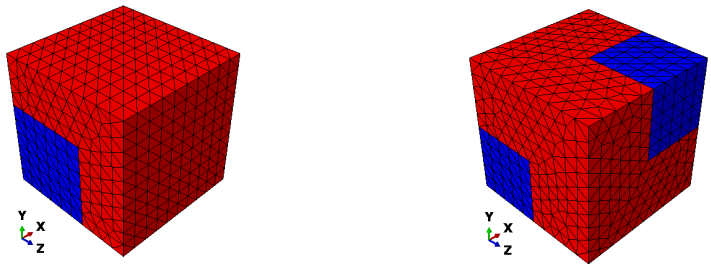

Figure A.1.3: Docol 800DP: Illustration of the RVEs with cubical martensite. Martensite only in the centre to the left, while it is distributed both in the centre and the corners to the right. The blue and red parts represent the martensite and ferrite, respectively.

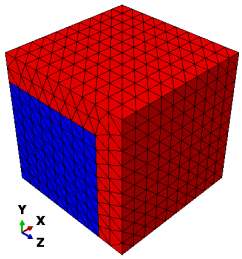

Figure A.1.4: Docol 1000DP: Illustration of the RVE with cubical martensite. Only the RVE with martensite in the centre is presented. The combination of cubical martensite, Docol 1000DP and distributed martensite causes overlapping of the martensite islands. The blue and red parts represent the martensite and ferrite, respectively.

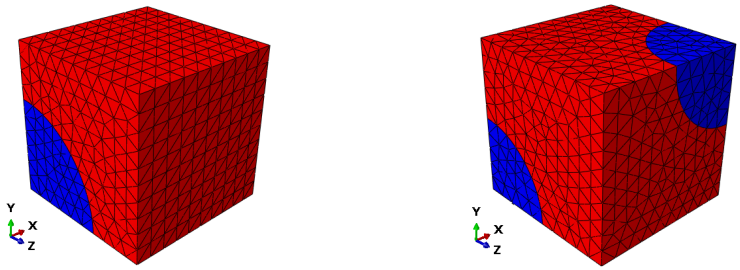

Figure A.1.5: Docol 500DP: Illustration of the RVEs with spherical martensite. Martensite only in the centre to the left, while it is distributed both in the centre and the corners to the right. The blue and red parts represent the martensite and ferrite, respectively.

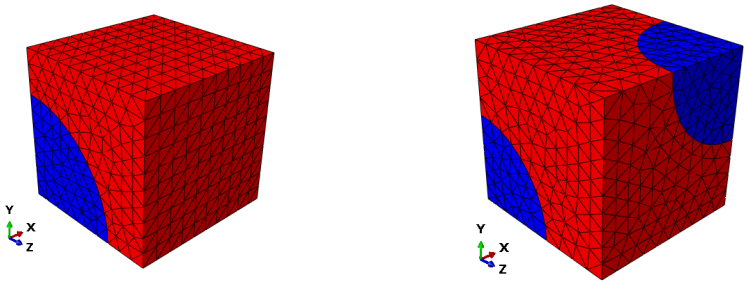

Figure A.1.6: Docol 600DP: Illustration of the RVEs with spherical martensite. Martensite only in the centre to the left, while it is distributed both in the centre and the corners to the right. The blue and red parts represent the martensite and ferrite, respectively.

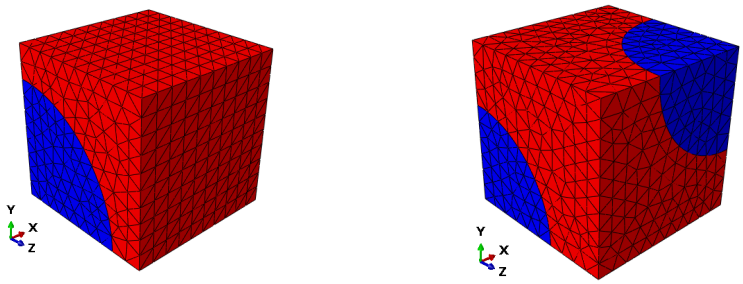

Figure A.1.7: Docol 800DP: Illustration of the RVEs with spherical martensite. Martensite only in the centre to the left, while it is distributed both in the centre and the corners to the right. The blue and red parts represent the martensite and ferrite, respectively.

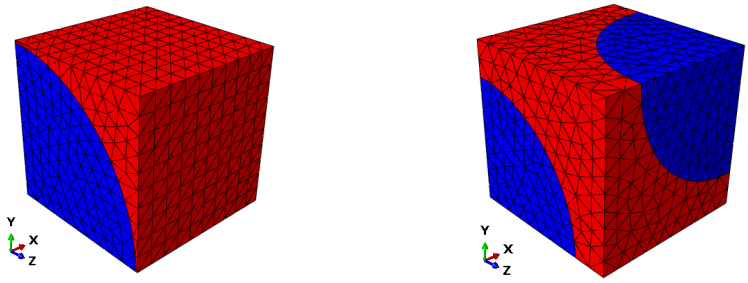

Figure A.1.8: Docol 1000DP: Illustration of the RVEs with spherical martensite. Martensite only in the centre to the left, while it is distributed both in the centre and the corners to the right. The blue and red parts represent the martensite and ferrite, respectively.

A.2 Yielding and Work-Hardening

The RVEs with cubical martensite:

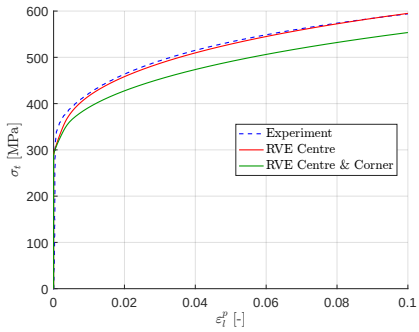

Figure A.2.9: Docol 500DP: Comparison of experiment and both RVEs with cubical shape of martensite in uniaxial tension.

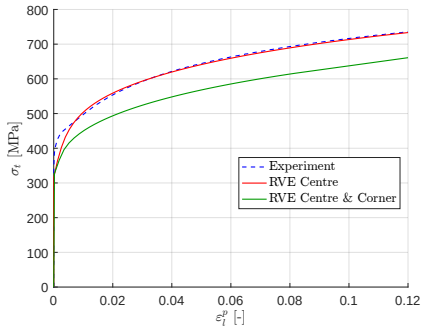

Figure A.2.10: Docol 600DP: Comparison of experiment and both RVEs with cubical shape of martensite in uniaxial tension.

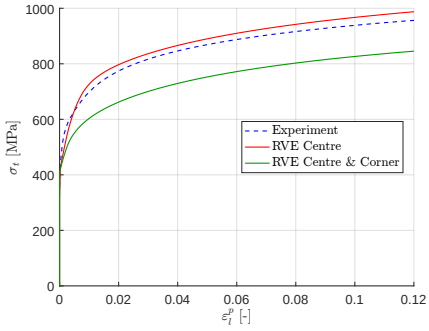

Figure A.2.11: Docol 800DP: Comparison of experiment and both RVEs with cubical shape of martensite in uniaxial tension.

The RVEs with spherical martensite:

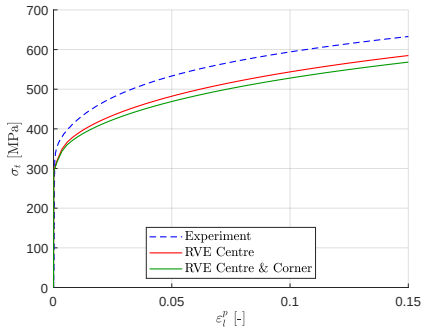

Figure A.2.12: Docol 500DP: Comparison of experiment and both RVEs with spherical shape of martensite in uniaxial tension.

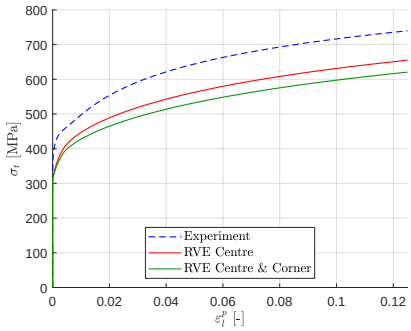

Figure A.2.13: Docol 600DP: Comparison of experiment and both RVEs with spherical shape of martensite in uniaxial tension.

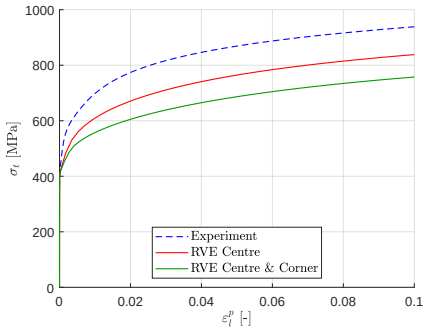

Figure A.2.14: Docol 800DP: Comparison of experiment and both RVEs with spherical shape of martensite in uniaxial tension.

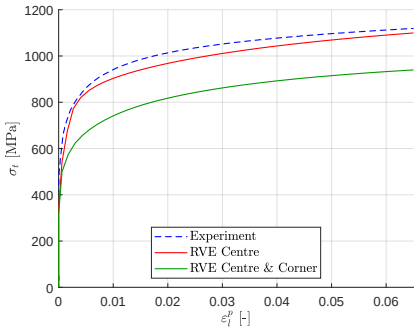

Figure A.2.15: Docol 1000DP: Comparison of experiment and both RVEs with spherical shape of martensite in uniaxial tension.

A.3 Iso-Curves

The RVE with cubical martensite in the centre:

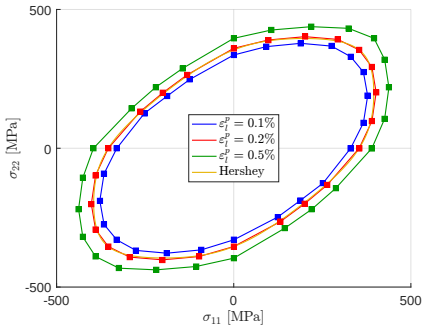

Figure A.3.16: Docol 500DP: Three iso-curves obtained by use of the RVE with cubical martensite in the centre and the Hershey yield locus at 0.2% plastic strain.

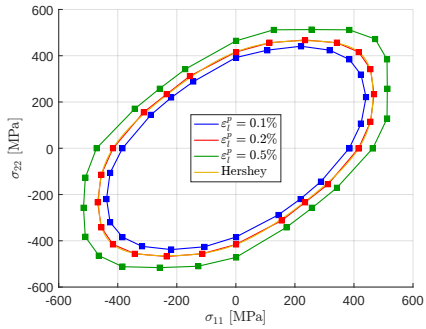

Figure A.3.17: Docol 600DP: Three iso-curves obtained by use of the RVE with cubical martensite in the centre and the Hershey yield locus at 0.2% plastic strain.

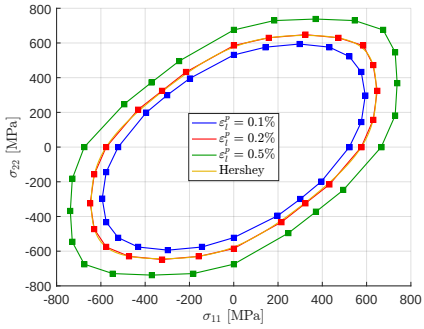

Figure A.3.18: Docol 800DP: Three iso-curves obtained by use of the RVE with cubical martensite in the centre and the Hershey yield locus at 0.2% plastic strain.

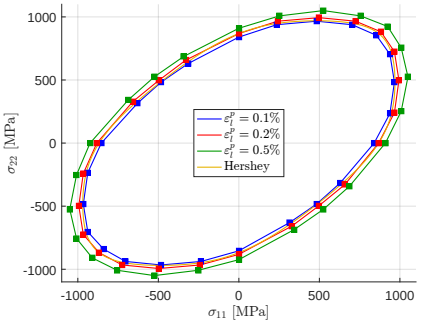

Figure A.3.19: Docol 1000DP: Three iso-curves obtained by use of the RVE with cubical martensite in the centre and the Hershey yield locus at 0.2% plastic strain.

The RVEs with cubical and spherical centre:

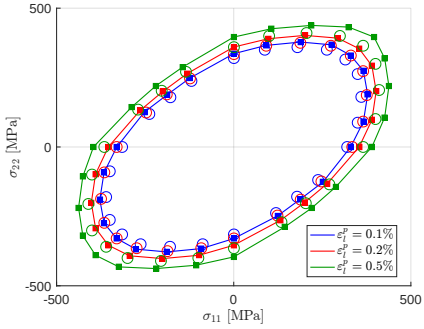

Figure A.3.20: Docol 500DP: Iso-curves obtained by use of the RVEs with cubical and spherical martensite in the centre.

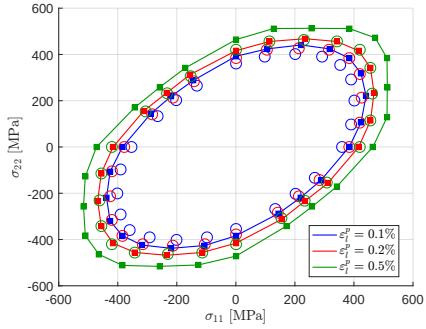

Figure A.3.21: Docol 600DP: Iso-curves obtained by use of the RVEs with cubical and spherical martensite in the centre.

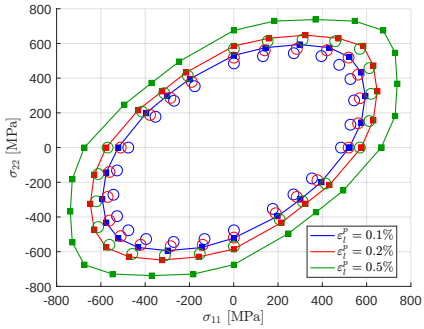

Figure A.3.22: Docol 800DP: Iso-curves obtained by use of the RVEs with cubical and spherical martensite in the centre.

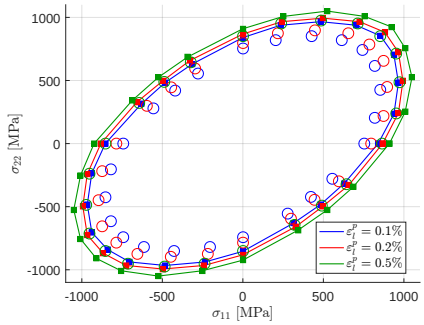

Figure A.3.23: Docol 1000DP: Iso-curves obtained by use of the RVEs with cubical and spherical martensite in the centre.

The effect of distributing the martensite:

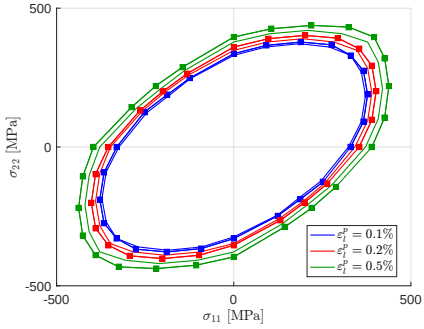

Figure A.3.24: Docol 500DP: Iso-curves obtained by using the RVEs with cubical martensite only in the centre and distributed between the centre and the corners.

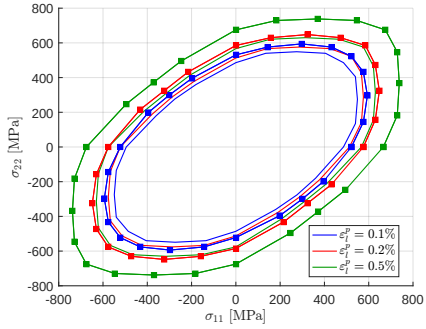

Figure A.3.25: Docol 800DP: Iso-curves obtained by using the RVEs with cubical martensite only in the centre and distributed between the centre and the corners.

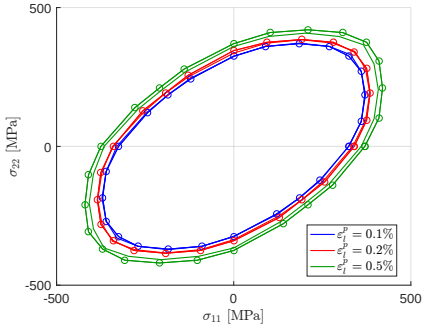

Figure A.3.26: Docol 500DP: Iso-curves obtained by using the RVEs with spherical martensite only in the centre and distributed between the centre and the corners.

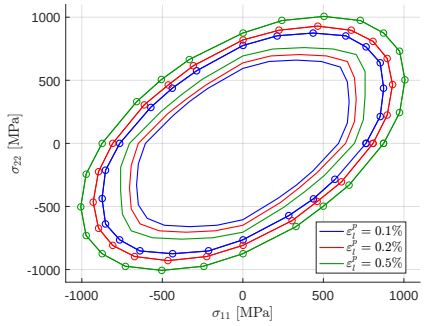

Figure A.3.27: Docol 1000DP: Iso-curves obtained by using the RVEs with spherical martensite only in the centre and distributed between the centre and the corners.

A.4 Kinematic Hardening

The RVE with cubical martensite in the centre:

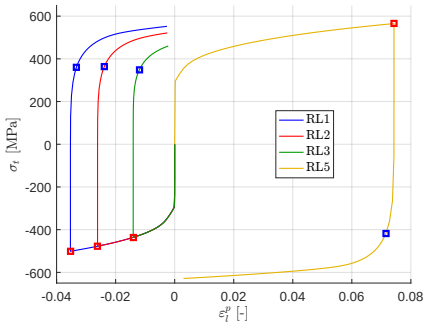

Figure A.4.28: Docol 500DP: True stress vs. plastic strain curves from the RVE with cubical martensite in the centre. Red and blue points indicate load reversal points and yield points, respectively.

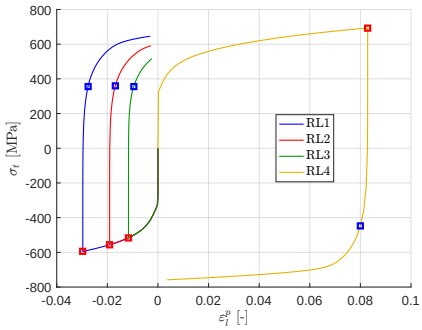

Figure A.4.29: Docol 600DP: True stress vs. plastic strain curves from the RVE with cubical martensite in the centre. Red and blue points indicate load reversal points and yield points, respectively.

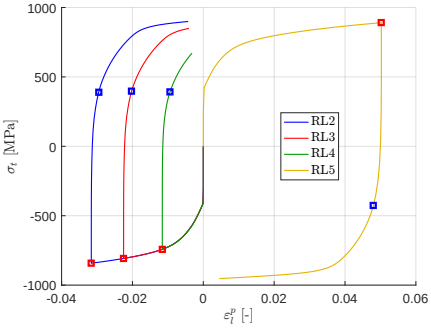

Figure A.4.30: Docol 800DP: True stress vs. plastic strain curves from the RVE with cubical martensite in the centre. Red and blue points indicate load reversal points and yield points, respectively.

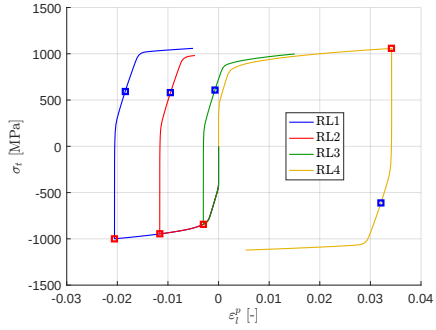

Figure A.4.31: Docol 1000DP: True stress vs. plastic strain curves from the RVE with cubical martensite in the centre. Red and blue points indicate load reversal points and yield points, respectively.

The RVE with cubical martensite in the centre and the corners:

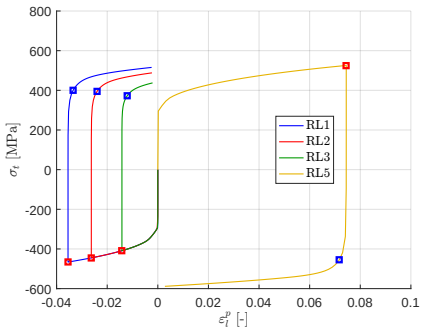

Figure A.4.32: Docol 500DP: True stress vs. plastic strain curves from the RVE with cubical martensite in the centre and the corners. Red and blue points indicate load reversal points and yield points, respectively.

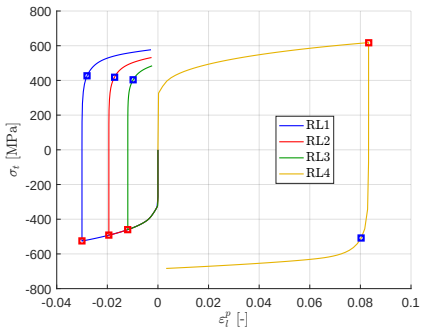

Figure A.4.33: Docol 600DP: True stress vs. plastic strain curves from the RVE with cubical martensite in the centre and the corners. Red and blue points indicate load reversal points and yield points, respectively.

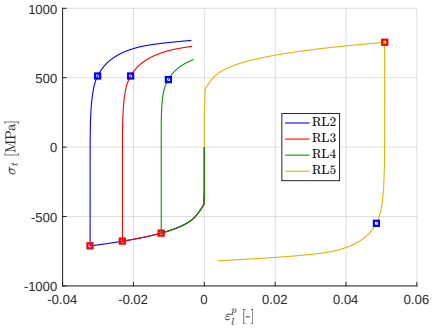

Figure A.4.34: Docol 800DP: True stress vs. plastic strain curves from the RVE with cubical martensite in the centre and the corners. Red and blue points indicate load reversal points and yield points, respectively.

The RVE with spherical martensite in the centre:

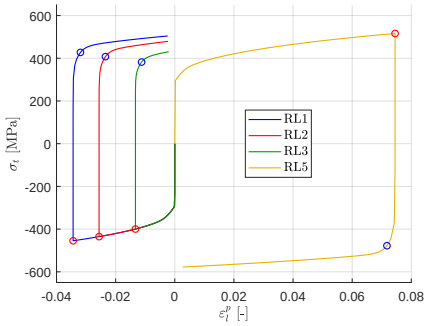

Figure A.4.35: Docol 500DP: True stress vs. plastic strain curves from the RVE with spherical martensite in the centre. Red and blue points indicate load reversal points and yield points, respectively.

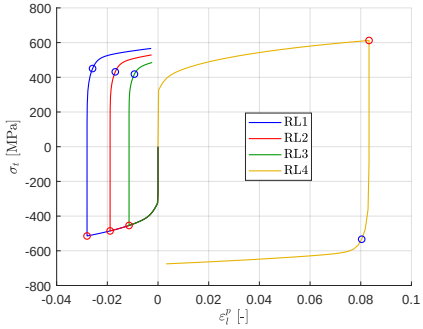

Figure A.4.36: Docol 600DP: True stress vs. plastic strain curves from the RVE with spherical martensite in the centre. Red and blue points indicate load reversal points and yield points, respectively.

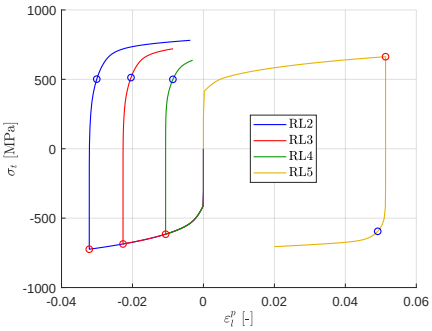

Figure A.4.37: Docol 800DP: True stress vs. plastic strain curves from the RVE with spherical martensite in the centre. Red and blue points indicate load reversal points and yield points, respectively.

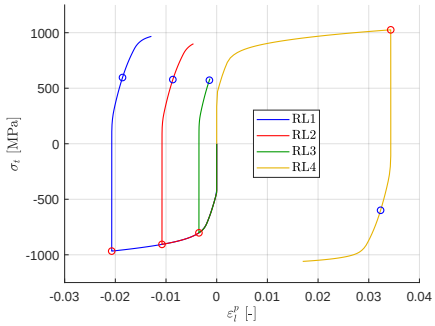

Figure A.4.38: Docol 1000DP: True stress vs. plastic strain curves from the RVE with spherical martensite in the centre. Red and blue points indicate load reversal points and yield points, respectively.

The RVE with spherical martensite in the centre and the corners:

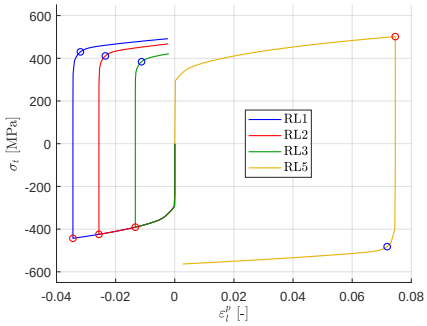

Figure A.4.39: Docol 500DP: True stress vs. plastic strain curves from the RVE with spherical martensite in the centre and the corners. Red and blue points indicate load reversal points and yield points, respectively.

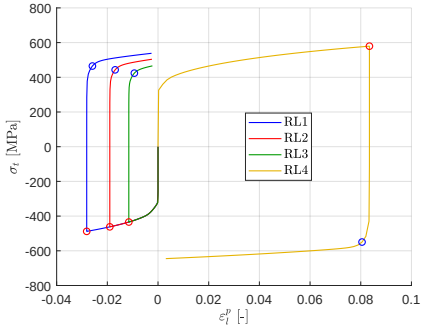

Figure A.4.40: Docol 600DP: True stress vs. plastic strain curves from the RVE with spherical martensite in the centre and the corners. Red and blue points indicate load reversal points and yield points, respectively.

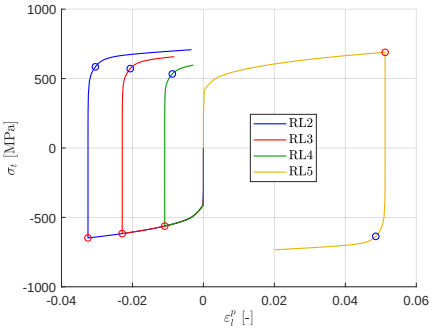

Figure A.4.41: Docol 800DP: True stress vs. plastic strain curves from the RVE with spherical martensite in the centre and the corners. Red and blue points indicate load reversal points and yield points, respectively.

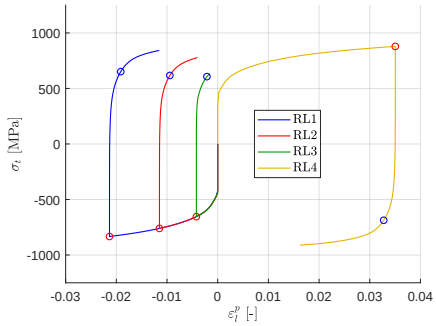

Figure A.4.42: Docol 1000DP: True stress vs. plastic strain curves from the RVE with spherical martensite in the centre and the corners. Red and blue points indicate load reversal points and yield points, respectively.

The RVEs with cubical martensite:

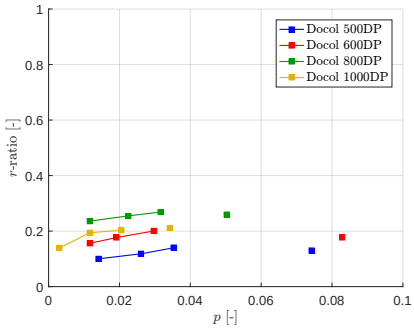

Figure A.4.43: The Bauschinger effect expressed by use of the r-ratio obtained by the RVE with cubical martensite in the centre.

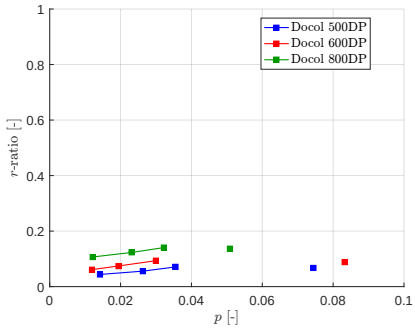

Figure A.4.44: The Bauschinger effect expressed by use of the r-ratio obtained by the RVE with cubical martensite in the centre and corners.

The RVEs with spherical martensite:

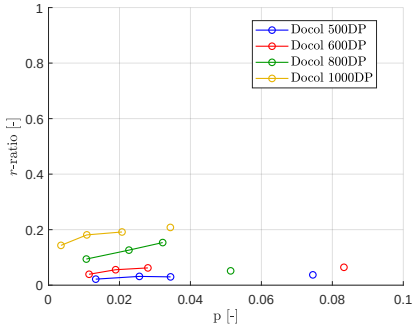

Figure A.4.45: The Bauschinger effect expressed by use of the r-ratio obtained by the RVE with spherical martensite in the centre.

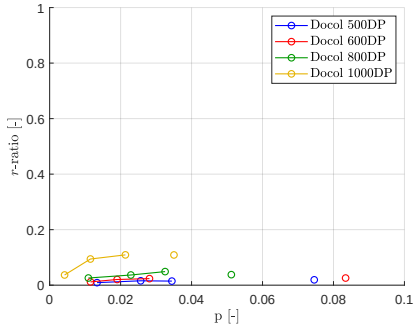

Figure A.4.46: The Bauschinger effect expressed by use of the r-ratio obtained by the RVE with spherical martensite in the centre and corners.

A.5 Homogenization

Docol 500DP

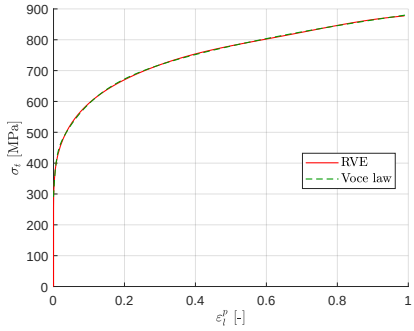

Figure A.5.47: Docol 500DP: True stress vs. plastic strain curve obtained with the calibrated Voce hardening law shown together with the RVE with cubical centre it was based upon.

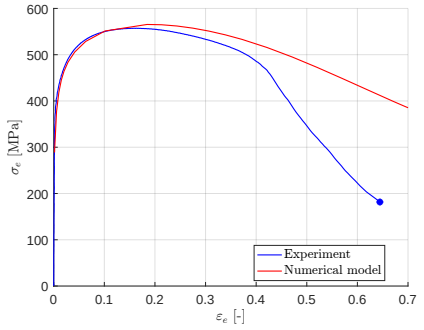

Figure A.5.48: Docol 500DP: Engineering stress-strain curve from experimental and numerical central hole test.

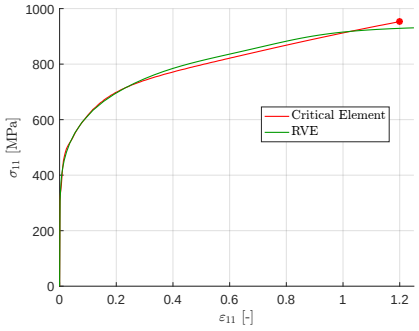

Figure A.5.49: Docol 500DP: True stress-strain from the critical element shown together with RVE exposed to the average stress triaxiality.

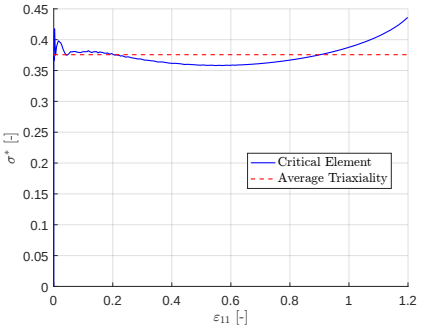

Figure A.5.50: Docol 500DP: Stress triaxiality in the critical element.

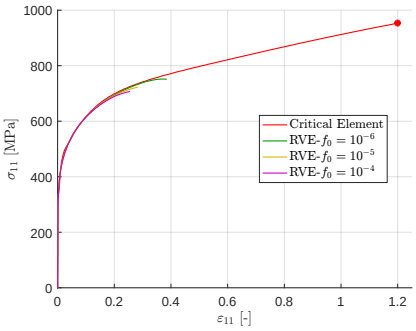

Figure A.5.51: Docol 500DP: True stress-strain from the critical element shown together with the RVE where the Gurson model with initial void volume fraction f_0 was included and exposed to the average stress triaxiality.

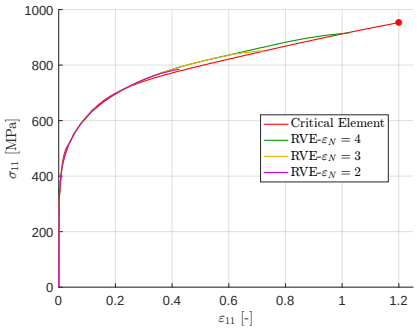

Figure A.5.52: Docol 500DP: True stress-strain from the critical element shown together with the RVE where the Gurson model with void nucleation controlled by changing ε_N was included and exposed to the average stress triaxiality. $S_N = 0.05$ and $f_N = 0.01$.

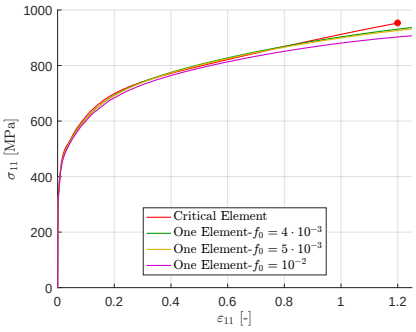

Figure A.5.53: Docol 500DP: True stress-strain from the critical element shown together with the homogeneous element where the Gurson model with initial void volume fraction f_0 was included and exposed to the average stress triaxiality.

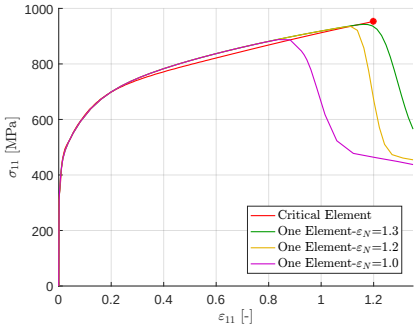

Figure A.5.54: Docol 500DP: True stress-strain from the critical element shown together with the homogeneous element where the Gurson model with void nucleation was included and exposed to the average stress triaxiality. $S_N = 0.05$ and $f_N = 0.3$.

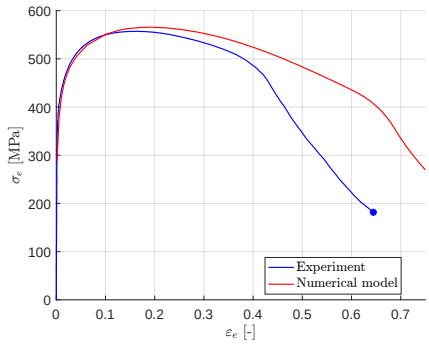

Figure A.5.55: Docol 500DP: The final simulation of central hole simulation. Engineering stress-strain. $\varepsilon_N = 1.3$, $S_N = 0.05$ and $f_N = 0.3$.

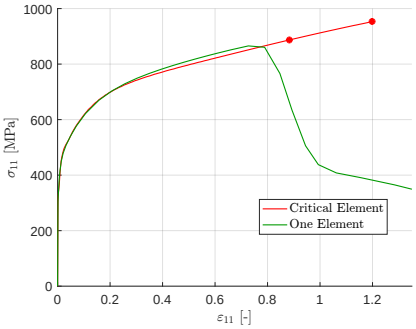

Figure A.5.56: Docol 500DP: True stress-strain from the critical element and the homogeneous element where the Gurson model with void nucleation was included and calibrated for damage initiation. $\varepsilon_N = 0.9$, $S_N = 0.05$ and $f_N = 0.3$.

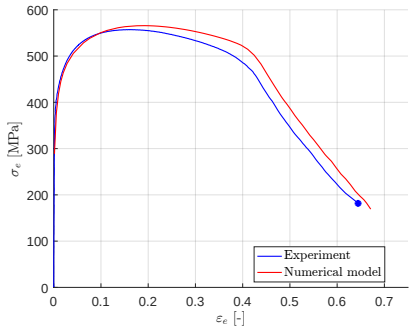

Figure A.5.57: Docol 500DP: Engineering stress-strain curve from the central hole simulation based on damage initiation. $\varepsilon_N = 0.9$, $S_N = 0.05$ and $f_N = 0.3$.

Docol 600DP

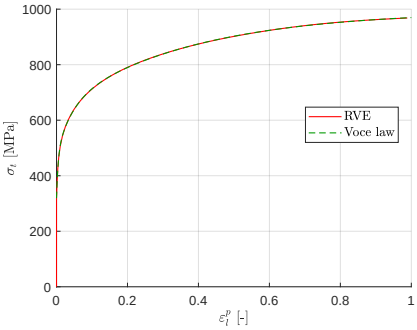

Figure A.5.58: Docol 600DP: True stress vs. plastic strain curve obtained with the calibrated Voce hardening law shown together with the RVE with cubical centre it was based upon.

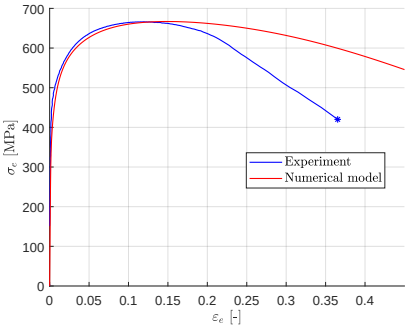

Figure A.5.59: Docol 600DP: Engineering stress-strain curve from experimentally and numerically central hole test.

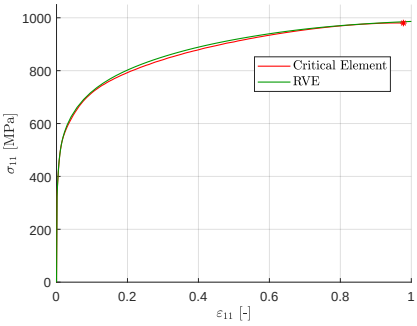

Figure A.5.60: Docol 600DP: True stress-strain from the critical element shown together with RVE exposed to the average stress triaxiality.

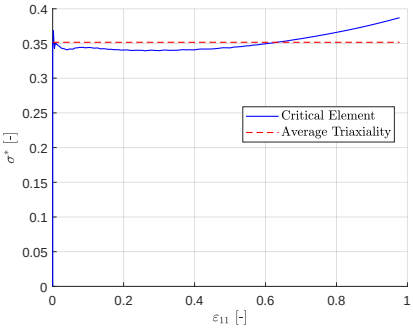

Figure A.5.61: Docol 600DP: Stress triaxiality in the critical element.

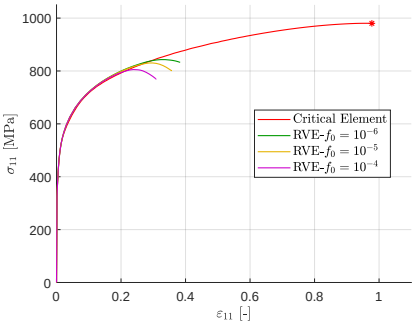

Figure A.5.62: Docol 600DP: True stress-strain from the critical element shown together with RVE where the Gurson model with initial void volume fraction f_0 was included exposed to the average stress triaxiality.

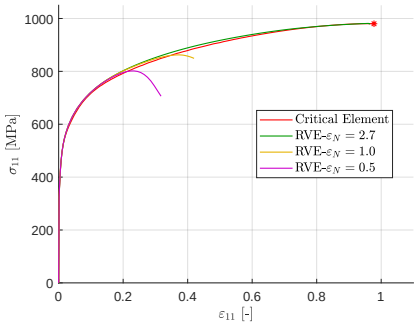

Figure A.5.63: Docol 600DP: True stress-strain from the critical element shown together with RVE where the Gurson model with void nucleation controlled by changing ε_N was included exposed to the average stress triaxiality. $S_N = 0.05$ and $f_N = 0.01$.

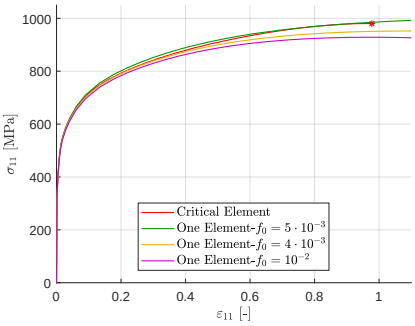

Figure A.5.64: Docol 600DP: True stress-strain from the critical element shown together with homogeneous element where the Gurson model with initial void volume fraction f_0 was included exposed to the average stress triaxiality.

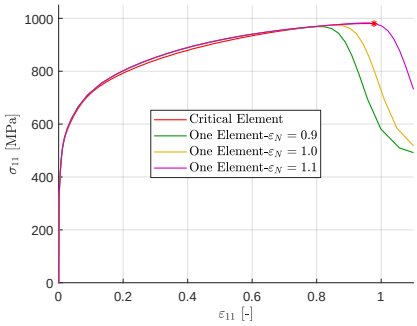

Figure A.5.65: Docol 600DP: True stress-strain from the critical element shown together with homogeneous element where the Gurson model with void nucleation was included exposed to the average stress triaxiality. $S_N = 0.05$ and $f_N = 0.3$.

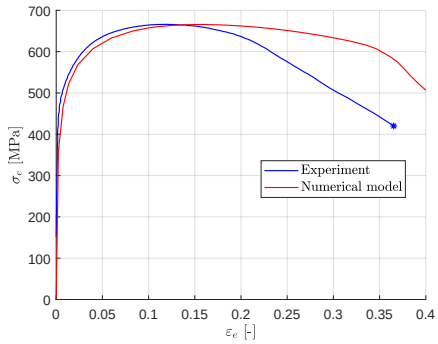

Figure A.5.66: Docol 600DP: The final simulation of central hole simulation. Engineering stress strain obtained with $\varepsilon_N = 0.9$, $S_N = 0.05$ and $f_N = 0.3$.

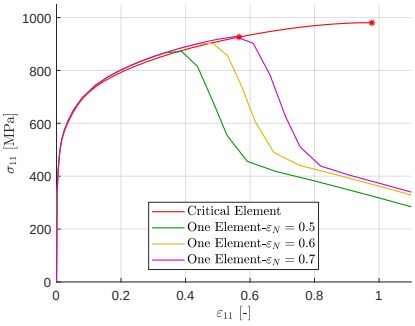

Figure A.5.67: Docol 600DP: True stress-strain from the critical element and the homogeneous element where the Gurson model with void nucleation was included and calibrated for damage evolution. $S_N = 0.05$ and $f_N = 0.3$.

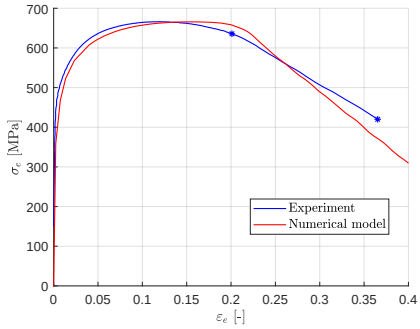

Figure A.5.68: Docol 600DP: Engineering stress-strain curve from the central hole simulation based on damage initiation. Engineering stress strain obtained with $\varepsilon_N = 0.6$, $S_N = 0.05$ and $f_N = 0.3$. Note, the slopes beyond damage initiation are not equal. Similar slopes could have been obtained by decreasing f_N. This result was assumed sufficient since the desire was to initiate fracture at damage initiation, not necessarily to obtain a perfect fit.

Docol 800DP

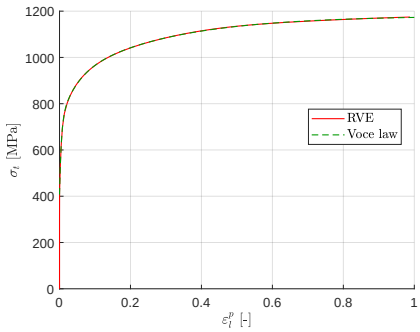

Figure A.5.69: Docol 800DP: True stress vs. plastic strain curve obtained with the calibrated Voce hardening law shown together with the RVE with cubical centre it was based upon.

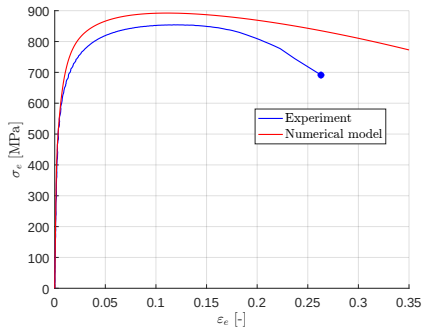

Figure A.5.70: Docol 800DP: Engineering stress-strain curve from experimental and numerical central hole test.

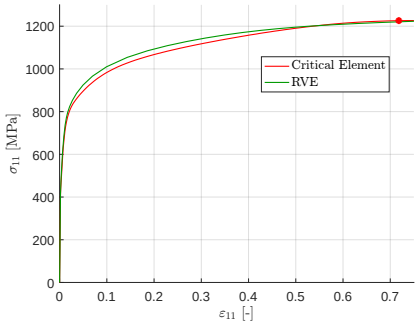

Figure A.5.71: Docol 800DP: True stress-strain from the critical element shown together with RVE exposed to the average stress triaxiality.

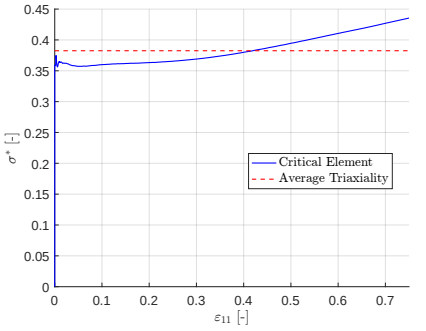

Figure A.5.72: Docol 800DP: Stress triaxiality in the critical element.

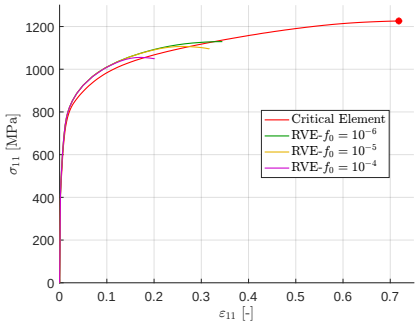

Figure A.5.73: Docol 800DP: True stress-strain from the critical element shown together with the RVE where the Gurson model with initial void volume fraction f_0 was included and exposed to the average stress triaxiality.

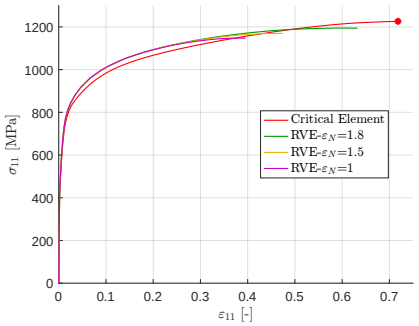

Figure A.5.74: Docol 800DP: True stress-strain from the critical element shown together with the RVE where the Gurson model with void nucleation controlled by changing ε_N was included and exposed to the average stress triaxiality. $S_N = 0.05$ and $f_N = 0.01$

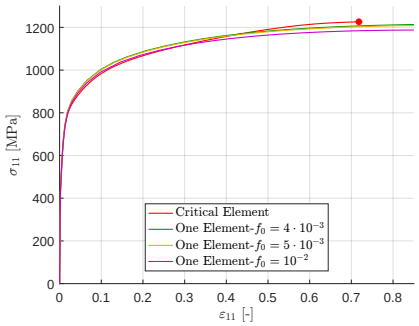

Figure A.5.75: Docol 800DP: True stress-strain from the critical element shown together with the homogeneous element where the Gurson model with initial void volume fraction f_0 was included and exposed to the average stress triaxiality.

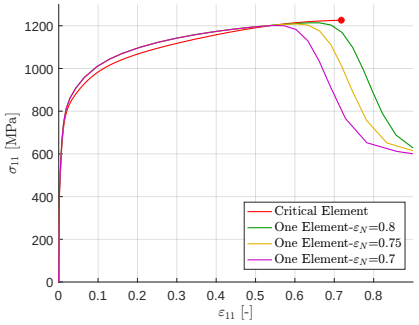

Figure A.5.76: Docol 800DP: True stress-strain from the critical element shown together with the homogeneous element where the Gurson model with void nucleation was included and exposed to the average stress triaxiality. $S_N = 0.05$ and $f_N = 0.3$.

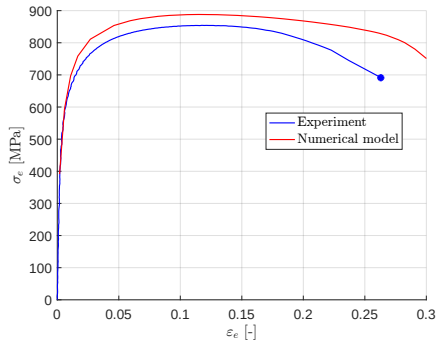

Figure A.5.77: Docol 800DP: The final simulation of central hole simulation. Engineering stress-strain obtained with $\varepsilon_N = 0.8$, $S_N = 0.05$ and $f_N = 0.3$.

Docol 1000DP

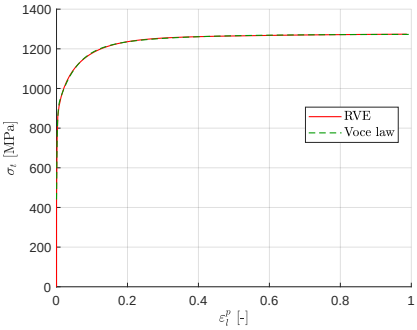

Figure A.5.78: Docol 1000DP: True stress vs. plastic strain curve obtained with the calibrated Voce hardening law shown together with the RVE with cubical centre it was based upon.

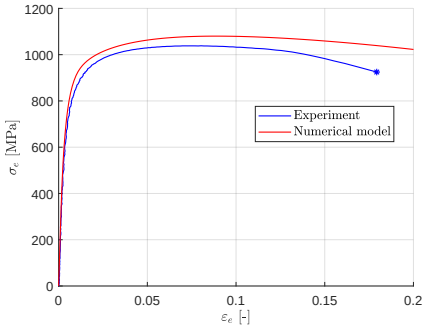

Figure A.5.79: Docol 1000DP: Engineering stress-strain curve from experimentally and numerically central hole test.

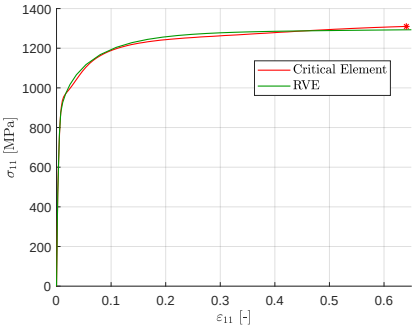

Figure A.5.80: Docol 1000DP: True stress-strain from the critical element shown together with RVE exposed to the average stress triaxiality.

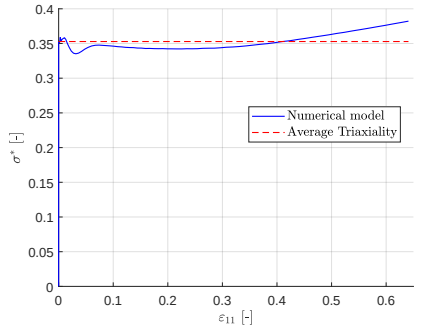

Figure A.5.81: Docol 1000DP: Stress triaxiality in the critical element.

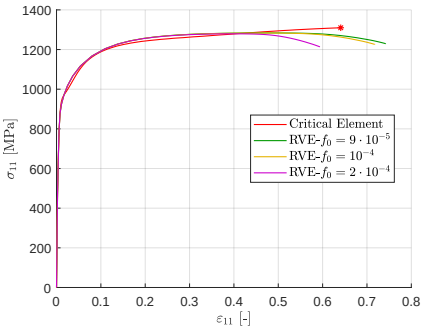

Figure A.5.82: Docol 1000DP: True stress-strain from the critical element shown together with RVE where the Gurson model with initial void volume fraction f_0 was included exposed to the average stress triaxiality.

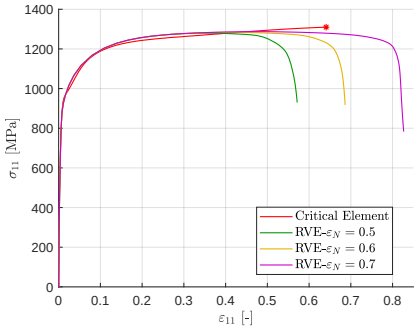

Figure A.5.83: Docol 1000DP: True stress-strain from the critical element shown together with RVE where the Gurson model with void nucleation controlled by changing ε_N was included exposed to the average stress triaxiality. $S_N = 0.05$ and $f_N = 0.01$.

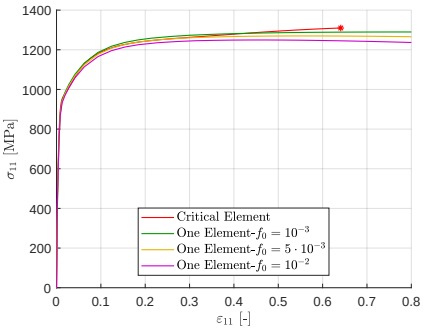

Figure A.5.84: Docol 1000DP: True stress-strain from the critical element shown together with homogeneous element where the Gurson model with initial void volume fraction f_0 was included exposed to the average stress triaxiality.

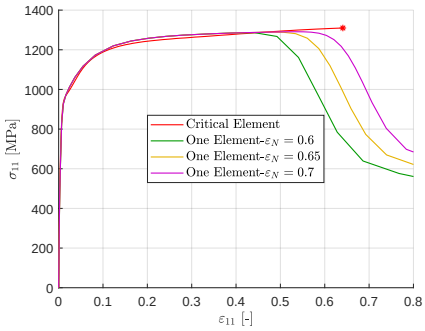

Figure A.5.85: Docol 1000DP: True stress-strain from the critical element shown together with homogeneous element where the Gurson model with void nucleation was included exposed to the average stress triaxiality. $S_N = 0.05$ and $f_N = 0.3$

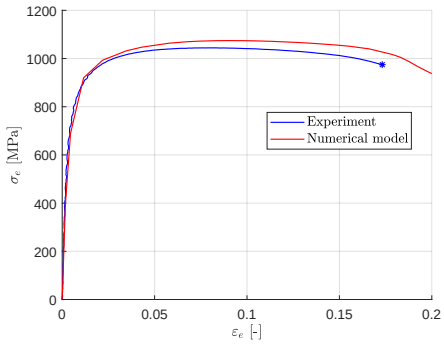

Figure A.5.86: Docol 1000DP: The final simulation of central hole simulation. Engineering stress strain obtained with $\varepsilon_N = 0.6$, $S_N = 0.05$ and $f_N = 0.3$.

B External Data

B.1 Experimental Yield Loci

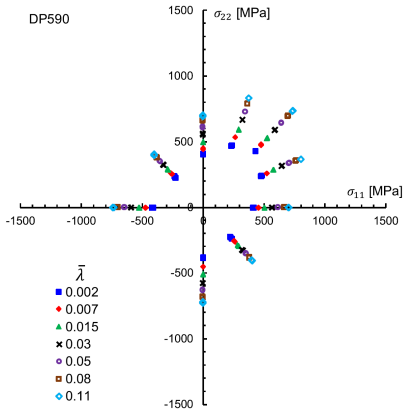

Figure B.1.1: Experimental yield loci for DP590 from Hou et al. (2019).

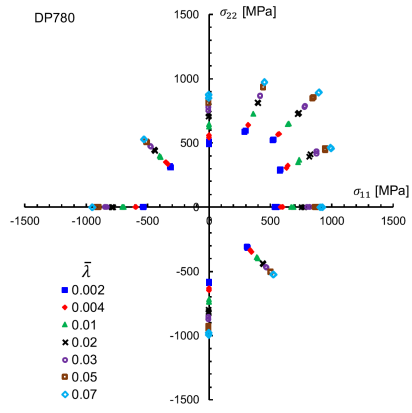

Figure B.1.2: Experimental yield loci for DP780 from Hou et al. (2019).

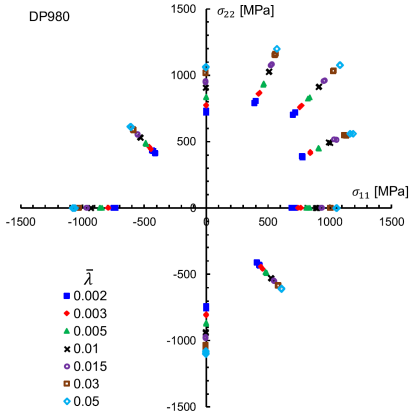

Figure B.1.3: Experimental yield loci for DP980 from Hou et al. (2019).

Sigurd Aune & Jostein Lima

Modelling and Simulation of Yielding, Work-Hardening and Fracture of Advanced High-Strength Steels

NTNU
Norwegian University of
Science and Technology